Generalizations for Insolation and Albedo to Adapt an Energy Balance Model to Other Planets

A THESIS
SUBMITTED TO THE FACULTY OF THE GRADUATE SCHOOL
OF THE UNIVERSITY OF MINNESOTA
BY

Alice Nadeau

IN PARTIAL FULFILLMENT OF THE REQUIREMENTS
FOR THE DEGREE OF
Doctor of Philosophy

Richard McGehee

May 2019

Acknowledgements

I would like express my gratitude to the following people for the roles they played in helping me get where I am today:

Dick McGehee, who has been the best advisor, in every respect, anyone could hope for. My academic twin, Kate Meyer, for always motivating me. Thanks for providing me my fallback question of "What would Kate do in this situation?" whenever I get stuck on something. Clarence Lehman, who inspires me to tackle grand challenges. Arnd Scheel and Yoichiro Mori for serving on my committee and the informal mentoring you've given me during my time at UMN. Kim Logan, for everything. Couldn't have done it without you bud. The extended McGehee academic family (especially those listed above and Harini, Somyi, Esther, and Jim), for being a sounding board and for the future collaborations I hope we have. Mark Schneider, Joyce Stern, and the Grinnell Science Project, for giving me a scientific community when I really needed one. Mark Schneider, again, for encouraging me to do research and serving as my first research advisor. This isn't a physics thesis but it's pretty close. The Grinnell College Mathematics and Physics Faculty, especially Jen Paulhus, who provided me with an outstanding foundation on which to build my career.

Finally, I would like to acknowledge the support of the Mathematics and Climate Research Network through the NSF grants DMS-0940363 and DMS-0940366 and a UMN Interdisciplinary Doctoral Fellowship through the Institute on the Environment and the Graduate School.

Dedication

I would like to dedicate this work to my family and friends who have been with me through it all. You made it all possible. Thank you!

To my parents, Mary and Jim. Thank you for always providing me the space to challenge myself, whether it was making sure I was in the right math class when I came home crying that the material was too easy or putting up with me trying to finish one last proof during our DC road trip. I couldn't have done this without your unrelenting support and belief in my abilities.

To my husband, Derek. Thank you for always being my cheerleader, for sharing in all my weird jokes, for being the voice of reason, and for all the Take 5's you snuck into my lunches. Now on to the next great adventure!

Abstract

Interest in modeling the climates of other planets has been stimulated by observations of the Pluto-Charon system and seven Earth-sized planets orbiting the nearby star TRAPPIST-1. Furthermore, as of March 2019, over four thousand planets outside of our solar system have been discovered. Scientists are interested in what these planets might be like and if they could support life as we know it, but there is very little empirical information that they can collect in order to learn more about them. For this reason, scientists must rely on models to study climate on these planets. Because so little is known about our planetary neighbors compared to Earth, and even less is known about planets outside of our solar system, it is hard to faithfully model their climates using complex models such as such as the class of models referred to as General Circulation Models (GCMs). Instead, conceptual climate models may be preferred because the small number of state variables and parameters (relative to GCMs) make it easier to quantify possible behaviors of the system. Adapting well known conceptual models for Earth to extraterrestrial and extrasolar planets raises issues whose solutions draw from the fields of celestial mechanics, harmonic analysis and nonsmooth systems. This work focuses on a main component of conceptual climate models—incoming radiation absorbed by the planet—and the mathematical considerations for and implications of adapting this component to planets other than Earth. We generalize both the distribution of insolation and location of different albedos on the planet's surface. We find that the insolation distribution for slowly rotating planets approaches a rapid rotation distribution like the reciprocal of the rotation rate. Additionally, we show that it is possible to have stable, asymmetric configurations of ice in an energy balance model of Pluto.

Contents

List of Tables

List of Figures

Chapter 1

Introduction

Energy balance climate models (sometimes energy balance models or EBMs) made their way to prominence in the geoscience fields in the late 1960's to mid 1970's. These models attempted to describe Earth's surface temperature distribution as a result of changing a handful of parameters such as planetary albedo, solar constant, or atmospheric turbidity [6, 38]. However, with the rise of faster, more efficient, and easier to access computers, large-scale Earth Systems Models (ESMs) and General Circulation Models (GCMs) soon became the norm for studying Earth's climate. Most geoscientists abandoned low dimensional dynamical systems models in favor of the developing ESMs with hundreds of parameters and state variables. Although ESMs are a useful tool in determining Earth's past and future climate, it is not always clear how results are related to different choices of parameter values or which parameters or variables have the strongest impact on the modeled climate.

Low dimensional climate models are still important tools for understanding Earth's climate and the study of such models is still vital. These models can tell us about global behaviors of the climate system as opposed to the local results that are given in ESMs. For example, low dimensional energy balance models can help us learn about the phenomenon of ice-albedo feedback (e.g. in [47], among others) but cannot tell us what

areas of the arctic will continue to have sea ice in the future. Energy balance models have contributed to scientists' understanding of a wide range of climate phenomena, including the possibility of a completely glaciated Earth and escape from it ([1] among others).

Furthermore, low dimensional mathematical models of extraterrestrial and extra-solar planetary climate can be a beneficial tool for scientists trying to understand the universe around us. Interest in modeling the climates of other planets has been ignited due to the fly-by of the Pluto-Charon system by the NASA probe New Horizons and the discovery of seven Earth-sized planets orbiting the nearby star TRAPPIST-1. Surprised by the complexity of Pluto and Charon and inspired by the prospect of liquid water and life in the TRAPPIST-1 system, scientists are now trying to understand these observations through the use of mathematical models. They employ energy balance models to study phenomena such as the stability of Pluto's nitrogen glaciers [15, 16] and the possibility of liquid water on TRAPPIST-1 planets [8]. Even though NASA has several missions designed to provide scientists with empirical information about the planets and moons close to us, relatively little is known about our planetary neighbors compared to Earth, and even less is known about planets outside of our solar system. For this reason, it is difficult to adapt the large ESMs to study our planetary neighbors. The parameter spaces of low dimensional climate models are usually easier to deal with, giving these models an edge over their more complex counterparts.

Broadly, the point of this work is to lay some of the foundation for adapting low dimensional energy balance models of Earth to other planets. We will focus on how incoming radiation is modeled and generalize some of the components of the incoming radiation term for ease of application to other planets.

The first part of this work concerns a major component of energy balance models, the incoming solar radiation, or *insolation*. In particular, we focus on how a planet's rotation rate (denoted as ω, the ratio of the number of rotations per revolution) and obliquity (tilt of the axis of rotation relative to the orbital plane) affect the distribution

of the solar energy across the planet's surface. In Chapter 2 we derive the Legendre series expansion for insolation on rapidly rotating planets and compare different truncations of this series with approximations that exist in the literature. In Chapter 3, we provide bounds for how quickly a planet's insolation distribution approaches a rapidly rotating insolation distribution as the rotation rate ω increases.

In the second part of this work, we will focus on the reflection of this energy from the planet's surface. We will remove a long-standing symmetry constraint in a particular energy balance model for the distribution of highly reflective regions on the Earth's surface. The removal of this constraint allows us to investigate symmetric and asymmetric configurations of ice on both Earth and Pluto. In fact, we could study any rapidly rotating planet with the framework laid out here, but we restrict ourselves to these two cases and leave a more general exploration to future work. We find that symmetric solutions on Earth are globally attracting and that it is possible to find asymmetric ice line configurations on Pluto that are stable. The study of Earth is presented in Chapter 4 and the study of Pluto is presented in Chapter 5.

Chapter 2

Approximating Insolation on Rapidly Rotating Planets

The insolation at any point on a planet is a function of the latitude and longitude of the point, the planet's orbital parameters (semi-major axis, obliquity, and precession angle), the position of the planet along its orbit, and the solar energy output. Using Kepler's laws and integrating over an entire year, one can show that the global annual average power flux (Watts per square meter) is given by

$$Q(a, e) = \frac{K\sqrt{a}}{\sqrt{1 - e^2}},$$

where K is proportional to the solar output, a is the semi-major axis of the planet's orbit, and e is the eccentricity [29]. This energy is then distributed across the planet's surface and is dependent on the planet's rotation rate relative to its orbital rate, obliquity angle, and precession angle. The following two chapters describe the relationship between these parameters and the distribution of energy across a planet's surface and how to best approximate the distribution for use in Budyko-Sellers type energy balance models.

This chapter concerns insolation on planets that are rapidly rotating. While it should be noted that there is no definition of "rapid rotation" in the literature, it is

generally agreed that Earth is a rapidly rotating planet. With about 366 rotations per revolution, the only planets in our solar system with slower rotation rates are Mercury (with 3 rotations every 2 revolutions) and Venus (with -0.92 rotations every revolution). Mercury and Venus are both slowly rotating by the colloquial definition used in the literature [12, 13, 14]. In Chapter 3, we will discuss what it means to be slowly rotating and provide some metrics so that the line between rapid and slow rotation can be determined. For now, we will define rapid rotation to be any rotation rate which causes the annual average insolation distribution to be rotationally symmetric about the planet's axis of rotation.

For a rapidly rotating planet, the orbital parameters and the position of the planet do not change substantially during a day, leading to a simplification of distribution by latitude of the annual average insolation. In this case, annual average insolation distribution reduces to a function only of the obliquity (β) and latitude (α) [45, 29, 13] and is given by

$$s(\alpha,\beta) = \frac{2}{\pi^2}\int_0^{2\pi} \sqrt{1-(\cos\alpha\sin\beta\sin\gamma - \sin\alpha\cos\beta)^2}\,d\gamma, \tag{2.1}$$

where γ is the longitude. Since the latitude is measured up and down from the equator, we have $-\pi/2 \leq \alpha \leq \pi/2$, while, since obliquity is the angle between the angular momentum vector of the planetary orbit and the angular momentum vector of the planetary spin, we have $0 \leq \beta \leq \pi$.

For each fixed obliquity β, $s(\alpha,\beta)$ is the distribution of insolation across the surface of the planet, so the annual average insolation at latitude α is given by

$$Q(a,e)s(\alpha,\beta).$$

In this chapter, an infinite series representation of the function $s(\alpha,\beta)$ is derived in

terms of Legendre polynomials (Theorem 2.0.1). Truncating this series gives a polynomial approximation for the insolation function, allowing for faster computation of the insolation while also avoiding the numerical approximation of the integral. A quadratic approximation of s for the Earth's obliquity has been used extensively [1, 2, 29, 30, 43, 47]. However, for other planets, a quadratic approximation fails to capture the qualitative behavior of the insolation as a function of latitude. In a previous paper [31], Nadeau and McGehee introduced a sixth order polynomial approximation and showed that it captures the characteristics of Pluto's insolation. Here that result is generalized and placed on a firm mathematical foundation using classical results about spherical harmonics.

In modeling studies, it is usually most appropriate to take sine of the latitude instead of latitude so that the infinitesimal $dy = \cos\theta d\theta$ is proportional to the area of the latitudinal strip parallel to y. Taking cosine of obliquity makes s symmetric in sine of the latitude (η) and cosine of obliquity (ζ):

$$s(\eta,\zeta) = \frac{2}{\pi^2}\int_0^{2\pi} \sqrt{1-\left(\sqrt{1-\eta^2}\sqrt{1-\zeta^2}\sin\gamma - \eta\zeta\right)^2}\, d\gamma. \tag{2.2}$$

The Legendre polynomials $P_i(x), i = 0, 1, 2, \ldots,$ form a complete orthogonal set in the space $L^2([-1,1])$ with the properties P_i has degree i and $P_i(1) = 1$ [3]. Therefore, the products $P_{i,j}(x,y) = P_i(x)P_j(y)$ form a complete orthogonal set in the space $L^2([-1,1]\times[-1,1])$. Thus we can write

$$s(\eta,\zeta) = \sum_{i=0}^{\infty}\sum_{j=0}^{\infty} c_{ij}P_i(\zeta)P_j(\eta). \tag{2.3}$$

The series naturally converges in L^2. One can show that the convergence is also pointwise, but, since we will not use that fact here, we leave the proof to the reader. Instead, we simply interpret the equal sign in equation (2.3) as equality in L^2. Surprisingly, c_{ij} is diagonal, in particular:

Theorem 2.0.1. *The annual average insolation distribution function can be written*

$$s(\eta,\zeta)=\sum_{n=0}^{\infty}A_{2n}P_{2n}(\zeta)P_{2n}(\eta), \tag{2.4}$$

where P_{2n} is the Legendre polynomial of degree $2n$, and where

$$A_{2n}=\frac{(-1)^n(4n+1)}{2^{2n-1}}\sum_{k=0}^{n}\binom{2n}{n-k}\binom{2n+2k}{2k}\binom{1/2}{k+1}.$$

Here we are using the standard notation

$$\binom{r}{j}=\frac{r(r-1)\cdots(r-j+1)}{j!}.$$

The proof of this theorem relies on two main lemmas which are stated and proved in the following two sections. The proof of the theorem is given in Section 2.3. In Section 4 we discuss convergence properties of the approximation and in Section 5 we compare the approximation to others that appear in the literature.

2.1 Rotational symmetries of square integrable functions on S^2

The proof of Lemma 2.1.1 relies on rotational symmetries of the spherical harmonics; however some ambiguities can arise when discussing rotations. For this reason, we first lay out definitions that will be used in the proof.

In $\mathbb{R}^3$, any orientation can be achieved by composing three elemental rotations, starting from a known standard direction. Let the standard direction be (x,y,z) and

the elemental matrices be

$$R_1(\cdot) = \begin{bmatrix} \cos(\cdot) & 0 & \sin(\cdot) \\ 0 & 1 & 0 \\ -\sin(\cdot) & 0 & \cos(\cdot) \end{bmatrix} \quad \text{and} \quad R_2(\cdot) = \begin{bmatrix} \cos(\cdot) & -\sin(\cdot) & \\ \sin(\cdot) & \cos(\cdot) & 0 \\ 0 & 0 & 1 \end{bmatrix}.$$

The rotation $R_1(\cdot)$ rotates the (y, z)-plane around the x-axis using the right hand rule while $R_2(\cdot)$ rotates the (x, y)-plane around the z-axis using the right hand rule. The rotation matrix $R(\rho, \beta, \alpha)$ defined by

$$R(\rho, \beta, \alpha) = R_2(\rho)R_1(\beta)R_2(\alpha)$$

is intended to operate by pre-multiplying the column vector (x, y, z) and represents an active rotation.[1] Each matrix is meant to represent the composition of intrinsic rotations.[2] In terms of orbital parameters, if $\alpha = 0$, then β is te obliquity angle and ρ is the precession angle.

Any point $(\hat{x}, \hat{y}, \hat{z})$ can be decomposed in the elemental rotations relative to the standard direction as

$$\begin{bmatrix} \hat{x} \\ \hat{y} \\ \hat{z} \end{bmatrix} = R(\rho, \beta, \alpha) \begin{bmatrix} x \\ y \\ z \end{bmatrix}.$$

Furthermore, write each set of coordinates in spherical coordinates as

$$\begin{aligned} x &= \cos\theta \sin\phi & & \hat{x} = \cos\hat{\theta} \sin\hat{\phi} \\ y &= \sin\theta \sin\phi & \text{and} \quad & \hat{y} = \sin\hat{\theta} \sin\hat{\phi} \\ z &= \cos\phi & & \hat{z} = \cos\hat{\phi} \end{aligned}$$

where θ and $\hat{\theta}$ are the azimuth angles as measured counterclockwise from the x- and

[1] The matrices act on the coordinates of vectors defined in the initial fixed reference frame and give, as a result, the coordinates of a rotated vector defined in the same reference frame.

[2] Rotations around the axes of the rotated reference frame.

$\hat{x}$-axes, respectively and ϕ and $\hat{\phi}$ are the usual polar angles. Let $R_{\rho,\beta,\alpha}$ denote the same rotation described by $R(\rho,\beta,\alpha)$ but which relates $(\hat{\theta},\hat{\phi})$ to (θ,ϕ) so that

$$(\hat{\theta},\hat{\phi}) = R_{\rho,\beta,\alpha}(\theta,\phi), \quad \text{and} \quad (\theta,\phi) = R^{-1}_{\rho,\beta,\alpha}(\hat{\theta},\hat{\phi}).$$

Note that

$$\cos\hat{\phi} = \hat{z} = \hat{z}(\alpha,\beta,\theta,\phi) = \cos\beta\cos\phi - \sin\beta\sin\phi\cos(\alpha+\theta). \tag{2.5}$$

Lemma 2.1.1. *Suppose $f(\theta,\phi)$ is a square integrable function on $S^2 \subset \mathbb{R}^3$ with bounded variation where θ is the azimuthal angle and ϕ is the polar angle. Suppose also that $R_{\rho,\beta,\alpha}$ is a proper Euler rotation as described above so that*

$$(\hat{\theta},\hat{\phi}) = R_{\rho,\beta,\alpha}(\theta,\phi)$$

and there exists a coordinate system where f depends only on the cosine of the polar angle (i.e. $f(R^{-1}_{\rho,\beta,\alpha}(\hat{\theta},\hat{\phi})) = \tilde{f}(\cos\hat{\phi})$). Then we have

$$\tilde{f}(\cos\hat{\phi}) = \tilde{f}(\alpha,\beta,\theta,\phi) = \sum_{n=0}^{\infty} \tilde{c}_n \left(\sum_{k=-n}^{n} Y_n^k(\alpha,\beta) Y_n^k(\theta,\phi) \right)$$

where $Y_n^k(\theta,\phi) = N_{n,k} e^{ik\theta} P_n^k(\cos\phi)$ is the $n-k$ spherical harmonic with normalizing factor

$$N_{n,k} = (-1)^k \sqrt{\frac{2n+1}{4\pi}\frac{(n-k)!}{(n+k)!}},$$

associated Legendre polynomial P_n^k, and

$$\tilde{c}_n = 2\pi \int_{-1}^{1} \tilde{f}(\hat{z}) P_n(\hat{z}) d\hat{z}$$

where P_n is the n-th Legendre polynomial. Furthermore, for β and θ fixed we have

$$\int_0^{2\pi} \tilde{f}(\alpha,\beta,\theta,\phi)d\theta = \int_0^{2\pi} \tilde{f}(\alpha,\beta,\theta,\phi)d\alpha = \sum_{n=0}^{\infty} \tilde{b}_n P_n(\cos\beta)P_n(\cos\phi)$$

where

$$\tilde{b}_n = \pi(2n+1)\int_{-1}^{1} \tilde{f}(\hat{z})P_n(\hat{z})d\hat{z}.$$

Proof. Notice that $\tilde{f}(\cos\hat{\phi}) = \tilde{f}(\hat{z})$. As stated above, the Legendre polynomials $P_i(x), i = 0, 1, 2, \ldots,$ form a complete orthogonal set in the space $L^2([-1,1])$ with the properties P_i has degree i and $P_i(1) = 1$ [3].

Expanding $\tilde{f}(\hat{z})$ into its Legendre series gives

$$\tilde{f}(\hat{z}) = \sum_{n=0}^{\infty} c_n P_n(\hat{z}), \tag{2.6}$$

where

$$c_n = \frac{\int_{-1}^{1} \tilde{f}(\hat{z})P_n(\hat{z})d\hat{z}}{\int_{-1}^{1} P_n(\hat{z})^2 d\hat{z}} = \frac{2n+1}{2}\int_{-1}^{1} \tilde{f}(\hat{z})P_n(\hat{z})d\hat{z}$$

and P_n is the n-th Legendre polynomial. The series naturally converges in L^2. One can show that the convergence is also pointwise, but, since we will not use that fact here, we leave the proof to the reader.

Instead, we simply interpret the equal sign in Equation (2.6) as equality in L^2. Changing back to spherical coordinates yields

$$\tilde{f}(\cos\hat{\phi}) = \sum_{n=0}^{\infty} c_n P_n(\cos\hat{\phi}). \tag{2.7}$$

The addition formula for spherical harmonics [17, 46] says that

$$P_n(\cos\omega) = \frac{4\pi}{2n+1}\sum_{k=-n}^{n} Y_n^k(\theta,\phi)Y_n^k(\theta',\phi')^*$$

where

$$\cos\omega = \cos\phi\cos\phi' + \sin\phi\sin\phi'\cos(\theta - \theta') \tag{2.8}$$

and $Y_n^k(\theta,\phi) = N_{n,k}e^{ik\theta}P_n^k(\cos\phi)$ is the $n-k$ spherical harmonic. Recall that

$$\cos\hat{\phi} = \cos\beta\cos\phi - \sin\beta\sin\phi\cos(\alpha+\theta)$$

which can be written in the form of Equation (2.8) by letting $\beta = -\tilde{\beta}$ and $\alpha = -\tilde{\alpha}$. Then for any n

$$\begin{aligned} P_n(\cos\hat{\phi}) &= \frac{4\pi}{2n+1}\sum_{k=-n}^{n} Y_n^k(\theta,\phi)Y_n^k(\tilde{\alpha},\tilde{\beta})^* \\ &= \frac{4\pi}{2n+1}\sum_{k=-n}^{n} Y_n^k(\theta,\phi)Y_n^k(\alpha,\beta) \end{aligned}$$

because $Y_n^k(\alpha,\cdot) = Y_n^k(-\alpha,\cdot)^*$ and Y_n^k is even in the second argument. Substituting the above into Equation (2.7) yields

$$\tilde{f}(\cos\hat{\phi}) = \sum_{n=0}^{\infty}\frac{4\pi c_n}{2n+1}\left(\sum_{k=-n}^{n} Y_n^k(\alpha,\beta)Y_n^k(\theta,\phi)\right).$$

Writing $\tilde{f}(\cos\hat{\phi}) = \tilde{f}(\cos\beta\cos\phi - \sin\beta\sin\phi\cos(\alpha+\theta)) = \tilde{f}(\alpha,\beta,\theta,\phi)$ gives the formula from the statement of the theorem.

To prove that

$$\int_0^{2\pi}\tilde{f}(\alpha,\beta,\theta,\phi)d\theta = \int_0^{2\pi}\tilde{f}(\alpha,\beta,\theta,\phi)d\alpha = 2\pi\sum_{n=0}^{\infty}P_n(\cos\beta)P_n(\cos\phi)$$

notice that

$$\int_0^{2\pi} \sum_{n=0}^{\infty} \tilde{c}_n \sum_{k=-n}^{n} Y_n^k(\theta,\phi) Y_n^k(\alpha,\beta) d\theta = \sum_{n=0}^{\infty} \tilde{c}_n \int_0^{2\pi} \sum_{k=-n}^{n} Y_n^k(\theta,\phi) Y_n^k(\alpha,\beta) d\theta$$

because the function is absolutely integrable over a finite interval. We see that

$$\begin{aligned}\int_0^{2\pi} \sum_{k=-n}^{n} Y_n^k(\theta,\phi) Y_n^k(\alpha,\beta) d\theta &= \sum_{k=-n}^{n} Y_n^k(\alpha,\beta) N_{n,k} P_n^k(\cos\theta) \int_0^{2\pi} e^{ik\theta} d\theta \\ &= \sum_{k=-n}^{n} Y_n^k(\alpha,\beta) N_{n,k} P_n^k(\cos\phi)(2\pi\delta_{k,0})\end{aligned}$$

where $\delta_{k,0}$ is the Kronecker Delta function indicating that the integral is zero except when $k = 0$. Then

$$\begin{aligned}\int_0^{2\pi} f(\alpha,\beta,\theta,\phi) d\theta &= 2\pi \sum_{n=0}^{\infty} \tilde{c}_n \left(N_{n,0}\right)^2 P_n(\cos\beta) P_n(\cos\phi) \\ &= \sum_{n=0}^{\infty} \left(\frac{2n+1}{2}\right) \tilde{c}_n P_n(\cos\beta) P_n(\cos\phi) \\ &= \sum_{n=0}^{\infty} \tilde{b}_n P_n(\cos\beta) P_n(\cos\phi)\end{aligned}$$

Integrating in α yields the same result. □

2.2 Integral of $x^{2k}\sqrt{(1-x^2)}$

The second lemma is instrumental for computing the coefficients of the Legendre series for the insolation distribution function.

Lemma 2.2.1. *For any non-negative integer k,*

$$\int_{-1}^{1} \sqrt{1-x^2}\, x^{2k}\, dx = (-1)^k \pi \binom{1/2}{k+1}.$$

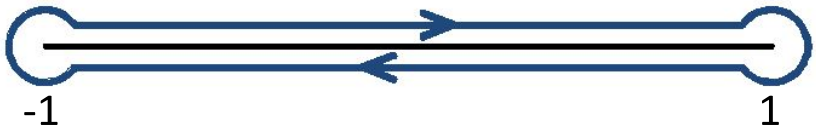

Figure 2.1: The contour, C, used in the calculation of the integral in Lemma 2.2.1.

Proof. Let

$$a_{2k} = \int_{-1}^{1} \sqrt{1-x^2}x^{2k}dx.$$

We compute a_{2k} via the integral around the contour C shown in Figure 2.1. The integral around C is given by the residue at infinity of the integrand. Namely

$$\begin{aligned} 2a_{2k} &= 2\int_{-1}^{1} \sqrt{1-x^2}x^{2k}dx \\ &= \int_{C} \sqrt{1-z^2}z^{2k}dz \\ &= -2\pi i \text{Res}(\sqrt{1-z^2}z^{2k}, \infty) \\ &= 2\pi i \text{Res}\left(\sqrt{1-\frac{1}{z^2}}\frac{1}{z^{2k}}\frac{1}{z^2}, 0\right) \\ &= -2\pi \text{Res}\left(\frac{\sqrt{1-z^2}}{z^{2k+3}}, 0\right) \end{aligned}$$

The series expansion of $\sqrt{1-z^2}$ is given by

$$\sqrt{1-z^2} = \sum_{n=0}^{\infty} \binom{1/2}{n} (-z^2)^n = \sum_{n=0}^{\infty} (-1)^n \binom{1/2}{n} z^{2n}.$$

were $\binom{1/2}{n}$ is a standard generalized binomial coefficient. Multiplying through by

$1/(z^{2k+3})$ yields

$$\frac{\sqrt{1-z^2}}{z^{2k+3}} = \sum_{n=0}^{\infty}(-1)^n \binom{1/2}{n} z^{2n-2k-3}.$$

Then we calculate the residue as

$$\operatorname{Res}\left(\frac{\sqrt{1-z^2}}{z^{2k+3}}, 0\right) = (-1)^{k+1}\binom{1/2}{k+1}$$

which establishes the formula given in the lemma. □

2.3 Proof of Theorem 2.0.1

Proof. (Theorem 2.0.1)

McGehee and Lehman [29] showed that the annual average insolation at a point on the surface of a non-rotating planet is proportional to the sine of the co-latitude in the ecliptic coordinates. Normalizing so that the total insolation is 2 gives us the insolation distribution

$$I(\hat{\phi}) = \frac{2}{\pi^2}\sin\hat{\phi} = \frac{2}{\pi^2}\sqrt{1-\hat{z}^2}$$

where $\hat{\phi}$ is the polar angle in the ecliptic coordinates. The factor of two maintains compatibility with the usual normalization of over one hemisphere.

This function is square integrable and of bounded variation, so Lemma 2.1.1 tells us that

$$I(\hat{\phi}) = I(0,\beta,\theta,\phi) = \sum_{n=0}^{\infty}\tilde{c}_n\left(\sum_{k=-n}^{n} Y_n^k(0,\beta)Y_n^k(\theta,\phi)\right).$$

Since we want the annual average insolation, we integrate over θ (a day) as was done in McGehee and Lehman (2012) [29]. Lemma 2.1.1 then tells us

$$s(\beta,\phi) = \sum_{n=0}^{\infty} A_n P_n(\cos\beta)P_n(\cos\phi)$$

where

$$\begin{aligned} A_n &= \pi(2n+1)\int_{-1}^{1}\frac{2}{\pi^2}\sqrt{1-z^2}P_n(z)dz \\ &= \frac{2(2n+1)}{\pi}\int_{-1}^{1}\sqrt{1-z^2}P_n(z)dz \end{aligned}$$

If n is odd, the integral is zero. Furthermore, the coefficients of the Legendre polynomials are well-known [3]. In particular,

$$P_{2n}(x) = \sum_{k=0}^{n} p_{2n,2k}x^{2k},$$

where

$$p_{2n,2k} = \frac{(-1)^{n-k}}{4^n}\binom{2n}{n-k}\binom{2n+2k}{2n}.$$

Therefore, we can write

$$\begin{aligned} A_{2n} &= \frac{2(4n+1)}{\pi}\int_{-1}^{1}\sqrt{1-z^2}P_{2n}(z)dz \\ &= \frac{2(4n+1)}{\pi}\int_{-1}^{1}\sqrt{1-z^2}\left(\sum_{k=0}^{n}p_{2n,2k}z^{2k}\right)dz \\ &= \frac{2(4n+1)}{\pi}\sum_{k=0}^{n}p_{2n,2k}\int_{-1}^{1}\sqrt{1-z^2}z^{2k}dz \\ &= \frac{2(4n+1)}{\pi}\sum_{k=0}^{n}\frac{(-1)^{n-k}}{4^n}\binom{2n}{n-k}\binom{2n+2k}{2n}\int_{-1}^{1}\sqrt{1-z^2}z^{2k}dz \end{aligned}$$

Applying Lemma 2.2.1 gives

$$A_{2n} = \frac{(4n+1)(-1)^n}{2^{2n-1}}\sum_{k=0}^{n}\binom{2n}{n-k}\binom{2n+2k}{2n}\binom{1/2}{k+1}$$

which proves the formula. □

2.4 Convergence of the Legendre Approximations

For a fixed obliquity, we can compute the convergence of the approximation in $L^2([-1,1])$ as well as $\mathcal{C}^0([-1,1])$. Although convergence in L^2 is the natural space to consider from an analysis perspective, convergence in $\mathcal{C}^0$ may be more appropriate from a modeling perspective. In particular, because we are concerned with the qualitative behavior of solutions in the Budyko-Widiasih model, convergence in the $\mathcal{C}^0$ norm may better capture qualitative differences between the approximations of different degrees.

Below we present mostly numerical results on the convergence rate of the Legendre approximations and leave the proofs for a future paper. We note that for approximations of degree bigger than 8, the coefficients A_{2n} of the approximation get very unwieldy. In particular, since our recommendation is to only take the approximation up to degree six for use in energy balance models, the proof of the convergence rates will be a somewhat superficial result. We present the following conjecture to motivate a future investigation into the convergence rate.

Conjecture 2.4.1. *Convergence of $\sigma_{2N}(\eta,\zeta)$ to $s(\eta,\zeta)$ in $L^2([-1,1])$ is of order N^{-2} for $\zeta \neq 1$ and order N^{-1} for $\zeta = 1$.*

2.4.1 Convergence in $L^2([-1,1])$

Provided one can show that the derivative $\partial s(\eta,\zeta)/\partial\eta$ is bounded in L^2, it is routine to show that the convergence of the Legendre series approximations is at least order $1/N^2$, i.e.

$$\|s(\cdot,\zeta) - \sigma_{2N}(\cdot,\zeta)\|^2_{L^2([-1,1])} \approx \frac{C}{(2N)^2} \tag{2.9}$$

for large N. We observe that the derivatives $\partial s(\eta,\zeta)/\partial\eta$ are bounded for $\zeta \in [0,1)$, although showing this directly is rather thorny due to the form of $s(\eta,\zeta)$.

Instead we numerically compute the convergence rate. The results are compiled in

$2N$	$\|s(\eta,\zeta_{Earth})-\sigma_{2N}(\eta,\zeta_{Earth})\|_{L^2}$	Approx. order of convergence (α)
2	$2.18972\cdot 10^{-2}$	
4	$6.46609\cdot 10^{-3}$	1.75978
8	$2.90261\cdot 10^{-3}$	1.15554
16	$5.70582\cdot 10^{-3}$	2.34685
32	$1.13598\cdot 10^{-4}$	2.32849
64	$4.91472\cdot 10^{-5}$	1.20877

Table 2.1: Approximate convergence rates (α) in the L^2 norm for the approximation to Earth's insolation. See the in text discussion for a description of α.

Table 2.1 for $\zeta = \zeta_{Earth} = \cos((23.5/180)\pi)$. The first column gives the largest degree of the polynomial used for the approximation. The second column gives the L^2 norm of the difference between the approximation and the actual insolation function $s(\eta, \zeta_{Earth})$. The third column gives an approximation to the order of convergence. This is computed by first assuming that

$$\|s(\eta,\zeta)-\sigma_{2^M}(\eta,\zeta)\|_{L^2} \approx \frac{C}{(2^M)^\alpha} \tag{2.10}$$

Then we have that

$$\frac{\|s(\eta,\zeta)-\sigma_{2^M}(\eta,\zeta)\|_{L^2}}{\|s(\eta,\zeta)-\sigma_{2^{M+1}}(\eta,\zeta)\|_{L^2}} \approx \left(\frac{2^{M+1}}{2^M}\right)^\alpha \tag{2.11}$$

so that

$$\alpha \approx \frac{1}{\log 2}\log\left(\frac{\|s(\eta,\zeta)-\sigma_{2^M}(\eta,\zeta)\|_{L^2}}{\|s(\eta,1)-\sigma_{2^{M+1}}(\eta,\zeta)\|_{L^2}}\right). \tag{2.12}$$

We report these approximate α values in the third column. The α values are only reported to $2N = 64$ because round off errors due to the coefficients in the summands of A_{2N} at $2N = 128$ and above cause our approximation for α to be rather poor.

For $\zeta = 1$ the derivative with respect to sine of the latitude is unbounded in L^2.

$2N$	$\|s(\eta,1)-\sigma_{2N}(\eta,1)\|_{L^2}$	Approx. order of convergence
2	$7.27019 \cdot 10^{-2}$	
4	$2.97384 \cdot 10^{-2}$	1.28967
8	$1.02277 \cdot 10^{-2}$	1.53984
16	$3.36645 \cdot 10^{-3}$	1.60319
32	$1.32593 \cdot 10^{-3}$	1.34423
64	$6.32304 \cdot 10^{-4}$	1.06831
128	$3.12467 \cdot 10^{-4}$	1.01691
256	$1.56444 \cdot 10^{-4}$	$9.98062 \cdot 10^{-1}$
512	$7.84126 \cdot 10^{-5}$	$9.96485 \cdot 10^{-1}$

Table 2.2: Approximate convergence rates in the L^2 norm for the approximation to the insolation on a planet with no axial tilt. See the in text discussion for a description of α.

However, because the function $s(\eta, 1)$ is still continuous at the endpoints, theory indicates that the convergence rate should be order $1/N$. Our numerical computations confirm this (see Table 2.2). We are able to compute the approximation for more values of N than in the case with $\zeta = \zeta_{Earth}$ because $\zeta = 1$ allows us to avoid some of the roundoff error due to our numerical integration step.

2.4.2 Convergence in $\mathcal{C}^0([-1,1])$

For modelers, the L^2 norm may not be the ideal measure for goodness-of-fit of the approximation. Instead, the $\mathcal{C}^0$ norm may be more appropriate. Take the norm in $\mathcal{C}^0([-1,1])$ to be

$$\|f\|_{\mathcal{C}^0([-1,1])} = \sup_{x\in[-1,1]} |f(x)|. \tag{2.13}$$

From Wang [44], if we can show that s is absolutely continuous, $\partial(s(\eta,\zeta))/\partial\eta$ is of

$2N$	$\|s(\eta,1)-\sigma_{2N}(\eta,1)\|_{\mathcal{C}^0}$	Approx. order of convergence
4	$2.34375 \cdot 10^{-1}$	
8	$1.34583 \cdot 10^{-1}$	0.80032
16	$7.28457 \cdot 10^{-2}$	0.88558
32	$3.80199 \cdot 10^{-2}$	0.93809
64	$1.94405 \cdot 10^{-2}$	0.96769
128	$9.83219 \cdot 10^{-3}$	0.98348
256	$4.94465 \cdot 10^{-3}$	0.99154
512	$2.47954 \cdot 10^{-3}$	0.99578

Table 2.3: Approximate convergence rates in the $\mathcal{C}^0$ norm for the approximation to the insolation on a planet with no axial tilt. See the in text discussion for a description of α.

bounded variation and

$$V_1 = \int_{-1}^{1} \left| \frac{\partial}{\partial \eta} s(\eta, \zeta) \right| (1-\eta^2)^{-1/4} d\eta < \infty \tag{2.14}$$

then we can conclude that for fixed ζ we have

$$\|s(\eta,\zeta) - \sigma_{2N}(\eta,\zeta)\|_{\mathcal{C}^0([-1,1])} = \frac{4V_1}{\sqrt{\pi(4N-5)}}. \tag{2.15}$$

However, we see that our numerical computations for the $\mathcal{C}^0$ error for this particular case, is much better than this general result. Even when $\zeta = 1$ we have that the convergence is roughly of order $1/N$ even though $s(\eta, 1)$ has an unbounded derivative. The approximate order of convergence for σ_{2N} in the $\mathcal{C}^0$ norm is displayed in Table 2.3.

2.5 Comparisons with Other Approximations

Finding the insolation distribution for a planet is not a new problem, and various other approximations exist. The sixth degree polynomial approximation, σ_6, gotten by

truncating Equation 2.4 at $n = 3$ is given by

$$\sigma_6(y, \beta) = 1 - s_2 p_2(\cos\beta) p_2(y) - s_4 p_4(\cos\beta) p_4(y) - s_6 p_6(\cos\beta) p_6(y) \tag{2.16}$$

where $s_2 = 5/8$, $s_4 = 9/64$, and $s_6 = 65/1024$ and the p_k's are the Legendre polynomials

$$p_2(y) = (3y^2 - 1)/2, \tag{2.17}$$

$$p_4(y) = (35y^4 - 30y^2 + 3)/8, \tag{2.18}$$

$$p_6(y) = (231y^6 - 315y^4 + 105y^2 - 5)/16. \tag{2.19}$$

The approximation σ_6 is preferable to other approximations in the literature because

1. it has explicit dependence on obliquity,
2. it is a better approximation in the L^2 norm than any other polynomial approximation of equal or lesser degree,
3. for obliquity angles between 7° and 183°, σ_6 is the best approximation in the $\mathcal{C}^0$ norm than other approximations in the literature,
4. for obliquity angles between 50° and 130°, σ_6 is a better approximation in the $\mathcal{C}^0$ norm than σ_2 and σ_4, and
5. σ_6 is the lowest degree polynomial that captures the qualitative distribution of insolation for all obliquities.

The polynomial approximation σ_6 should be used instead of the integral form of the insolation distribution function and other approximations in the literature because the approximation is more computationally efficient and sufficiently accurate to capture the qualitative characteristics of the actual distribution function for any obliquity.

2.5.1 Approximations by North [32] and Chylek and Coakley [9]

North [32] explicitly gives a second degree approximation for the insolation distribution of Earth as

$$\hat{\sigma}(\eta) = 1 - 0.482 p_2(\eta)$$

(see equation 2 in [32]). The degree two approximation gotten by truncating Equation 2.4 at $n = 1$ is

$$\sigma_2(\eta, \hat{\zeta}) = 1 + A_2 p_2(\hat{\zeta}) p_2(\eta) = 1 - 0.482 p_2(\eta) \tag{2.20}$$

where $\hat{\zeta} = \cos(23^\circ) \approx 0.920505$. We see that North's approximation $\hat{\sigma}$ is the second degree Legendre series expansion, $\hat{\sigma}(\eta) = \sigma_2(\eta, \hat{\zeta})$. In fact, the obliquity of Earth in the currrent epoch is 23.4°. Letting $\zeta_{Earth} = \cos(23.4^\circ) \approx 0.91775$, we have

$$\sigma_2(\eta, \zeta_{Earth}) = 1 + A_2 p_2(\zeta_{Earth}) p_2(\eta) = 1 - 0.477 p_2(\eta) \tag{2.21}$$

which should be used for studies of Earth's current cliamte. In the following section we use the approximation with $\hat{\zeta}$ so that we can better compare with North's approximation. In an earlier study, North notes that $\hat{\sigma}$ was first given in Chýlek and Coakely [33, 9] as a linear interpolation of the insolation distribution, although no closed-form formula is given in that paper. Since this approximation was computed only for the current obliquity of the Earth, it cannot be used to compute changes due to the Milankovitch cycles, nor can it be used for other planets.

North states that $\hat{\sigma}$ uniformly approximates the actual distribution within 2% [32]. North does not explicitly state what metric he is using, but he cannot mean the $\mathcal{C}^0$, L^∞, nor L^2 norms because

$$\|s(\eta, \hat{\zeta}) - \hat{\sigma}(\eta)\|_{\mathcal{C}^0} = \|s(\eta, \hat{\zeta}) - \hat{\sigma}(\eta)\|_{L^\infty} = \sup_{\eta \in [0,1]} |s(\eta, \hat{\zeta}) - \hat{\sigma}(\eta)| = 0.0306712, \tag{2.22}$$

and

$$\|s(\eta,\hat{\zeta}) - \hat{\sigma}(\eta)\|_{L^2} \approx 0.023263. \tag{2.23}$$

Furthermore, for the region between $\eta \approx 0.89$ and $\eta = 1$ we have that the relative errror between the two functions, i.e.

$$\frac{|\hat{\sigma}(\eta) - s(\eta,\hat{\zeta})|}{s(\eta,\hat{\zeta})}, \tag{2.24}$$

is greater than 0.02 and has a maximum of 0.0543613 around $\eta = 0.952$. In fact, the relative error is greater than 0.02 on the interval $[0.6, 0.78]$ as well. Using this measure, $\hat{\sigma}$ is within 5.5% of $s(\eta,\hat{\zeta})$ for all latitudes.

The sixth degree approximation is given by

$$\sigma_6(\eta,\hat{\zeta}) = 1 - 4.82 \cdot 10^{-1} p_2(\eta) - 4.76 \cdot 10^{-2} p_4(\eta) - 6.59 \cdot 10^{-3} p_6(\eta). \tag{2.25}$$

Unsurprisingly, it does better than North's degree two approximation in both the $\mathcal{C}^0$ norm, with

$$\|\sigma_6(\eta,\hat{\zeta}) - s(\eta,\hat{\zeta})\|_{\mathcal{C}^0} = 0.0203968, \tag{2.26}$$

and the L^2 norm, with

$$\|\sigma_6(\eta,\hat{\zeta}) - s(\eta,\hat{\zeta})\|_{L^2} \approx 5.53131 \cdot 10^{-3}. \tag{2.27}$$

In Figure 2.2 we see the plots for $|s(\eta,\hat{\zeta}) - \hat{\sigma}(\eta)|$ (solid plot) and $|s(\eta,\hat{\zeta}) - \sigma_6(\eta,\hat{\zeta})|$ (dashed plot) as functions of η. Notice that the maxima of these plots give the value for the error in the $\mathcal{C}^0$ norm. Although σ_6 is a better approximation in both the $\mathcal{C}^0$ and L^2 norms, we see that it is not uniformly better. In particular, there are latitude ranges where $\hat{\sigma}$ is closer to s than σ_6.

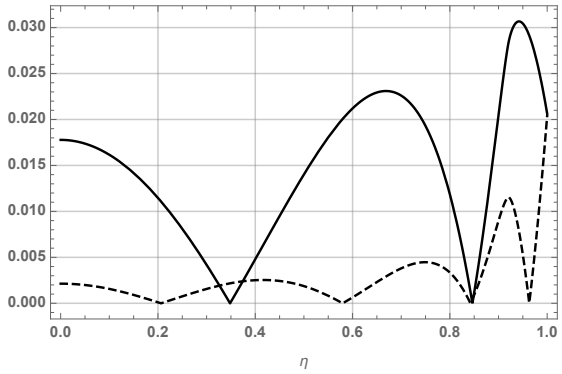

Figure 2.2: The differences in absolute value between $s(\eta, \hat{\zeta})$ and $\hat{\sigma}$ (solid plot) and $\sigma_6(\eta, \hat{\zeta})$ (dashed plot). The maxima of these plots give the error of the approximation in the $\mathcal{C}^0$ norm.

2.5.2 Approximation by Ojakangas and Stevenson [34]

The approximation given in Ojakangas and Stevenson [34] gives an explicit dependence on obliquity and is given by

$$\check{\sigma}(\eta, \zeta) = \begin{cases} \frac{4\sqrt{1-\eta^2}}{\pi} & \eta > \zeta \\ \frac{4\sqrt{\arccos^2(\zeta)+\arccos^2(\eta)}}{\sqrt{2}\pi} & \eta \leq \zeta \end{cases} \tag{2.28}$$

where η is the sine of the latitude and ζ is cosine of the obliquity (see equations A.17 and A.18 in [34]). Ojakangas and Stevenson developed this approximation to understand the insolation on Europa and note that $\check{\sigma}$ is valid only when ζ is close to 1 (i.e. an obliquity close to zero) [34]. Ojakangas and Stevenson use $\arccos \zeta = 3°$. The degree six approximation with $\check{\zeta} = \cos(3°)$ is

$$\sigma_6(\eta, \check{\zeta}) = 1 - 3.1 \cdot 10^{-1} p_2(\eta) - 5.13 \cdot 10^{-2} p_4(\eta) - 1.87 \cdot 10^{-2} p_6(\eta). \tag{2.29}$$

The functions $|s(\eta, \hat{\zeta}) - \check{\sigma}(\eta, \zeta)|$ and $|s(\eta, \hat{\zeta}) - \sigma_6(\eta, \zeta)|$ are plotted in Figure 2.3 as functions of η for two values of ζ. It should be noted that $\check{\sigma}$ is continuous only when

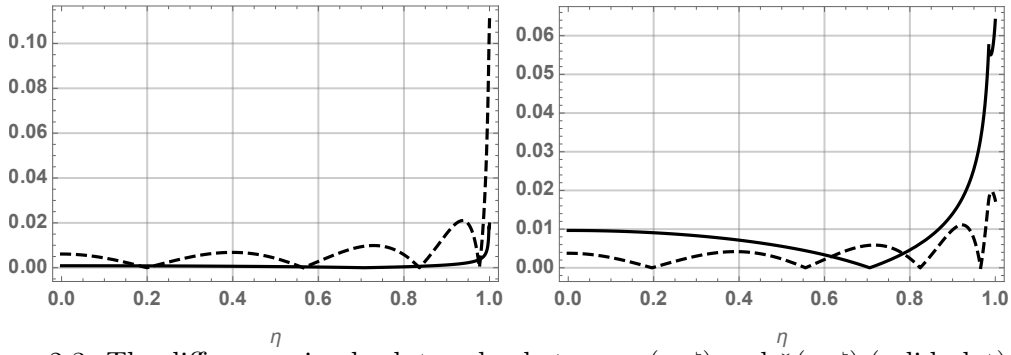

Figure 2.3: The differences in absolute value between $s(\eta, \zeta)$ and $\check{\sigma}(\eta, \zeta)$ (solid plot) and $\sigma_6(\eta, \zeta)$ (dashed plot). The maxima of these plots give the error of the approximation in the $\mathcal{C}^0$ norm. **Left:** Letting $\zeta = \check{\zeta}$ and **Right:** Letting $\zeta = \cos(10^\circ)$. Note that the vertical scales for the two plots are different.

$\zeta = 1$. For all other obliquities, $\check{\sigma}$ is discontinuous at $\eta = \pm\zeta$ and the jumpdistance increases as the obliquity increases.

At Jupiter's obliquity, we have

$$\|s(\eta, \check{\zeta}) - \check{\sigma}(\eta)\|_{L^\infty} = 0.0194958, \quad \text{and} \quad \|s(\eta, \check{\zeta}) - \hat{\sigma}(\eta)\|_{L^2} \approx 0.00235491, \tag{2.30}$$

whereas

$$\|s(\eta, \check{\zeta}) - \sigma_6(\eta, \check{\zeta})\|_{L^\infty} = 0.110566, \quad \text{and} \quad \|s(\eta, \check{\zeta}) - \hat{\sigma}(\eta)\|_{L^2} \approx 0.0147827. \tag{2.31}$$

In Figure 2.4, we see the error of the approximations to $s(\eta, \zeta)$ in the L^∞ norm as a function of the obliquity. The Ojakangas and Stevenson approximation (solid line) is better than the sixth degree Legendre approximation (dashed line) in both the $\mathcal{C}^0$ and L^2 norms for obliquities smaller than 7°. When modeling planets with low obliquity angle, the Ojakangas and Stevenson approximation may be preferable over the degree six Legendre approximation as long as the discontinuities are not an issue in the modeling framework.

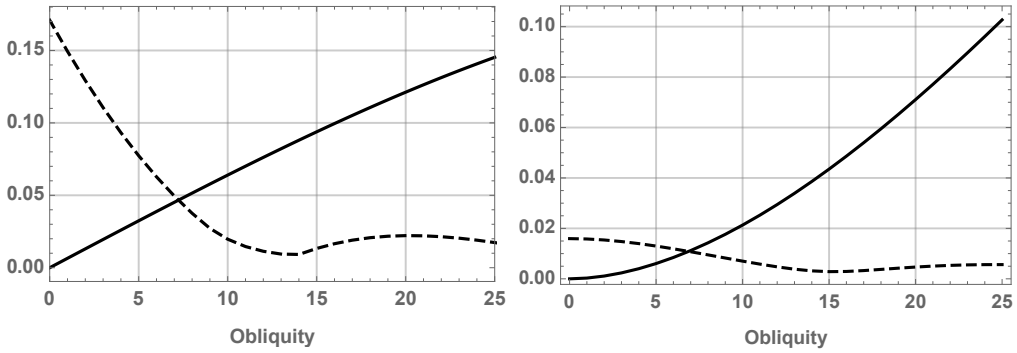

Figure 2.4: The error of the approximations in the $\mathcal{C}^0$ norm (left) and the L^2 norm (right) as a function of the obliquity. Solid curves are the Ojaknagas and Stevenson approximation, $\check{\sigma}(\eta, \zeta)$ and dashed curves are the sixth degree Legendre approximation, $\sigma_6(\eta, \zeta)$.

2.5.3 Legendre Approximations of Degree Two, Four, and Six

At the beginning of this section, we asserted that the sixth degree Legendre approximation is the preferable degree approximation to choose when modeling insolation on rapidly rotating planets. Here we compare the first three Legendre series approximations.

The biggest difference between the approximations is how well they capture the qualitative aspects of the insolation distribution. A second order approximation is sufficient for Earth's obliquity ($\beta \approx 23.4°$), however other obliquity angles produce qualitatively different insolation distributions and the second order approximation is no longer sufficient to capture an accurate insolation distribution. In particular, for obliquities between 47° and 63° (and 117° and 133°), the insolation has a characteristic 'W' shape. This 'W' shape is first captured for all obliquities by the degree six approximation, see Figure 2.5.

The L^2 error as a function of the obliquity is given in Figure 2.6. As expected, the $2N$ approximation is bounded above by the $2(N-1)$ approximation; however, it

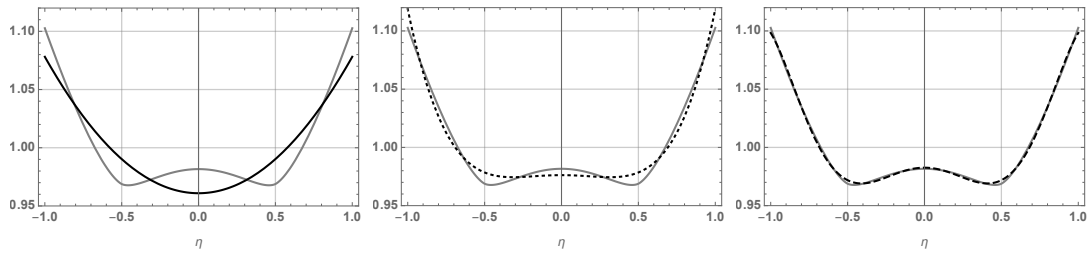

Figure 2.5: The insolation distribution $s(\eta, \zeta)$ (gray) and the degree two (solid, left), degree four (dotted, center), and degree six (dashed, right) approximations for an obliquity angle of 120° (Pluto's obliquity).

is interesting to note that at some obliquities, there is no reduction in the L^2 error between successive approximations and one must take an additional term in the Legendre approximation to ensure a decrease in the error.

The $\mathcal{C}^0$ error as a function of the obliquity is given in Figure 2.7. Here the decrease in error is not monotonic for all obliquities as we increase the degree of the approximation. For example, the degree two approximation is better than the degree four approximation for obliquity angles between 25° and 32°. As with the L^2 error, we see that one must take an additional term in the Legendre approximation to ensure a decrease in the error, although it is not clear if this is true for all N.

2.6 Discussion

In this chapter we have derived the Legendre series expansion for the insolation distribution on rapidly rotating planets as a function of sine of the latitude and the planet's obliquity. Furthermore, we give an explicit formula for the coefficients of this series as it depends on the obliquity.

Being able to compute insolation by latitude as an explicit function of obliquity is particularly important in the case of Mars due to the chaotic nature of Mars' obliquity over the course of 5 billion years. Laskar et al., [28], showed that the obliquity of

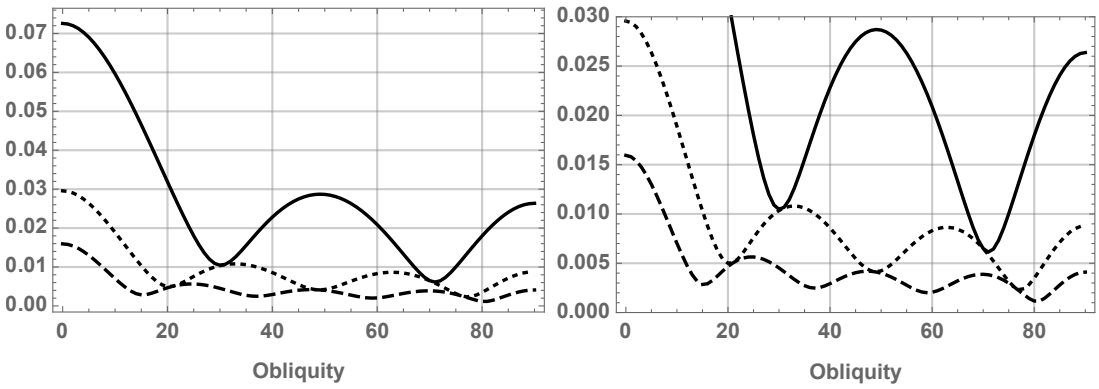

Figure 2.6: The L^2 error for the degree two (solid), degree four (dotted), and degree six (dashed) approximations as a function of obliquity. Note that these errors are symmetric about an obliquity angle of 90°. The right hand plot has a zoomed vertical scale for a clearer representation of the norms for large obliquities.

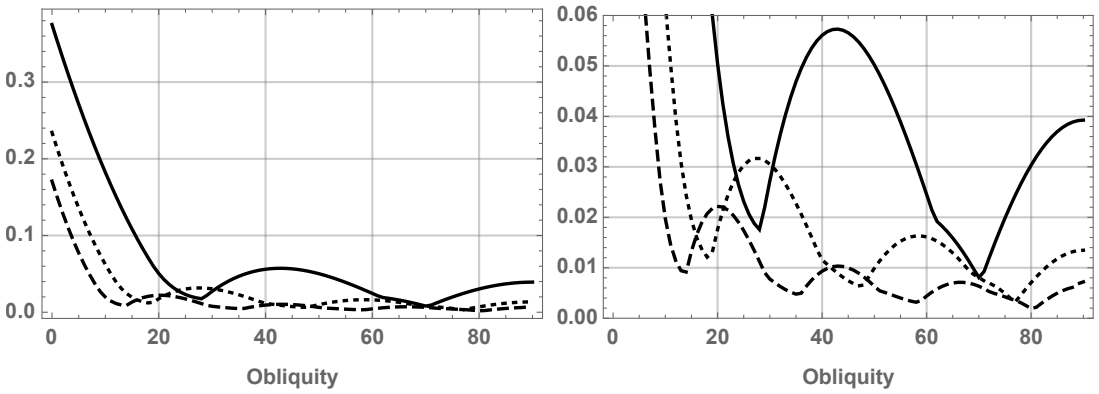

Figure 2.7: The $\mathcal{C}^0$ error for the degree two (solid), degree four (dotted), and degree six (dashed) approximations as a function of obliquity. Note that these errors are symmetric about an obliquity angle of 90°. The right hand plot has a zoomed vertical scale for a clearer representation of the norms for large obliquities.

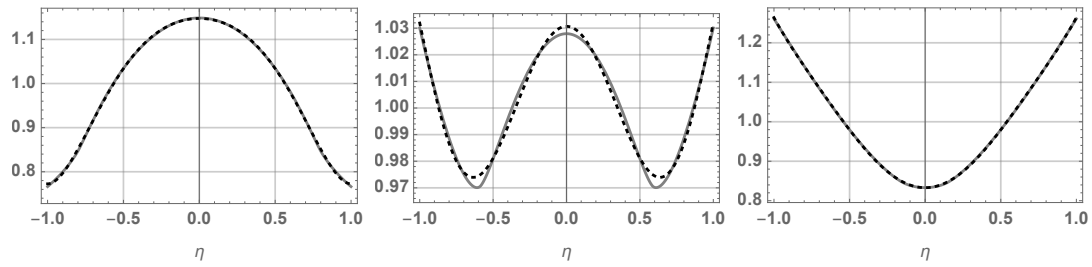

Figure 2.8: Insolation distribution for various obliquity values in Mars' orbital history. In all plots we give the actual (gray) and sixth order approximation to the insolation distribution (black dashed). Note: the vertical scales are different across plots and the actual and approximations plots are nearly identical by eye for the left and right figures. In (a) we have $\beta = 37^\circ$ which is Mars' average obliquity as given in [28], in (b) we have $\beta = 54^\circ$ which gives an example where polar and equatorial regions receive about the same yearly insolation, and in (c) we have $\beta = 82^\circ$, which is the maximal possible obliquity, [28].

Mars ranges from $\beta \approx 24^\circ$ to $\beta \approx 82^\circ$. Over this range in obliquity, the insolation distribution changes drastically, going from a downward facing parabolic shape, to a strong 'W' shape, to an upward facing parabolic shape (see Figure 2.8). In modeling the climate of Mars over time, it would necessary to have an algebraic representation of the insolation with explicit dependence on obliquity.

We also compare finite truncations of this series to two other approximations which exist in the literature. We conclude that the sixth degree approximation is the optimal approximation to use for rapidly rotating planets with obliquity greater than 7.5° because the error is smallest in both the L^2 and $\mathcal{C}^0$ norms compared to other approximations, it give explicit dependence on the obliquity, and it is the lowest degree approximation that captures the qualitative characteristics of the distribution for all obliquities.

Chapter 3

Insolation on Slowly Rotating Planets

The analysis conducted in Chapter 2 rests on an assumption that the planet is rapidly rotating; however, rapid rotation is not well-defined in the literature. In some sense, the definition is prescriptive: if equation (2.2) gives a good approximation for the insolation distribution over the course of a year, then the planet is rapidly rotating. This definition encompasses planets that rotate many times on their axis over the course of one revolution, but it also captures some less intuitive cases. For example, below we will see that planets with zero obliquity on a circular orbit with an integer number of rotations ($n > 1$) per revolution, have constant yearly average insolation on fixed latitudes. This means that equation (2.2) applies, but we wouldn't call a planet that rotates twice over the course of a year "rapidly rotating."

Conversely, it is clear that when a planet rotates only once on its axis over the course of a year that the situation is different. For example, the moon is tidally locked to the Earth, meaning that it rotates once on its axis during one orbit around the Earth. If we consider this tidally locked scenario in terms of a sun and planet with zero obliquity on a circular orbit, we see that one side of the planet would be in perpetual day and the

other would be in perpetual night, resulting in a highly varied distribution of sunlight by longitude. Since the analysis done in Chapter 2 does not depend on longitude, we see that this would give us a very bad approximation.

In several works ([11, 12, 13]), Dobrovolskis has investigated how a planet's eccentricity and obliquity affect its insolation if it has a small integer orbital resonance between its rotation rate and its orbital rate. He considers the whole and half integer cases of rotation to orbit resonance between 1:1 and 4:1. Dobrovolskis numerically computes a planet's insolation as a function of latitude and longitude by first computing the sub-solar point[1] for the planet as it traverses its orbit (or two orbits, in the case of a half integer resonance) and then computing the incident stellar flux as it varies across the illuminated hemisphere of the planet.

Dobrovolskis work highlights the relationship between orbital parameters and the distribution of sunlight for a handful of slow rotation rates (the whole and half-odd integer ratios from 1 to 4). Dobrovoskis work is motivated by trying to understand climate and habitability or exoplanets although no modeling appears in his studies.

In this chapter we contextualize what it means to be a rapidly rotating planet in terms of the insolation distribution. For the most part, we focus on the case where the obliquity and eccentricity are both zero, although we end with a few conjectures for more general orbital parameters.

3.1 What is "rapid" rotation?

Let ω be the number of rotations per revolution. We want to know how quickly the annual average insolation approaches the rapid rotation distribution as a function of ω. As we saw in the previous chapter, the annual average insolation on a rapidly rotating planet is rotationally symmetric about the planet's axis of rotation, in other words it is

[1] The sub-solar point is the point on the planet directly "below" the sun, i.e. the place where a vertical stick would have no shadow. For a tidally locked planet with zero obliquity, the sub-solar point would lie on the equator at 0° longitude (where the longitude is by convention).

constant for a fixed latitude. Then to compute how quickly the insolation distribution approaches the rapidly rotating distribution, we will compare the largest difference between the insolation distribution on a rapidly rotating planet with zero obliquity and eccentricity and the distribution for a planet with rotation rate ω. For planets with zero obliquity and eccentricity, this largest difference occurs at the equator, although the longitude of greatest difference varies depending on the rotation rate.

If $\tilde{I}(\phi, \lambda, \omega)$ represents the annual average insolation as a function of longitude ϕ, latitude λ, and rotation rate ω, then for rapidly rotating planets

$$\frac{1}{2\pi}\int_0^{2\pi} \tilde{I}(\phi, \sin(\lambda), \omega) = s(\sin(\lambda)) \tag{3.1}$$

In the following theorem, we can constrain the maximum difference between the annual average distribution of sunlight as a function of longitude, latitude, and rotation rate and the annual average distribution of sunlight as a function of latitude and rotation rate (averaged over longitude) for a planet on a circular orbit with no axial tilt. We see that the decay as the rotation rate increases is proportional to the inverse of the rotation rate.

Theorem 3.1.1. *For a planet on a circular orbit with zero obliquity, if*

- $\tilde{I}(\phi, \lambda, \omega)$ *represents the annual average insolation as a function of longitude* ϕ*, latitude* λ*, and rotation rate* ω*,*
- $\hat{I}(\lambda, \omega) = \frac{1}{2\pi}\int_0^{2\pi} \tilde{I}(\phi, \lambda, \omega) d\phi$ *is the average over all longitudes, and*
- $\omega > 1$*,*

then

$$\frac{2\,|\sin(\pi\omega)|}{\pi(\omega - 1)} \leq \sup_{\phi \in [0, 2\pi]} \|\tilde{I}(\phi, \lambda, \omega) - \hat{I}(\lambda, \omega)\|_{\mathcal{C}^0([-\pi/2, \pi/2])} \leq \frac{4\,|\sin(\pi\omega)|}{\pi(\omega - 1)}.$$

See Figure 3.1 for a visual representation of the bounds for this theorem.

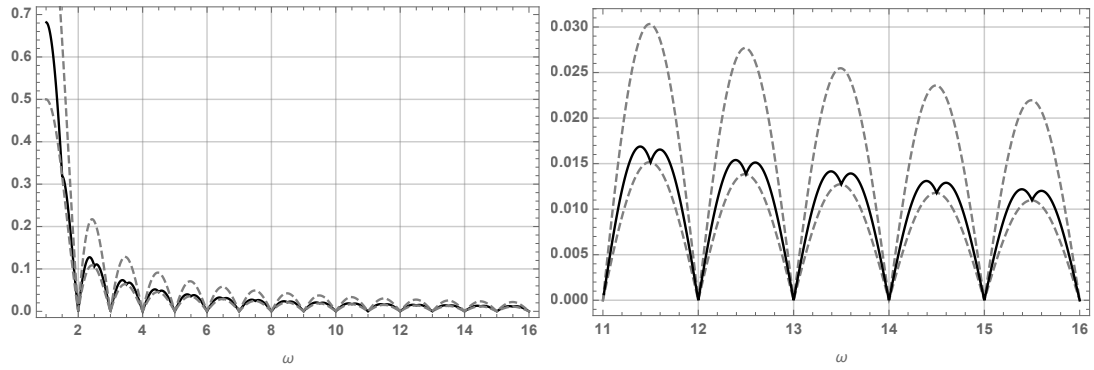

Figure 3.1: The value $\sup_{\phi\in[0,2\pi]} \|\tilde{I}(\phi,\lambda,\omega)-\hat{I}(\lambda,\omega)\|_{\mathcal{C}^0([-1,1]}$ plotted as a function of the rotation rate ω (solid, black curve) along with the bounds from Theorem 3.1.1 (dashed, gray curve). The right image is a zoomed version of the tail of the left image.

3.2 Annual Insolation Averaged over Longitude

Lemma 3.2.1. *For a planet on a circular orbit with zero obliquity, if $\tilde{I}(\phi,\lambda,\omega)$ represents the annual average insolation as a function of longitude ϕ, latitude λ, and rotation rate ω, then*

$$\hat{I}(\lambda,\omega) = \frac{1}{2\pi}\int_0^{2\pi} \tilde{I}(\phi,\lambda,\omega)d\phi = \frac{4\cos\lambda}{\pi} \tag{3.2}$$

for $\lambda \in [-\pi/2, \pi/2]$.

Proof. From Dobrovolskis' 2013 paper [13] we calculate the insolation away from the subsolar point where ξ is the angle of the star from the local zenith. The insolation is given by $\cos\xi$ on the sunlit side of the planet where

$$\cos\xi = \cos(\alpha+\nu)\cos(\phi+\Phi_0+\omega t)\cos(\lambda) \tag{3.3}$$

$$+\sin(\alpha+\nu)\sin(\phi+\Phi_0+\omega t)\cos(\lambda)\cos(\beta) \tag{3.4}$$

$$+\sin(\alpha+\nu)\sin(\lambda)\sin(\beta), \tag{3.5}$$

ν is the true anomaly and α and Φ_0 are parameters that denote the procession angle.

Since we are only considering a circular orbit with zero obliquity, we can set the procession parameters (α and Φ_0) and β to zero. Since eccentricity is zero we have the relationship $\nu = nt$ where n is the mean motion. For the duration we let $n = 1$. Then

$$\cos\xi = \cos(\lambda)\cos(\phi + (\omega - 1)\nu). \tag{3.6}$$

Since the insolation can never be negative, the insolation is computed by adding the absolute value of $\cos\xi$ to $\cos\xi$ and dividing the sum by 2, i.e. $(\cos\xi + |\cos\xi|)/2$. Further, we must account for the solar intensity at the subsolar point. The solar intensity is proportional to $1/r^2$ where r is the instantaneous distance from the planet to the sun along it's orbit. Since we are considering only a circular orbit, r is constant. We take $r = 1$ here for simplicity. In order to maintain agreement with insolation calculations in the mathematical literature, we must also multiply by 4. This ensures that the function is a distribution over latitude and longitude (i.e. integrates to 1). In particular, S_0 in Dobrovolskis' 2013 paper [13] is related to Q in McGehee and Lehman [29] by $Q = S_0/4$.

Then the average annual insolation as a function of longitude, latitude, and rotation rate is

$$\tilde{I}(\phi, \lambda, \omega) = \frac{1}{\pi}\int_0^{2\pi} (\cos(\lambda)\cos(\phi + (\omega - 1)\nu) + |\cos(\lambda)\cos(\phi + (\omega - 1)\nu)|)\, d\nu \tag{3.7}$$

$$= \frac{\cos\lambda}{\pi}\int_0^{2\pi} (\cos(\phi + (\omega - 1)\nu) + |\cos(\phi + (\omega - 1)\nu)|)\, d\nu \tag{3.8}$$

for $\lambda \in [-\pi/2, \pi/2]$.

If $\omega = 1$, then the integral becomes

$$\tilde{I}(\phi, \lambda, \omega) = \frac{\cos\lambda}{\pi}\int_0^{2\pi} (\cos(\phi) + |\cos(\phi)|)\, d\nu = 2\cos\lambda\,(\cos(\phi) + |\cos(\phi)|)\,. \tag{3.9}$$

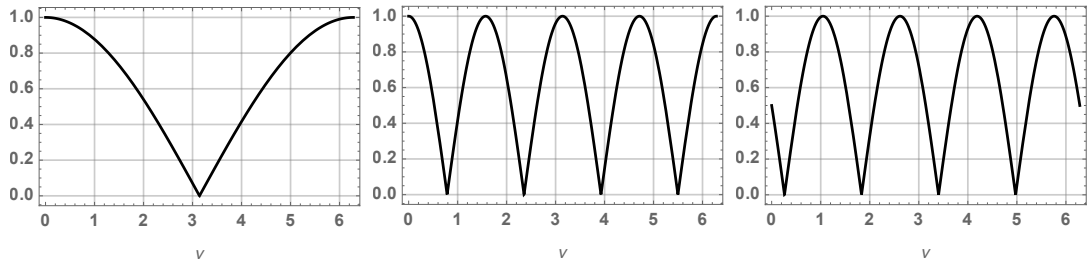

Figure 3.2: Plots of $|\cos(\phi + (\omega - 1)\nu)|$ with **Left:** $\phi = 0$, $\omega = 1.5$, **Center:** $\phi = 0$, $\omega = 3$, and **Right:** $\phi = \pi/3$, $\omega = 3$.

Averaging over ϕ yields

$$\hat{I}(\lambda, \omega) = \frac{\cos\lambda}{\pi} \int_0^{2\pi} (\cos(\phi) + |\cos(\phi)|)\, d\phi = \frac{\cos\lambda}{\pi} \cdot 4 = \frac{4\cos\lambda}{\pi}. \tag{3.10}$$

If $\omega \neq 1$ we compute the terms individually. Let

$$s_1(\phi, \omega) = \int_0^{2\pi} \cos(\phi + (\omega - 1)\nu) d\nu = \frac{2\cos(\phi + \pi\omega)\sin(\pi\omega)}{\omega - 1} \tag{3.11}$$

and

$$s_2(\phi, \omega) = \int_0^{2\pi} |\cos(\phi + (\omega - 1)\nu)|\, d\nu. \tag{3.12}$$

A plot of the integrand appears in Figure 3.2. Notice that ϕ shifts the function left or right and $(\omega - 1)$ changes the number of cosine bumps that appear in the interval $[0, 2\pi]$. For each bump the antiderivative is a sine function, but moving between adjacent bumps

requires adding a multiple of 2 to the antiderivative. Then

$$s_2(\phi,\omega) = \int_0^{2\pi} |\cos(\phi + (\omega-1)\nu)|\, d\nu \tag{3.13}$$

$$= \frac{1}{\omega-1}\left(\sin(u)\frac{|\cos(u)|}{\cos(u)} + 2m \text{ for } u \in \left[\frac{-\pi}{2}+\pi m, \frac{\pi}{2}+\pi m\right]\right)\Bigg|_{u_1(\phi)=\phi}^{u_2(\phi)=\phi+2\pi(\omega-1)} \tag{3.14}$$

$$= s_{22}(\phi,\omega) - s_{21}(\phi,\omega). \tag{3.15}$$

where the functions $s_{22}(\phi,\omega)$ and $s_{21}(\phi,\omega)$ indicate evaluation at the upper and lower bounds of the integral, respectively. Since $\phi \in [0, 2\pi]$ we have that $\phi + 2\pi(\omega-1) \in [2\pi(\omega-1), 2\pi + 2\pi(\omega-1)]$. The integer m is the smallest integer so that the domain of $u_i(\phi)$ intersected with $[-\pi/2 + \pi m, \pi/2 + \pi m)$ is nonempty. This means m is different for the upper and lower bounds.

The functions $s_{22}(\phi,\omega)$ and $s_{21}(\phi,\omega)$ are both piecewise defined. The form of $s_{21}(\phi,\omega)$ does not depend on ω and is always given by

$$s_{21}(\phi,\omega) = \begin{cases} \frac{\sin(\phi)}{\omega-1} & \phi \in [0, \frac{\pi}{2}) \\ \frac{2-\sin(\phi)}{\omega-1} & \phi \in [\frac{\pi}{2}, \frac{3\pi}{2}) \\ \frac{4+\sin(\phi)}{\omega-1} & \phi \in [\frac{3\pi}{2}, 2\pi] \end{cases}. \tag{3.16}$$

Because no ω term appears in $u_1(\phi)$, the domain of $u_1(\phi)$ is $[0, 2\pi]$ and $m = 0$.

On the other hand, the form of $s_{22}(\phi,\omega)$ depends the value of ω. If $2\pi(\omega-1) \in \left(-\frac{\pi}{2}+\pi m, \frac{\pi}{2}+\pi m\right)$ for some integer $m > 0$, then $s_2 2$ has three piecewise components

and

$$s_{22}(\phi,\omega) = \begin{cases} \frac{2m+\cos(\pi m)\sin(\phi+2\pi(\omega-1))}{\omega-1} & \phi \in [0, a(\omega)) \\ \frac{2(m+1)-\cos(\pi m)\sin(\phi+2\pi(\omega-1))}{\omega-1} & \phi \in [a(\omega), b(\omega)) \\ \frac{2(m+2)+\cos(\pi m)\sin(\phi+2\pi(\omega-1))}{\omega-1} & \phi \in [b(\omega), 2\pi] \end{cases} \tag{3.17}$$

$$= \begin{cases} \frac{2m+\cos(\pi m)\sin(\phi+2\pi\omega)}{\omega-1} & \phi \in [0, a(\omega)) \\ \frac{2(m+1)-\cos(\pi m)\sin(\phi+2\pi\omega)}{\omega-1} & \phi \in [a(\omega), b(\omega)) \\ \frac{2(m+2)+\cos(\pi m)\sin(\phi+2\pi\omega)}{\omega-1} & \phi \in [b(\omega), 2\pi] \end{cases} \tag{3.18}$$

where $a + 2\pi(\omega - 1) = \frac{\pi}{2} + \pi m$ implies $a(\omega) = \frac{\pi}{2}(2m - 4\omega + 5)$ and $b(\omega) = a(\omega) + \pi$. Note that the integer m satisfies the inequality $(4\omega - 5)/2 < m \leq (4\omega - 3)/2$.

Notice that when $\omega = (2m+3)/4$, then $2\pi(\omega - 1) = \pi m - \pi/2$ and $a(\omega) = \pi$, so the third piecewise term collapses to a point and we have

$$s_{22}(\phi, (2m+3)/4) = \begin{cases} \frac{2m+\cos(\pi m)\sin(\phi+\pi(2m+3)/2)}{-1+(2m+3)/4} & \phi \in [0, \pi) \\ \frac{2m+2-\cos(\pi m)\sin(\phi+\pi(2m+3)/2)}{-1+(2m+3)/4} & \phi \in [\pi, 2\pi] \end{cases}. \tag{3.19}$$

In summary

$$\tilde{I}(\phi, \lambda, \omega) = \frac{\cos\lambda}{\pi}\left(s_1(\phi,\omega) + s_{22}(\phi,\omega) - s_{21}(\phi,\omega)\right). \tag{3.20}$$

To integrate this function in ϕ, we need only tools from calculus, so the intervening steps are omitted. It is straightforward to show that

$$\frac{1}{2\pi}\int_0^{2\pi} s_1(\phi,\omega)d\phi = 0, \tag{3.21}$$

$$\frac{1}{2\pi}\int_0^{2\pi} s_{21}(\phi,\omega)d\phi = \frac{2}{\omega-1}, \text{ and} \tag{3.22}$$

$$\frac{1}{2\pi}\int_0^{2\pi} s_{22}(\phi,\omega)d\phi = \frac{4\omega-2}{\omega-1}. \tag{3.23}$$

Then we have

$$\frac{1}{2\pi}\int_0^{2\pi}\tilde{I}(\phi,\lambda,\omega)d\phi = \frac{1}{2\pi}\int_0^{2\pi}\left(\frac{\cos\lambda}{\pi}\left(s_1(\phi,\omega)+s_{22}(\phi,\omega)-s_{21}(\phi,\omega)\right)\right) \tag{3.24}$$

$$= \frac{\cos\lambda}{\pi}\left(0+\frac{4\omega-2}{\omega-1}-\frac{2}{\omega-1}\right) \tag{3.25}$$

$$= \frac{4\cos\lambda}{\pi}. \tag{3.26}$$

Thus $\hat{I}(\lambda,\omega) = 4\cos\lambda/\pi$ for any ω. □

To compare to other results, we convert the variable to sine of the latitude. This yields

$$\hat{I}(\eta,\omega) = \frac{4\sqrt{1-\eta^2}}{\pi} \tag{3.27}$$

which agrees with the annual average insolation distribution as a function of sine of latitude gotten from McGehee and Lehman [29]. In particular, one computes the insolation distribution for a rapidly rotating planet with zero obliquity on a circular orbit using equation (2.2) with $\zeta = 1$. We see

$$s(\eta,1) = \frac{2}{\pi^2}\int_0^{2\pi}\sqrt{1-\left(\sqrt{1-\eta^2}\sqrt{1-(1)^2}\cos\gamma-\eta(1)\right)^2}d\gamma = \frac{4}{\pi}\sqrt{1-\eta^2}. \tag{3.28}$$

This means that averaging over the longitude results in the same distribution as if we assumed that the planet was rapidly rotating (for planets with zero obliquity on circular orbits). Then comparing the difference between $\tilde{I}(\phi,\lambda,\omega)$ and $\hat{I}(\lambda,\omega)$ tells us how similar the distribution $\tilde{I}(\phi,\lambda,\omega)$ is to a rapidly rotating distribution.

3.3 Absolute Difference of Insolation Averages

In this section we'll discuss the difference of the insolation averages $\tilde{I}(\phi,\lambda,\omega)$ (annual average as a function of longitude, latitude, and rotation rate) and $\hat{I}(\lambda,\omega)$ (annual

latitudinal averages). We have

$$\left|\tilde{I}(\phi,\lambda,\omega)-\hat{I}(\lambda,\omega)\right| = \left|\tilde{I}(\phi,\lambda,\omega)-\frac{4\cos\lambda}{\pi}\right| \tag{3.29}$$

$$= 4\left|\cos\lambda\right|\left|\frac{s_1(\phi,\omega)}{4\pi}+\frac{s_{22}(\phi,\omega)}{4\pi}-\frac{s_{21}(\phi,\omega)}{4\pi}-\frac{1}{\pi}\right|. \tag{3.30}$$

Define $f(\phi,\omega)$ as

$$f(\phi,\omega)=\frac{s_1(\phi,\omega)}{4\pi}+\frac{s_{22}(\phi,\omega)}{4\pi}-\frac{s_{21}(\phi,\omega)}{4\pi}-\frac{1}{\pi}. \tag{3.31}$$

Recall that $s_{21}(\phi,\omega)$ and $s_{22}(\phi,\omega)$ are both piecewise defined and that the parts of $s_{22}(\phi,\omega)$ depend on the value of ω. If $a(\omega)<\pi/2$ then

$$s_{22}(\phi,\omega)-s_{21}(\phi,\omega) \tag{3.32}$$

$$= \begin{cases} \frac{1}{\omega-1}\left(2m+\cos(\pi m)\sin(\phi+2\pi\omega)-\sin\phi\right) & \phi\in[0,a(\omega)) \\ \frac{1}{\omega-1}\left(2m+2-\cos(\pi m)\sin(\phi+2\pi\omega)-\sin\phi\right) & \phi\in[a(\omega),\pi/2) \\ \frac{1}{\omega-1}\left(2m+2-\cos(\pi m)\sin(\phi+2\pi\omega)-2+\sin\phi\right) & \phi\in[\pi/2,b(\omega)) \\ \frac{1}{\omega-1}\left(2m+4+\cos(\pi m)\sin(\phi+2\pi\omega)-2+\sin\phi\right) & \phi\in[b(\omega),3\pi/2) \\ \frac{1}{\omega-1}\left(2m+4+\cos(\pi m)\sin(\phi+2\pi\omega)-4-\sin\phi\right) & \phi\in[3\pi/2,2\pi] \end{cases} \tag{3.33}$$

and if $a(\omega) > \pi/2$ we have

$$s_{22}(\phi,\omega) - s_{21}(\phi,\omega) \tag{3.34}$$

$$= \begin{cases} \frac{1}{\omega-1}\left(2m + \cos(\pi m)\sin(\phi + 2\pi\omega) - \sin\phi\right) & \phi \in [0, \pi/2) \\ \frac{1}{\omega-1}\left(2m + \cos(\pi m)\sin(\phi + 2\pi\omega) - 2 + \sin\phi\right) & \phi \in [\pi/2, a(\omega)) \\ \frac{1}{\omega-1}\left(2m + 2 - \cos(\pi m)\sin(\phi + 2\pi\omega) - 2 + \sin\phi\right) & \phi \in [a(\omega), 3\pi/2) \\ \frac{1}{\omega-1}\left(2m + 2 - \cos(\pi m)\sin(\phi + 2\pi\omega) - 4 - \sin\phi\right) & \phi \in [3\pi/2, b(\omega)) \\ \frac{1}{\omega-1}\left(2m + 4 + \cos(\pi m)\sin(\phi + 2\pi\omega) - 4 - \sin\phi\right) & \phi \in [b(\omega), 2\pi] \end{cases} \tag{3.35}$$

3.3.1 Bounds

Lemma 3.3.1. *Fix $\omega \in [n, n + 1/2]$ and let $\phi^* = (2 + n - \omega)\pi$. Then*

(i) $\phi^* \in [\frac{3\pi}{2}, 2\pi]$,

(ii) $\frac{|\sin(\pi\omega)|}{2\pi(\omega-1)} \leq |f(\phi^*, \omega)| \leq \frac{|\sin(\pi\omega)|}{\pi(\omega-1)}$, *and*

(iii) $|f(\phi, \omega)| \leq |f(\phi^*, \omega)|$ *for all* $\phi \in [0, 2\pi]$.

Proof. For $\omega \in [n, n + 1/2]$, we clearly have that $3/2 \leq 2 + n - \omega \leq 2$, so (i) is true.

Recall that m is the integer that satisfies

$$\frac{4\omega - 5}{2} < m \leq \frac{4\omega - 3}{2}, \tag{3.36}$$

so we have $m = 2n - 2$ for $\omega \in [n, n + 1/4)$ and $m = 2n - 1$ for $\omega \in [n + 1/4, n + 1/2]$. We break up the proof into these two cases.

Suppose $\omega \in [n, n + 1/4)$. Then

$$0 = 2(2n - 2) - 4(n + 1/4) + 5 \leq \frac{2}{\pi}a(\omega) \leq 2(2n - 2) - 4n + 5 = 1, \tag{3.37}$$

so $s_{22}(\phi,\omega) - s_{21}(\phi,\omega)$ takes the form of (3.33).

To show (ii), first we evaluate f at ϕ^*. We have

$$f(\phi^*,\omega) = \frac{2\cos(\phi^* + \pi\omega)\sin(\pi\omega) + 2m + \sin(\phi^* + 2\pi\omega) - \sin\phi^* - 4(\omega-1)}{4\pi(\omega-1)} \tag{3.38}$$

$$= \frac{4\cos(\pi n)\sin(\pi\omega) + 2m - 4(\omega-1)}{4\pi(\omega-1)} \tag{3.39}$$

Notice that if n is even then $\sin(\pi\omega) > 0$ and $\cos(n\pi) > 0$ and if n is odd we have $\sin(\pi\omega) < 0$ and $\cos(n\pi) < 0$. Then

$$f(\phi^*,\omega) = \frac{4\left|\sin(\pi\omega)\right| + 2m - 4(\omega-1)}{4\pi(\omega-1)} \tag{3.40}$$

We have that

$$-1 < 2m - 4\omega + 4 \leq 0 \tag{3.41}$$

for $\omega \in [n, n+1/4)$. Then the upper inequality in (ii) is clear, namely we have

$$\left|f(\phi^*,\omega)\right| = \left|\frac{4\left|\sin(\pi\omega)\right| + 2m - 4(\omega-1)}{4\pi(\omega-1)}\right| \tag{3.42}$$

$$\leq \left|\frac{4\left|\sin(\pi\omega)\right|}{4\pi(\omega-1)}\right| \tag{3.43}$$

$$= \frac{\left|\sin(\pi\omega)\right|}{\pi(\omega-1)} \tag{3.44}$$

The lower inequality holds provided $\left|2m - 4(\omega-1)\right| < 2\left|\sin(\pi\omega)\right|$. We know that $\sin(\pi x) \leq 2x \leq 0$ for $x \in [-1/2, 0]$ which implies $2\left|\sin(\pi x)\right| > 4\left|x\right|$ for $x \in [-1/2, 0]$. Furthermore, we have

$$-1/4 < \left(\frac{m}{2} - (\omega-1)\right) \leq 0. \tag{3.45}$$

So we see that

$$|2m - 4(\omega - 1)| = 4\left|\frac{m}{2} - (\omega - 1)\right| \leq 2\left|\sin\left(\frac{m}{2}\pi - (\omega - 1)\pi\right)\right| = 2\left|\sin(\pi\omega)\right|. \quad (3.46)$$

To show (iii), notice that f is continuously differentiable in ϕ with derivative

$$\frac{\partial f}{\partial \phi}(\phi, \omega) = \begin{cases} \frac{1}{4\pi(\omega-1)}\left(-4\sin(\pi\omega)\sin(\phi + \pi\omega)\right) & \phi \in [0, a(\omega)) \\ \frac{1}{4\pi(\omega-1)}\left(-2\cos\phi\right) & \phi \in [a(\omega), \pi/2) \\ 0 & \phi \in [\pi/2, b(\omega)) \\ \frac{1}{4\pi(\omega-1)}\left(2\cos(\phi + 2\pi\omega)\right) & \phi \in [b(\omega), 3\pi/2) \\ \frac{1}{4\pi(\omega-1)}\left(-4\sin(\pi\omega)\sin(\phi + \pi\omega)\right) & \phi \in [3\pi/2, 2\pi] \end{cases}. \quad (3.47)$$

The function $\partial_\phi f(\phi, \omega)$ is continuous in ϕ on the interval $[0, 2\pi]$ and periodic at the boundary, i.e. $\partial_\phi f(0, \omega) = \partial_\phi f(2\pi, \omega)$

It is straightforward to show that $\partial_\phi f(\phi^*, \omega) = 0$ and if $\phi \notin E(\omega) = [\pi/2, b(\omega)) \cup \{\phi^*\}$, then $\partial_\phi f(\phi, \omega) \neq 0$. So f has no local extrema in $([\pi/2, b(\omega)) \cup \{\phi^*\})^C$. As long as f on $E(\omega)$ is greater than or equal to f on the boundary, we have that f has global extrema for $\phi \in E(\omega)$.

On the boundary

$$f(0, \omega) = f(2\pi, \omega) = \frac{4\left|\cos(\pi\omega)\sin(\pi\omega)\right| + 2m - 4(\omega - 1)}{4\pi(\omega - 1)} \quad (3.48)$$

because $\cos(\pi\omega)$ and $\sin(\pi\omega)$ have the same sign for $\omega \in [n, n + 1/4)$. We see

$$f(\phi^*, \omega) - f(2\pi, \omega) = \frac{4\left|\sin(\pi\omega)\right|\left(1 - \left|\cos(\pi\omega)\right|\right) + 2m - 4(\omega - 1)}{4\pi(\omega - 1)} \geq 0. \quad (3.49)$$

So the global extrema of f are on $E(\omega)$.

It remains to show that $|f(\phi^*, \omega)| \geq |f(\phi, \omega)|$ for $\phi \in [\pi/2, b(\omega))$. On the interval

$[\pi/2, b(\omega))$, f is constant with

$$f(\phi,\omega) = \frac{2m - \sin(\phi + 2\pi\omega) + \sin\phi + 2\cos(\phi + \pi\omega)\sin(\pi\omega) - 4(\omega - 1)}{4\pi(\omega - 1)} \tag{3.50}$$

$$= \frac{2m - 4(\omega - 1)}{4\pi(\omega - 1)} \tag{3.51}$$

Then by the same argument as in equation (3.46), we have that

$$|f(\phi,\omega)| \leq \frac{|\sin(\pi\omega)|}{2\pi(\omega - 1)} \leq |f(\phi^*,\omega)| \tag{3.52}$$

for $\phi \in [\pi/2, b(\omega))$. Thus $|f(\phi,\omega)| \leq |f(\phi^*,\omega)|$ for all $\phi \in [0, 2\pi]$ when $\omega \in [n, n + 1/4)$.

Now suppose $\omega \in [n + 1/4, n + 1/2]$. Then $m = 2n - 1$ and

$$1 = 2(2n-1) - 4(n + 1/2) + 5 \leq \frac{2}{\pi}a(\omega) \leq 2(2n-1) - 4(n + 1/4) + 5 = 3, \tag{3.53}$$

so $s_{22}(\phi,\omega) - s_{21}(\phi,\omega)$ takes the form of (3.35). Furthermore,

$$b(\omega) - \phi^* = \frac{\pi}{2}m > 0 \tag{3.54}$$

so $\phi^* \in [\pi/2, b(\omega))$ and

$$f(\phi^*,\omega) = \frac{4\,|\sin(\pi\omega)| + 2m - 2 - 4(\omega - 1)}{4\pi(\omega - 1)} \tag{3.55}$$

Notice that

$$-2 \leq 2m - 2 - 4(\omega - 1) \leq -1 \tag{3.56}$$

for $\omega \in [n + 1/4, n + 1/2]$. Then the upper bound is clear. For the lower bound, notice

that

$$-1/2 \leq \frac{m-1}{2} - (\omega - 1) \leq -1/4, \tag{3.57}$$

so we can use the same argument as for equation (3.46) to say $|2m - 2 - 4(\omega - 1)| \leq 2\,|\sin(\omega\pi)|$, giving us the lower bound. Thus (ii) is shown for $\omega \in [n + 1/4, n + 1/2]$.

To show (iii) for $\omega \in [n + 1/4, n + 1/2]$, we again observe that f is continuously differentiable in ϕ with derivative

$$\frac{\partial f}{\partial \phi}(\phi, \omega) = \begin{cases} \frac{1}{4\pi(\omega-1)}\,(-2\cos\phi) & \phi \in [0, \pi/2) \\ 0 & \phi \in [\pi/2, a(\omega)) \\ \frac{1}{4\pi(\omega-1)}\,(2\cos(\phi + \pi\omega)\cos(\pi\omega)) & \phi \in [a(\omega), 3\pi/2) \\ \frac{1}{4\pi(\omega-1)}\,(-4\sin(\phi + \pi\omega)\sin(\pi\omega)) & \phi \in [3\pi/2, b(\omega)) \\ \frac{1}{4\pi(\omega-1)}\,(-2\cos\phi) & \phi \in [b(\omega), 2\pi] \end{cases} \tag{3.58}$$

The function $\partial_\phi f(\phi, \omega)$ is continuous in ϕ on the interval $[0, 2\pi]$ and periodic at the boundary, i.e. $\partial_\phi f(0, \omega) = \partial_\phi f(2\pi, \omega)$

It is straightforward to show that $\partial_\phi f(\phi^*, \omega) = 0$ and if $\phi \notin E_a(\omega) = [\pi/2, a(\omega)) \cup \{\phi^*\}$, then $\partial_\phi f(\phi, \omega) \neq 0$. So f has no local extrema in $([\pi/2, a(\omega)) \cup \{\phi^*\})^C$. As long as f on $E_a(\omega)$ is greater than or equal to f on the boundary, we have that f has global extrema for $\phi \in E(\omega)$.

On the boundary

$$f(0, \omega) = f(2\pi, \omega) = \frac{2\cos(\pi\omega)\sin(\pi\omega) + 2m - \sin(2\pi\omega) - 4(\omega - 1)}{4\pi(\omega - 1)} \tag{3.59}$$

$$= \frac{2m - 4(\omega - 1)}{4\pi(\omega - 1)} \tag{3.60}$$

We see

$$f(\phi^*, \omega) - f(2\pi, \omega) = \frac{4\,|\sin(\pi\omega)|}{4\pi(\omega - 1)} \geq 0. \tag{3.61}$$

So the global extrema of f are on $E_a(\omega)$.

It remains to show that $|f(\phi^*, \omega)| \geq |f(\phi, \omega)|$ for $\phi \in [\pi/2, a(\omega))$. On the interval $[\pi/2, a(\omega))$, f is constant with

$$f(\phi, \omega) = \frac{2m - 4(\omega - 1)}{4\pi(\omega - 1)} \tag{3.62}$$

as was the case when $\omega \in [n, n + 1/4)$. Then by the same argument, we have that

$$|f(\phi, \omega)| \leq \frac{|\sin(\pi\omega)|}{2\pi(\omega - 1)} \leq |f(\phi^*, \omega)| \tag{3.63}$$

for $\phi \in [\pi/2, b(\omega))$. Thus $|f(\phi, \omega)| \leq |f(\phi^*, \omega)|$ for all $\phi \in [0, 2\pi]$ when $\omega \in [n, n + 1/4)$. □

Similar results hold for $\omega \in [n + 1/2, n + 1]$. Since the proof is nearly identical, we present only the result here.

Lemma 3.3.2. *Fix $\omega \in [n + 1/2, n + 1]$ and let $\phi^* = (1 + n - \omega)\pi$. Then*

(i) $\phi^* \in [0, \frac{\pi}{2}]$,

(ii) $\frac{|\sin(\pi\omega)|}{2\pi(\omega-1)} \leq |f(\phi^*, \omega)| \leq \frac{|\sin(\pi\omega)|}{\pi(\omega-1)}$, *and*

(iii) $|f(\phi, \omega)| \leq |f(\phi^*, \omega)|$ *for all* $\phi \in [0, 2\pi]$.

3.4 Proof of Theorem 3.1.1

Proof of Theorem 3.1.1. From Lemma 3.2.1 we know that

$$\frac{1}{2\pi}\int_0^{2\pi} \tilde{I}(\phi,\lambda,\omega)d\phi = \frac{4\cos\lambda}{\pi}. \tag{3.64}$$

Noice that

$$\left\|\tilde{I}(\phi,\lambda,\omega) - \frac{4\cos\lambda}{\pi}\right\|_{\mathcal{C}^0} = \sup_{\lambda\in[-\pi/2,\pi/2]}\left|\tilde{I}(\phi,\lambda,\omega) - \frac{\cos\lambda}{\pi}\right| \tag{3.65}$$

$$= \sup_{\lambda\in[-\pi/2,\pi/2]} 4\left|\cos\lambda\right|\left|\frac{s_1(\phi,\omega)}{4\pi} + \frac{s_2(\phi,\omega)}{4\pi} - \frac{1}{\pi}\right| \tag{3.66}$$

$$= 4\left|\frac{s_1(\phi,\omega)}{4\pi} + \frac{s_2(\phi,\omega)}{4\pi} - \frac{1}{\pi}\right| \tag{3.67}$$

$$= 4\left|f(\phi,\omega)\right| \tag{3.68}$$

By Lemma 3.3.1 and Lemma 3.3.2, we have

$$4\frac{|\sin(\pi\omega)|}{2\pi(\omega-1)} \le 4\left|f(\phi,\omega)\right| \le 4\frac{|\sin(\pi\omega)|}{\pi(\omega-1)} \tag{3.69}$$

for all $\phi \in [0, 2\pi]$ as desired. □

3.5 Discussion

In this chapter we've provided a measure of how close a planet's insolation distribution is to a rapidly rotating planet on the same orbit. We restrict to the case where the planet is on a circular orbit with no obliquity. We show that the decay to rapid rotation insolation distribution is proportional to the reciprocal of the rotation rate in the $\mathcal{C}^0$ norm. It may be interesting to consider how this decays in other norms, but we leave that for further study.

Planets on a circular orbit with zero obliquity with an integer number of rotations

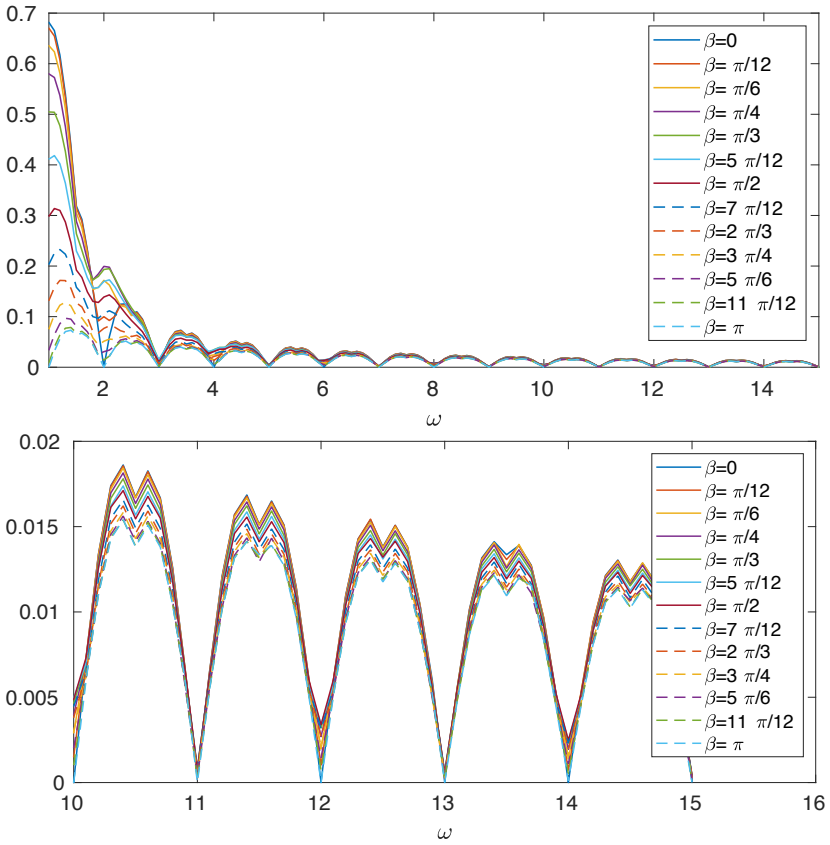

Figure 3.3: The value $\sup_{\phi\in[0,2\pi]} \|\tilde{I}(\phi,\lambda,\omega,\beta) - \hat{I}(\lambda,\omega,\beta)\|_{\mathcal{C}^0([-1,1]}$ plotted as a function of the rotation rate ω for 13 different obliquities.

n per revolution have the same insolation distribution as rapidly rotation planets as long as $n > 1$. This is true because each point on the planet sees the sun for the same amount of time and at the same intensity (for fixed latitude). Then we suspect that for a planet on a circular orbit with zero obliquity with rotation rate $\omega = p/q > 1$ (i.e. p rotations every q revolutions), that averaging over q revolutions should also give the same result as a rapidly rotating planet. We formalize this in the following conjecture.

Conjecture 3.5.1. *On a circular orbit with zero obliquity, if $\omega = p/q > 1$; $\tilde{I}_q(\phi, \lambda, p/q)$ represents the average insolation over q revolutions as a function of longitude ϕ, latitude λ, and rotation rate ω; and $\hat{I}(\lambda, p/q) = \frac{1}{2\pi}\int_0^{2\pi} \tilde{I}_1(\phi, \lambda, p/q)d\phi$; then*

$$\sup_{\phi\in[0,2\pi]} \|\tilde{I}_q(\phi, \lambda, p/q) - \hat{I}(\lambda, p/q)\|_{\mathcal{C}^0([-\pi/2,\pi/2]} = 0.$$

For nonzero obliquities, it's possible to plot the dependence on the rotation rate even though we haven't yet proven any analytical bounds. In Figure 3.3 we see how changing the obliquity affects how close the insolation distribution is to a rapidly rotating planet. These figures motivate the following conjecture.

Conjecture 3.5.2. *On a circular orbit, if $\tilde{I}(\phi, \lambda, \omega, \beta)$ represents the annual average insolation as a function of longitude ϕ, latitude λ, rotation rate ω, and obliquity β; $\hat{I}(\lambda, \omega, \beta) = \frac{1}{2\pi}\int_0^{2\pi} \tilde{I}(\phi, \lambda, \omega, \beta)d\phi$; $\omega > 1$; and $\beta \in [0, \pi]$; then*

$$\frac{4\,|\sin(\pi\omega)|}{\pi(\omega+1)} \leq \sup_{\phi\in[0,2\pi]} \|\tilde{I}(\phi, \lambda, \omega, \beta) - \hat{I}(\lambda, \omega, \beta)\|_{\mathcal{C}^0([-1,1]} \leq \frac{4}{\pi(\omega-1)}. \tag{3.70}$$

There may be stricter bounds that one could impose that depend on the obliquity.

Chapter 4

Energy Balance Model of Earth with Two Ice Lines

There is a rich literature which began in the late 1960's and early 1970's and continues to today which uses energy balance models (EBMs) to study the feedback between albedo and surface temperature on Earth [6, 38]. Studies within the literature which use these types of models assume a hemispheric symmetry of the planet either about the equator [2, 36, 29, 30, 47] or about 180° of longitude [8]. In studying the location and abundance of ice, these studies constrain their investigations to a single ice edge in one hemisphere of the planet and assume, in the case where symmetry is about the equator, that a mirror image is present in the other hemisphere. This assumption limits the type of solutions one can find—only symmetric solutions exist—and the interpretations of results.

In this study we develop a framework to remove the restriction of symmetry in a latitude-dependent Budyko-Sellers type EBM. The framework is general enough to be applied broadly; however, here we specifically focus on Earth in order to understand the stability of symmetric ice line configurations on Earth. In the following chapter we discss adaptions of the model that may make it applicable to Pluto in order to highlight

a major breakthrough from removing the symmetry restriction: stable, asymmetric configurations of ice on the planet. We suspect that these asymmetric, stable solutions persist for a range of orbital parameters; however we leave the details of that supposition to further study.

4.1 Description of the model

The energy balance equation describes the evolution of the annual average temperature $T(y,t)$ on a rapidly rotating planet where t denotes time in years and y denotes the sine of the latitude. The planet's south pole is at $y=-1$ and its north pole is at $y=1$. The temperature evolves based on the equation

$$R\frac{\partial T}{\partial t} = Qs(y,\beta)(1-\alpha(y,\eta)) - (A+BT(y,t)) - C\left(T(y,t)-\overline{T}(t)\right), \tag{4.1}$$

where the change in temperature is determined by the absorbed solar radiation (the term given by $Qs(y,\beta)(1-\alpha(y,\eta))$), the emitted longwave radiation $(A+BT(y,t))$, and energy transport across latitudes $(C\left(T(y,t)-\overline{T}(t)\right))$. The parameter R is the heat capacity of the planet's surface layer.

The annual average insolation is denoted by Q and the distribution of the annual insolation across the sine of the latitude y dependent on the obliquity of the planet β is given by $s(y,\beta)$. As was shown in Chapter 2, the insolation distribution for any rapidly rotating planet with obliquity β is well approximated by the sixth degree polynomial

$$s(y,\beta) \approx \sigma_6(y,\beta) = 1 - s_2p_2(\cos\beta)p_2(y) - s_4p_4(\cos\beta)p_4(y) - s_6p_6(\cos\beta)p_6(y) \tag{4.2}$$

where $s_2 = 5/8$, $s_4 = 9/64$, and $s_6 = 65/1024$ and the p_k's are the Legendre polynomials

$$p_2(y) = (3y^2 - 1)/2, \tag{4.3}$$

$$p_4(y) = (35y^4 - 30y^2 + 3)/8, \tag{4.4}$$

$$p_6(y) = (231y^6 - 315y^4 + 105y^2 - 5)/16. \tag{4.5}$$

The surface albedo is given by $\alpha(y, \eta)$, which depends on the sine of latitude y and the location of ice on the planet η. In this study we take $\eta = (\eta_S, \eta_N)$, which gives the location of a southern (η_S) and northern (η_N) ice line. We restrict the ice lines to the interval $[-1, 1]$ with the condition $-1 \leq \eta_S \leq \eta_N \leq 1$ (i.e. we do not let the ice lines cross each other). We consider a piecewise constant albedo function given by

$$\alpha(y, \eta) = \begin{cases} \alpha_2, & y < \eta_S \\ (\alpha_1 + \alpha_2)/2, & y = \eta_S \\ \alpha_1, & \eta_S < y < \eta_N \\ (\alpha_1 + \alpha_2)/2, & y = \eta_N \\ \alpha_2, & \eta_N < y \leq 1 \end{cases}. \tag{4.6}$$

For planets with ice caps, we take $\alpha_1 < \alpha_2$ so that the regions poleward of the ice lines are more reflective. This is depicted in Figure 4.1. For planets with an ice belt, we take $\alpha_2 < \alpha_1$, indicating that the region between the ice lines is more reflective than the regions poleward of the ice lines.

In the longwave radiation term, A and B parameterize the outgoing longwave radiation based on the planet's surface temperature. The parameter A is generally referred to as the greenhouse gas parameter. K. K. Tung discusses how one would derive this linear term from the Stefan-Boltzmann law in Chapter 8 of his book [41]. Tung also notes that, at least for Earth, the linear relationship between surface temperature and outgoing radiation is confirmed by satellite data [41] (see, for example, [22]). Kaper

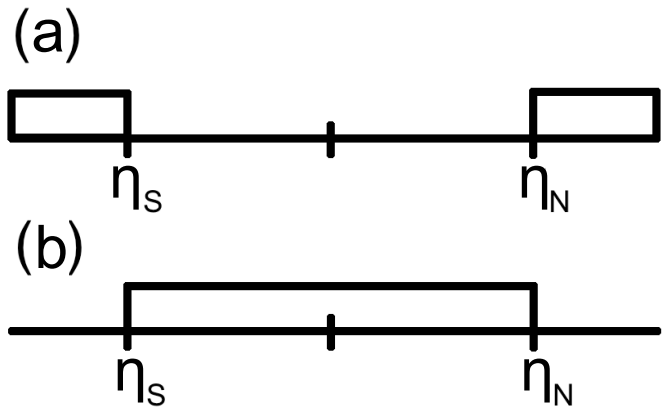

Figure 4.1: Set up with ice caps (a) or an ice belt (b). The ice lines η_S and η_N can move left or right on the interval $[-1, 1]$ as long as $\eta_S \leq \eta_N$.

and Engler note in in Chapter 2 of their book that linearizing the Stefan-Boltzmann law overestimates the values of A and B for Earth gotten from this satellite data [25].

The energy transport term is a simple linear relaxation to the mean annual global temperature. In this term, $\overline{T}(t) = \frac{1}{2}\int_{-1}^{1} T(y,t)dy$ is the global mean annual global temperature and C is an empirical parameter used to fit solutions the current climate of Earth [41]. Although heat is transported across the planet's surface through many complex processes, similar studies have shown that this for approximation reproduces useful and relevant results when applied to Earth ([2, 8, 30, 47] among others). Alternatively, one can model heat transport using a diffusion term (for example, recently in [36]); however we do not explored that possibility in this study. Instead we chose to focus on the relaxation to the mean in order to situate the results firmly within that literature and leave diffusion to future exploration.

In addition to equation (4.1) we consider two dynamic ice line equations in the fashion of Widiasih's single ice line equation [47]. In particular, the movement of an ice line is determined by the temperature at the ice line relative to a critical temperature

T_c, the highest temperature at which ice is present year round. For ice caps, we have

$$\begin{aligned} \frac{d\eta_S}{dt} &= \rho(T_c - T(\eta_S, t)), \\ \frac{d\eta_N}{dt} &= \rho(T(\eta_N, t) - T_c). \end{aligned} \tag{4.7}$$

Notice that if $T(\eta_S, t) > T_c$ then the temperature at the southern ice line is greater than the critical temperature and there must be melting (or sublimation) at η_S. If the edge of the southern ice cap is melting, then it moves toward the south pole. If instead we have $T(\eta_S, t) < T_c$ then it is colder than the critical temperature at η_S which means more ice can form and that the ice line moves toward the north pole. The northern ice line moves in a similar manner. To realize this movement with our equations, the northern ice line governing equation is multiplied by -1 so that ice formation ($T(\eta_N, t) < T_c$) or degradation ($T(\eta_N, t) > T_c$) results in the ice line moving in the proper direction.

In the case of a planet with an ice belt, one should multiply the right hand side of each equation in (4.7) by -1 so that the movement of both ice lines is in the opposite direction. For example, if the η_S equation were multiplied by -1, then when $T(\eta_S, t) > T_c$ we have that the ice line η_S should move towards 1, i.e. the southern edge of the ice belt melts back toward the north pole. This is described in more detail in Chapter 5.

The parameter ρ controls how fast the ice line changes relative to changes in temperature. Note that the parameter ρ must always be positive. For $\rho = 0$, the ice lines do not move when the temperature changes (which is nonphysical) and instead the temperature changes relative to the placement of the ice on the planet. In the limit as ρ goes to infinity, the ice lines adjust instantaneously to changes in temperature (which is also nonphysical). In their discussion of glacial cycles on Earth, McGehee and Widiasih give an in depth discussion on behavior of solutions of a similar EBM relative to the choice of ρ [30].

The values for the Budyko parameters are given in Table 4.1

Table 4.1: Parameter values used in the standard Budyko-Widiasih model.

Parameter	Name	Value for Earth	Units
R	Surface layer heat capacity	12.6	$\mathrm{Wm^{-2}K^{-1}}$
Q	Annual average insolation	343	$\mathrm{Wm^{-2}}$
β	Obliquity	23.5	degrees
α_1	Albedo between the ice lines	.32	dimensionless
α_2	Albedo poleward of the ice lines	.62	dimensionless
A	Greenhouse Gas parameter	202	$\mathrm{Wm^{-2}}$
B	Outgoing radiation	1.9	$\mathrm{Wm^{-2}K^{-1}}$
C	Heat transport	3.04	$\mathrm{Wm^{-2}K^{-1}}$
T_c	Critical temperature	-10	$^\circ$C
ρ	Ice line response to temperature change	varies	$\mathrm{K^{-1}yr^{-1}}$

4.1.1 Motion of the Ice Lines at Physical Boundaries

Due to the physical constraints of the planet, the ice lines cannot be less than -1 or greater than 1, even though the dynamic ice line equations (4.7) are defined for all real numbers. To constrain the ice lines within the physical boundary of the planet, we follow the approach outlined in [2].

Consider, for example, the southern ice line η_S. As η_S evolves, if $\eta_S(t) = -1$ and $T(\eta_S, t) > T_c$, then the governing equations dictate that the southern ice line should melt and move to the left of -1. Since this is not allowed by the physical constraints of the planet, we instead require that the southern ice line stop at $\eta_S = -1$ but continue to let η_N and T evolve as dictated by the equations. If at some time the temperature at the pole cools below the critical temperature, then the southern ice line grows towards the north pole as dictated by the governing equations. Similar behavior happens if the northern ice line, η_N reaches the north pole ($\eta_N = 1$).

If the ice lines come together ($\eta_S = \eta_N$), then we continue to let T evolve as dictated by (4.1). Note that in the ice cap scenario, the ice lines coming together means that the planet is completely covered in ice (commonly referred to as "Snowball Earth"). If at some time the temperature at this latitude rises above the critical temperature then the ice lines reform and move as dictated in (4.7).

Due to the piecewise continuous albedo function, T will have discontinuities at the ice lines. In particular, the temperature profile has the form

$$T(y,t) = \begin{cases} T_1(y,t), & y < \eta_S \\ T_2(y,t), & \eta_S < y < \eta_N \\ T_3(y,t), & y > \eta_N \end{cases}$$

were we impose the conditions

$$\begin{aligned} T(\eta_S,t) &= \frac{\lim_{y\to\eta_S^+} T(y,t) + \lim_{y\to\eta_S^-} T(y,t)}{2}, \text{ and} \\ T(\eta_N,t) &= \frac{\lim_{y\to\eta_N^+} T(y,t) + \lim_{y\to\eta_N^-} T(y,t)}{2}. \end{aligned} \tag{4.8}$$

at the ice lines as is common in other studies [2, 29, 47]. When $\eta_S \neq \eta_N$ this condition is

$$\begin{aligned} T(\eta_S,t) &= \frac{\lim_{y\to\eta_S^+} T_2(y,t) + \lim_{y\to\eta_S^-} T_1(y,t)}{2}, \text{ and} \\ T(\eta_N,t) &= \frac{\lim_{y\to\eta_N^+} T_3(y,t) + \lim_{y\to\eta_N^-} T_2(y,t)}{2}. \end{aligned}$$

When $\eta_S = \eta_N$ this condition is

$$\begin{aligned} T(\eta_S,t) &= \frac{\lim_{y\to\eta_S^+} T_3(y,t) + \lim_{y\to\eta_S^-} T_1(y,t)}{2}, \text{ and} \\ T(\eta_N,t) &= \frac{\lim_{y\to\eta_N^+} T_3(y,t) + \lim_{y\to\eta_N^-} T_1(y,t)}{2}. \end{aligned}$$

Due to the construction of the governing equations in the (η_S, η_N) plane, if the

vector field at $\eta_S = \eta_N$ is not zero, then it is parallel to the vector $(-1, 1)$. If the vector field at $\eta_S = \eta_N$ points in the same direction as $(-1, 1)$, then we let the system evolve as described by the governing equations. If instead it is parallel to $(1, -1)$, then we set $\frac{d\eta_N}{dt} = 0$ and $\frac{d\eta_N}{dt} = 0$ and let T evolve as normal. If, as T evolves, the (η_S, η_N) vector field becomes parallel to $(-1, 1)$, then the ice lines can separate and we let the system evolve as described by the governing equations.

4.1.2 Nondimensional Model

Here we nondimensionalize the model to reduce the number of parameters from ten to effectively six. In the nondimensional version of the model there are only two parameters which are unknown or not well constrained, whereas in the fully dimensional model, R, A, B, C, and T_c are not well known for planets other than Earth. A similar nondimensionalization is conducted in [36], and we have endeavored to use the same notation where the parameters are the same.

First we nondimensionalize the state variables and independent variables. The state variables η_S and η_N are already dimensionless, as is the independent variable y. Take the transformations

$$t = \theta\tau, \quad \text{and} \quad T(y,t) - T_c = K\varphi(y,\tilde{t})$$

to nondimensionalize time (τ) and temperature (φ) where $\theta = R/B$ and $K = Q/B$. The parameter θ rescales time relative to the annual heat capacity of the planet and radiative decay of annual temperature ([36] and references therein). The nondimensionalization of the temperature first zeros the temperature relative to the critical temperature of ice formation on the planet (T_c) then rescales relative to the annual insolation and radiative decay of annual temperature.

Furthermore, we define the nondimensional constants

$$\zeta = \cos\beta,$$
$$\mu = (A + BT_c)/Q,$$
$$\delta = C/B,$$
$$\lambda = \rho QR/B^2.$$

These parameters have the following physical interpretations

ζ: Cosine of obliquity. Cosine of the tilt of the planet's axis of rotation relative to the orbital plane.

μ: Radiative forcing. The numerator is the outgoing longwave radiation at the critical temperature, T_c. The numerator is the annual average solar radiation intercepted by the planet. Our parameter μ is proportional to q^{-1} in [36] and has similar sensitivities to solar radiation (Q), critical temperature (T_c), and the OLR parameters A and B.

δ: Efficiency of heat transport. The parameter δ measures the effect of transport across latitudes relative to radiative decay of annual temperature. Our parameter δ has the same physical interpretation as the nondimensional δ in [36]. [36] use a variation of a Budyko-Sellers EBM with diffusive heat transport which gives additional smoothing properties to solutions (as discussed in the description of their δ) not present in the EBM described in this study.

λ: Measure of ice line response relative to changes in temperature. The parameter λ measures how quickly the ice line latitude changes relative to changes in φ. λ has a lower bound of 0 because ρ, Q, R, and B^2 must all be positive [30] and no upper bound. In the case where $\lambda = 0$, the ice lines are stationary and φ adjusts to the location of the ice on the planet. In the limit as λ goes to infinity, the ice

Table 4.2: Parameter values used in the nondimensionalized Budyko-Widiasih model.

Parameter	Name	Value for Earth	Relation to Dimensional Constants
ζ	Cosine of obliquity	0.9171	$\zeta = \cos\beta$
μ	Radiative forcing	0.5335	$\mu = (A + BT_c)/Q$
δ	Efficiency of heat transport	1.6	$\delta = C/B$
λ	Measure of ice line response to changes in temperature	varies	$\lambda = \rho QR/B^2$
α_1	Albedo between the ice lines	.32	N/A
α_2	Albedo poleward of the ice lines	.62	N/A

lines adjust instantaneously to changes in φ.

Together these parameters yield the nondimensional Budyko-Sellers energy balance equation

$$\frac{\partial \varphi}{\partial \tau} = \sigma_6(y,\zeta)(1-\alpha(y,\eta)) - \mu - \varphi(y,\tau) - \delta(\varphi(y,\tau) - \overline{\varphi}(\tau)) \tag{4.9}$$

and the nondimensional Widiasih equations for the ice lines

$$\begin{aligned} \frac{d\eta_S}{d\tau} &= -\lambda\varphi(\eta_S,\tau), \text{ and} \\ \frac{d\eta_N}{d\tau} &= \lambda\varphi(\eta_N,\tau). \end{aligned} \tag{4.10}$$

Notice that we have not changed the albedo function. This is because the parameters α_1 and α_2 which denote the albedo of the planet between the ice lines and poleward of the ice lines, respectively, are already dimensionless.

The values of our nondimensional parameters computed from the regular Budyko parameters are given in Table 4.2.

4.2 Temperature Equilibrium Solutions

To see how the ice line equilibria change as we change parameters, we need to know what the equilibrium "temperature" profile, φ^*, is. First we must compute $\overline{\varphi}$ which we do by setting the left hand side of (4.9) equal to zero, integrating both sides from negative one to one, and dividing by two. This gives us

$$0 = \frac{1}{2}\int_{-1}^{1} \sigma_6(y,\zeta)(1-\alpha(y,\eta))dy - \mu - \overline{\varphi}. \tag{4.11}$$

because $\frac{1}{2}\int_{-1}^{1}\overline{\varphi} = \overline{\varphi}$, so there is no dependence on γ. Solving for $\overline{\varphi}$ yields

$$\begin{aligned}
\overline{\varphi} &= \frac{1}{2}\int_{-1}^{1}\sigma_6(y,\zeta)dy - \frac{1}{2}\int_{-1}^{1}\sigma_6(y,\zeta)\alpha(y,\eta)dy - \mu \\
&= 1 - \mu - \frac{\alpha_2}{2}\int_{-1}^{\eta_S}\sigma_6(y,\zeta)dy - \frac{\alpha_1}{2}\int_{\eta_S}^{\eta_N} s(y,\zeta)dy - \frac{\alpha_2}{2}\int_{\eta_N}^{1} s(y,\zeta)dy \\
&= 1 - \mu - \frac{\alpha_2}{2}\int_{-1}^{1}\sigma_6(y,\zeta)dy - \frac{(\alpha_1-\alpha_2)}{2}\int_{\eta_S}^{\eta_N} s(y,\zeta)dy \\
&= 1 - \mu - \alpha_2 + \frac{\alpha_2-\alpha_1}{2}\int_{\eta_S}^{\eta_N} s(y,\zeta)dy
\end{aligned}$$

Since s is simply a sixth degree polynomial, we can integrate it explicitly and the equilibrium "temperature" profile is

$$\varphi^*(y) = \frac{\sigma_6(y,\zeta)(1-\alpha(y,\eta)) - \mu + \delta\overline{\varphi}}{1+\gamma}. \tag{4.12}$$

If λ is large, then the ice line equilibria occur at $\varphi^*(\eta_S) = 0$ and $\varphi^*(\eta_N) = 0$ for $\eta_S, \eta_N \in (-1,1)$, i.e. when

$$\begin{aligned}
0 &= s(\eta_S,\zeta)(1-\alpha(\eta_S,\vec{\eta})) - \mu + \delta\left(1 - \mu - \alpha_2 + \frac{\alpha_2-\alpha_1}{2}\int_{\eta_S}^{\eta_N} s(y,\zeta)dy\right), \text{ and} \\
0 &= s(\eta_N,\zeta)(1-\alpha(\eta_N,\vec{\eta})) - \mu + \delta\left(1 - \mu - \alpha_2 + \frac{\alpha_2-\alpha_1}{2}\int_{\eta_S}^{\eta_N} s(y,\zeta)dy\right)
\end{aligned}$$

or rather when

$$0 = \frac{\alpha_1 + \alpha_2}{2} s(\eta_S, \zeta) - \mu + \delta \left((1 - \mu) + \frac{\alpha_0 - 1}{2} \int_{\eta_S}^{\eta_N} \sigma_6(y, \zeta) dy \right), \text{ and}$$
$$0 = \frac{\alpha_1 + \alpha_2}{2} s(\eta_N, \zeta) - \mu + \delta \left((1 - \mu) + \frac{\alpha_0 - 1}{2} \int_{\eta_S}^{\eta_N} \sigma_6(y, \zeta) dy \right).$$

We could continue along this route (as we do in Section 5.2.1) and find the equilibrium temperature profiles for Earth; however, we are also concerned with the dynamics of the ice line solutions, so we convert the system to an approximate system on a finite dimensional function space.

4.3 Non-dimensional sixth degree approximation

To discuss the dynamics of the non-dimensional Budyko equation (4.9) we follow the same technique as McGehee and Widiasih [30].

Define a function space X containing φ as a function of y which must also contain all of the equilibrium solutions (4.12). These solutions depend only on y by the function $\sigma_6(y, \zeta)$ with discontinuities at the southern and northern ice lines. Since s is an even, sixth degree polynomial, this motivates the definition of X to be the space of functions on $[-1, 1]$ which are piecewise sixth degree polynomials with two discontinuities, i.e. X is the set of all functions of the form

$$\varphi(y) = \begin{cases} \sum_{i=0}^{3} (u_{2i} + v_{2i}) p_{2i}(y) & y < \eta_S \\ \sum_{i=0}^{3} v_{2i} p_{2i}(y) & \eta_S < y < \eta_N \\ \sum_{i=0}^{3} (w_{2i} + v_{2i}) p_{2i}(y) & y > \eta_N \end{cases} \tag{4.13}$$

where $u_{2i}, v_{2i}, w_{2i} \in \mathbb{R}$ for each i and p_{2i} is the $2i$-th Legendre polynomial. At the ice

lines we have

$$\varphi(\eta_S) = \frac{\lim_{y\to\eta_S^+}\varphi(y) + \lim_{y\to\eta_S^-}\varphi(y)}{2}, \text{ and} \tag{4.14}$$

$$\varphi(\eta_N) = \frac{\lim_{y\to\eta_N^+}\varphi(y) + \lim_{y\to\eta_N^-}\varphi(y)}{2}. \tag{4.15}$$

This means that the value of φ at the ice line is the average of the values directly to the north and south of the ice line. From this construction, we see that X is a twelve dimensional function space parameterized by the u_{2i}, v_{2i}, and w_{2i} variables.

To re-write the non-dimensional Budyko equation in these new variables, we must first re-compute $\overline{\varphi}$ in the new variables. We have

$$\begin{aligned}
\overline{\varphi} =& \frac{1}{2}\int_{-1}^{1}\varphi(y)dy \\
=& \frac{1}{2}\int_{-1}^{\eta_S}\left(\sum_{i=0}^{3}(u_{2i}+v_{2i})p_{2i}(y)\right)dy + \frac{1}{2}\int_{\eta_S}^{\eta_N}\left(\sum_{i=0}^{3}v_{2i}p_{2i}(y)\right)dy \\
&+ \frac{1}{2}\int_{\eta_N}^{1}\left(\sum_{i=0}^{3}(w_{2i}+v_{2i})p_{2i}(y)\right)dy \\
=& \frac{1}{2}\left[2(v_0+w_0) + \sum_{i=0}^{3}(u_{2i}P_{2i}(\eta_S) - w_{2i}P_{2i}(\eta_N))\right]
\end{aligned}$$

where $P_{2i}(\eta) = \int_{-1}^{\eta} p_{2i}(y)dy$.

Plugging equation (4.13) into the non-dimensional Budyko equation (4.9) gives us the system of ODEs

$$\begin{aligned}
\sum_{i=0}^{3}\dot{u}_{2i}p_{2i}(y) &= \alpha_1 - \alpha_2 - (1+\delta)u_0 - \sum_{i=1}^{3}((\alpha_1-\alpha_2)s_{2i}p_{2i}(\zeta) + (1+\delta)u_{2i})p_{2i}(y) \\
\sum_{i=0}^{3}\dot{v}_{2i}p_{2i}(y) &= 1 - \alpha_1 - \mu - (1+\delta)v_0 + \delta\overline{\varphi} - \sum_{i=1}^{3}((1-\alpha_1)s_{2i}p_{2i}(\zeta) + (1+\delta)v_{2i})p_{2i}(y) \\
\sum_{i=0}^{3}\dot{w}_{2i}p_{2i}(y) &= \alpha_1 - \alpha_2 - (1+\delta)w_0 - \sum_{i=1}^{3}((\alpha_1-\alpha_2)s_{2i}p_{2i}(\zeta) + (1+\delta)w_{2i})p_{2i}(y)
\end{aligned} \tag{4.16}$$

following appropriate algebra to isolate the variables. Equating coefficients of the Legendre polynomials gives the twelve equations

$$\begin{aligned}
\dot{u}_0 &= \alpha_1 - \alpha_2 - (1+\delta)u_0 \\
\dot{v}_0 &= 1 - \alpha_1 - \mu - (1+\delta)v_0 + \delta\bar{\varphi} \\
\dot{w}_0 &= \alpha_1 - \alpha_2 - (1+\delta)w_0 \\
\dot{u}_{2i} &= -(\alpha_1 - \alpha_2)s_{2i}p_{2i}(\zeta) - (1+\delta)u_{2i} \\
\dot{v}_{2i} &= -(1-\alpha_1)s_{2i}p_{2i}(\zeta) - (1+\delta)v_{2i} \\
\dot{w}_{2i} &= -(\alpha_1 - \alpha_2)s_{2i}p_{2i}(\zeta) - (1+\delta)w_{2i}
\end{aligned} \tag{4.17}$$

for $i = 1, 2, 3$.

We see that all of the equations except the v_0 equation are decoupled ($\bar{\varphi}$ depends on u_{2i}, v_{2i}, and w_{2i} for $i = 0, 1, 2, 3$). This means that the decoupled equations converge exponentially (at rate $-(1+\delta)$) to their respective equilibria

$$u_0^* = w_0^* = \frac{\alpha_1 - \alpha_2}{1+\delta}, \quad u_{2i}^* = w_{2i}^* = -\frac{(\alpha_1 - \alpha_2)s_{2i}p_{2i}(\zeta)}{1+\delta}, \text{ and } v_{2i}^* = -\frac{(1-\alpha_1)s_{2i}p_{2i}(\zeta)}{1+\delta},$$

for $i = 1, 2, 3$. This leaves only the $\dot{v}_0$ equation

$$\begin{aligned}
\dot{v}_0 &= 1 - \alpha_1 - \mu - (1+\delta)v_0 + \delta\bar{\varphi} \\
&= 1 - \alpha_1 - \mu - (1+\delta)v_0 + \frac{\delta}{2}\left[2(v_0 + w_0) + \sum_{i=0}^{3}(u_{2i}P_{2i}(\eta_S) - w_{2i}P_{2i}(\eta_N))\right] \\
&= 1 - \alpha_1 - \mu - v_0 + \frac{\delta}{2}\left[2w_0 + \sum_{i=0}^{3}(u_{2i}P_{2i}(\eta_S) - w_{2i}P_{2i}(\eta_N))\right]
\end{aligned}$$

which tells us that the variable v_0 is a coordinate on a globally attracting invariant

one-dimensional manifold. On this manifold, v_0 is governed by the equation

$$\dot{v}_0 = 1 - \alpha_1 - \mu - v_0 + \frac{\delta(\alpha_1 - \alpha_2)}{2(1+\delta)} \left[2 + \eta_S - \eta_N - \sum_{i=1}^{3} (P_{2i}(\eta_S) - P_{2i}(\eta_N)) s_{2i} p_{2i}(\zeta) \right].$$

Define

$$F(x_1, x_2) = 1 - \alpha_1 - \mu + \frac{\delta(\alpha_1 - \alpha_2)}{2(1+\delta)} \left[2 + x_1 - x_2 - \sum_{i=1}^{3} (P_{2i}(x_1) - P_{2i}(x_2)) s_{2i} p_{2i}(\zeta) \right] \tag{4.18}$$

then we can write

$$\dot{v}_0 = -(v_0 - F(\eta_S, \eta_N)). \tag{4.19}$$

Now consider what is happening at the ice lines. Recall that the value of φ at the ice lines is the average of the left and right hand limits. For $\eta_S < \eta_N$ we have

$$\varphi(\eta_S) = \frac{\sum_{i=0}^{3} (u_{2i} + 2v_{2i}) p_{2i}(\eta_S)}{2}, \text{ and}$$
$$\varphi(\eta_N) = \frac{\sum_{i=0}^{3} (w_{2i} + 2v_{2i}) p_{2i}(\eta_N)}{2}.$$

Assuming that the u_{2i}'s and the w_{2i}'s have decayed to their equilibria, we have

$$\varphi(\eta_S) = v_0 + \frac{(\alpha_1 - \alpha_2) + (\alpha_1 + \alpha_2 - 2) \sum_{i=1}^{3} s_{2i} p_{2i}(\zeta) p_{2i}(\eta_S)}{2(1+\gamma)}, \text{ and}$$
$$\varphi(\eta_N) = v_0 + \frac{(\alpha_1 - \alpha_2) + (\alpha_1 + \alpha_2 - 2) \sum_{i=1}^{3} s_{2i} p_{2i}(\zeta) p_{2i}(\eta_N)}{2(1+\gamma)}.$$

since $u_{2i}^* = w_{2i}^*$. However, if the ice lines have come together and $\eta_S = \eta_N$, then the left

and right hand limits come from the first and third components of φ, namely

$$\varphi(\eta_S) = \frac{\sum_{i=0}^{3}(u_{2i} + 2v_{2i} + w_{2i})p_{2i}(\eta_S)}{2}, \text{ and}$$
$$\varphi(\eta_N) = \frac{\sum_{i=0}^{3}(w_{2i} + 2v_{2i} + w_{2i})p_{2i}(\eta_N)}{2}.$$

Again, assuming that the u_{2i}'s and the w_{2i}'s have decayed to their equilibria and recalling that $u^*_{2i} = w^*_{2i}$ for $i = 0, 1, 2, 3$ gives

$$\varphi(\eta_S) = v_0 + \frac{(\alpha_1 - \alpha_2) + (\alpha_2 - 1)\sum_{i=1}^{3} s_{2i}p_{2i}(\zeta)p_{2i}(\eta_S)}{1+\delta}, \text{ and}$$
$$\varphi(\eta_N) = v_0 + \frac{(\alpha_1 - \alpha_2) + (\alpha_2 - 1)\sum_{i=1}^{3} s_{2i}p_{2i}(\zeta)p_{2i}(\eta_N)}{1+\delta}.$$

Define

$$G(y) = \begin{cases} -\frac{(\alpha_1-\alpha_2)+(\alpha_1+\alpha_2-2)\sum_{i=1}^{3} s_{2i}p_{2i}(\zeta)p_{2i}(y)}{2(1+\delta)} & \eta_S < \eta_N \\ -\frac{(\alpha_1-\alpha_2)+(\alpha_2-1)\sum_{i=1}^{3} s_{2i}p_{2i}(\zeta)p_{2i}(y)}{1+\delta} & \eta_S = \eta_N \end{cases}. \tag{4.20}$$

Then the ice line equations for ice caps are

$$\begin{aligned} \frac{d\eta_S}{dt} &= -\lambda(v_0 - G(\eta_S)) \\ \frac{d\eta_N}{dt} &= \lambda(v_0 - G(\eta_N)) \end{aligned} \tag{4.21}$$

and ice line equilibria occur when

$$v_0 = G(\eta_S), \quad \text{and} \quad v_0 = G(\eta_N).$$

The sixth degree polynomial approximation to the Budyko-Widiasih model can be

described by the three equations:

$$\begin{aligned} \dot{v}_0 &= -(v_0 - F(\eta_S, \eta_N)) \\ \dot{\eta}_S &= -\lambda(v_0 - G(\eta_S)) \\ \dot{\eta}_N &= \lambda(v_0 - G(\eta_N)). \end{aligned} \tag{4.22}$$

Equilibria of this system are given by

$$v_0 - F(\eta_S, \eta_N) = G(\eta_S) - v_0 = v_0 - G(\eta_N) = 0 \tag{4.23}$$

for (η_S, η_N) pairs satisfying $-1 < \eta_S < \eta_N < 1$. If either ice line is at a pole or the ice lines come together, we may have Filippov equilibria.

4.4 Invariant Solutions

Below we discuss some invariant solutions of the system. Some results are given specifically for Earth while others are left as general results which apply to planets with any obliquity.

4.4.1 Invariance of Symmetric Ice Lines

Regardless of the choice of parameter values, symmetric ice caps or ice belts are invariant in the system. In particular, if the planet is initially in a symmetric configuration, then it must stay in a symmetric configuration.

Lemma 4.4.1. *The plane given by $\eta_S = -\eta_N$ is invariant for any combination of parameter values for system* (4.22).

Proof. Suppose $\eta_S = -\eta_N$. Then the governing equations are

$$\begin{aligned} \dot{v}_0 &= -(v_0 - F(-\eta_N, \eta_N)) \\ \dot{\eta}_S &= \mp\lambda(v_0 - G(\eta_N)) \\ \dot{\eta}_N &= \pm\lambda(v_0 - G(\eta_N)). \end{aligned} \tag{4.24}$$

because G is an even function. Then $\dot{\eta}_S = -\dot{\eta}_N$, so movement in the $\eta_S = -\eta_N$ plane is tangent to the $\eta_S = -\eta_N$ plane. □

In Section 6, we will see that the symmetric ice line configurations are globally attracting on Earth.

4.4.2 Equilibria of the System

As stated in Section 4, the equilibria of the system are given by

$$v_0 - F(\eta_S, \eta_N) = G(\eta_S) - v_0 = v_0 - G(\eta_N) = 0 \tag{4.25}$$

or rather when the surfaces $F(\eta_S, \eta_N)$, $G(\eta_S)$, and $G(\eta_N)$ have a common intersection point. In this case, we can numerically compute the equilibria using the parameter values from Table 4.2. They are

$$(v_0, \eta_S, \eta_N) \approx (0.0204, -0.26, 0.26), \quad \text{and} \quad (v_0, \eta_S, \eta_N) \approx (0.1398, -0.93, 0.93) \tag{4.26}$$

as well as the Filippov equilibria along the line $\eta_S = \eta_N$ where $F(\eta_S, \eta_N) \approx -0.0381$. Then on Earth, we have two symmetric equilibria corresponding to small ice caps and large ice caps and Filippov equilibria indicating a completely ice covered Earth.

The equilibrium at $(v_0, \eta_S, \eta_N) \approx (0.1398, -0.93, 0.93)$ is stable with all eigenvalues of the Jacobian at that point negative. The equilibrium at $(v_0, \eta_S, \eta_N) \approx (0.0204, -0.26, 0.26)$ is a saddle with two negative eigenvalues and one positive eigenvalue of the Jacobian at that point. We have computed the eigenvalues numerically

for λ between 0.01 and 15 and we conjecture that the results hold for all positive λ. Furthermore, the Filippov equilibria along $\eta_S = \eta_N$ are stable, and, in particular, there is no sliding along $\eta_S = \eta_N$. These results agree with earlier studies where the ice lines are constrained to be symmetric [30, 47].

If we assume λ is small then the system quickly collapses to the manifold $v_0 = F(\eta_S, \eta_N)$ and the movement of the ice lines is governed by the equations

$$\begin{aligned} \frac{d\eta_S}{d\tau} &= -\lambda(F(\eta_S, \eta_N) - G(\eta_S)), \text{ and} \\ \frac{d\eta_S}{d\tau} &= \lambda(F(\eta_S, \eta_N) - G(\eta_N)) \end{aligned} \tag{4.27}$$

and the ice line equilibria are given by

$$\begin{aligned} F(\eta_S, \eta_N) - G(\eta_S) &= 0, \text{ and} \\ F(\eta_S, \eta_N) - G(\eta_N) &= 0. \end{aligned} \tag{4.28}$$

Notice that this is an equivalent condition to the equilibria for the full three dimensional system. We are not surprised to find that for Earth parameters as given in Table 4.2, there are two ice line equilibria of (4.27):

$$(\eta_S, \eta_N) \approx (-0.26, 0.26), \quad \text{and} \quad (\eta_S, \eta_N) \approx (-0.93, 0.93)$$

which agree with previous studies using only one ice line on a symmetric planet [29, 47].

4.4.3 Phase Diagrams

In the three dimensional system, $F(\eta_S, \eta_N)$, $G(\eta_S)$ and $G(\eta_N)$ are the nullclines. For small λ, trajectories first converge to the surface $F(\eta_S, \eta_N)$ then flow along this critical manifold. For large λ, trajectories converge to the curve defined by $G(\eta_S) = G(\eta_N)$. This is depicted in Figure 4.2

Because the three dimensional vector field is tricky to visualize, let's consider the

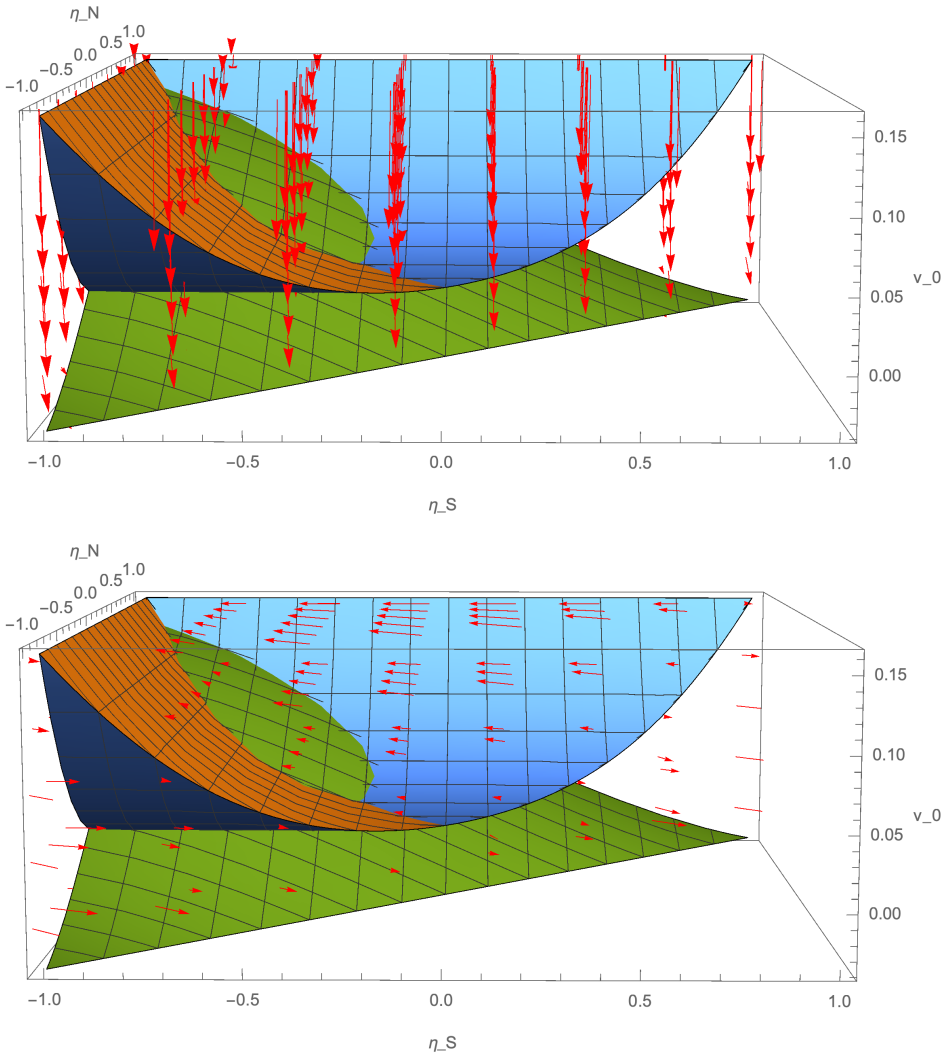

Figure 4.2: The three dimensional vector field for the system (4.22) for $\lambda = 0.1$ (top) and $\lambda = 100$ (bottom). The green surface is $F(\eta_S, \eta_N)$ and the orange and blue surfaces are $G(\eta_S)$ and $G(\eta_N)$, respectively. All other parameter values are as given in Table 4.2.

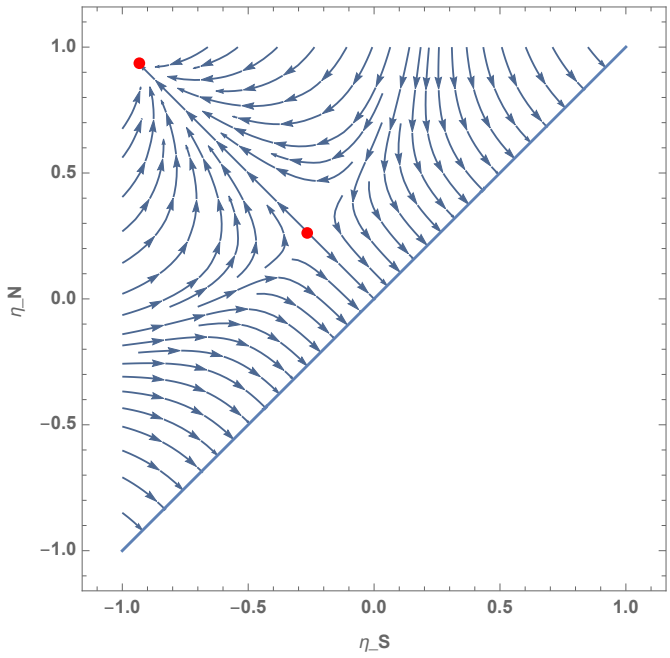

Figure 4.3: Ice line vector field parameter values from Table 4.2. Red dots indicated equilibria of (4.27). Solutions with $\eta_S > \eta_N$ are not physical and are not plotted.

case where λ is small so that we can consider the phase diagram in the plane. If λ is small, then the ice caps respond slowly to changes in temperature. The vector field for slowly moving ice caps with current values for Earth parameters is given in Figure 4.3. The line $\eta_S = \eta_N$ indicates the boundary where the ice lines come together. We see that the vector field approaches this boundary perpendicularly. The stability results of earlier studies are replicated here, namely the scenarios of a small ice cap and snowball Earth are stable, and ice free Earth and a large ice cap are unstable (in this case, the large ice cap is a saddle).

Figure 4.4 depicts representative vector fields for (4.27) and Earth parameters for some values of the greenhouse gas parameter A. The current value of A is normally taken to be approximately 202 [47, 41, 8]. Recall that as A decreases from 202 there is a stronger greenhouse gas effect. A full bifurcation diagram for A is given in 4.5.

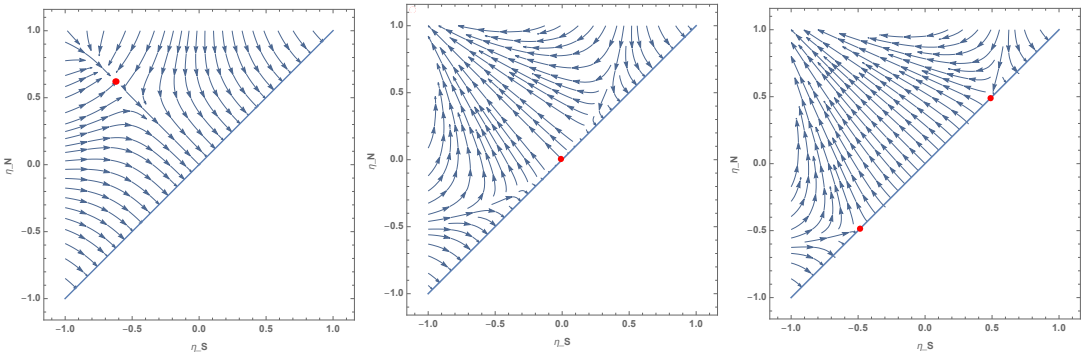

Figure 4.4: Ice line vector field for different values of the greenhouse gas parameter A and all other parameters from Table 4.2 held at Earth values. Red dots indicated equilibria of (4.27). Vectors below the line $\eta_S = \eta_N$ have been extended to better depict the value of the vector field on this line. Solutions with $\eta_S > \eta_N$ are not physical and not plotted. Left: $A = 213$, Middle: $A = 185$, Right: $A = 175$. The value of A used to model Earth in the current epoch is 202 and the corresponding vector field is depicted in Figure 4.3.

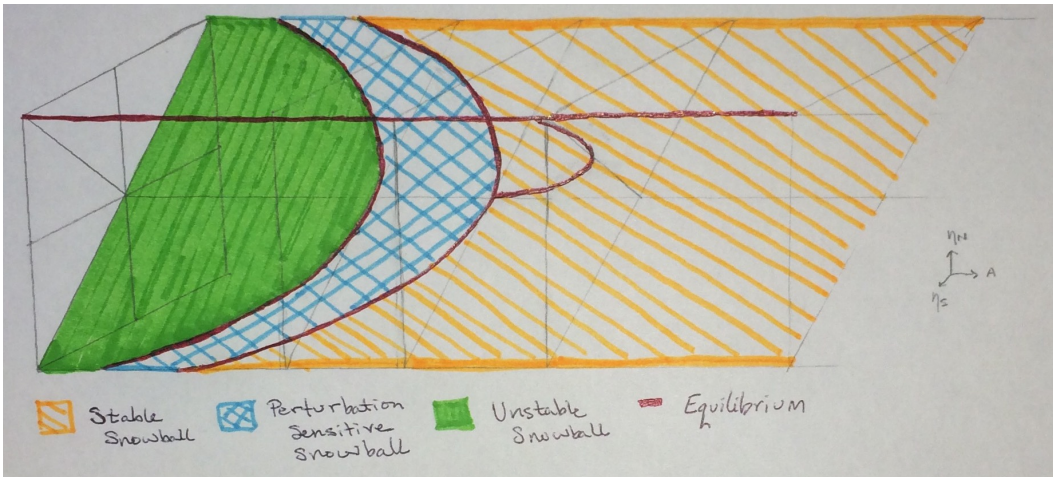

Figure 4.5: Bifurcation diagram of greenhouse gas parameter A. All other parameters from Table 4.2 held at Earth values.

The leftmost image of 4.4 is for $A = 212.94$, indicating a slightly weaker greenhouse gas effect than what is normally used in this model. In this case, the equilibria representing the small, stable ice cap, and the large saddle ice cap have coalesced. This agrees with past analysis of the effect of A on the location of ice line equilibria [47, 2]. Solutions with $\eta_S > \eta_N$ are not physical and are not shown. For larger values of A, the system goes through a saddle node bifurcation resulting in no equilibria in the region of physical solutions. In this case, all solutions tend toward the line $\eta_S = \eta_N$.

The middle image of 4.4 is for $A = 185$, indicating a stronger greenhouse gas effect than we currently experience on Earth. In this case, the equilibrium associated with the stable small ice cap has moved past the ice free Earth, leaving a Fillippov equilibrium at (-1,1). The saddle equilibrium for the large ice cap has collided with the $\eta_S = \eta_N$ boundary. For smaller values of A, this saddle equilibrium bifurcates into two saddle equilibria that move toward (-1,-1) and (1,1) as A continues to decrease. This is depicted in the righthand image of 4.4.

Because of the piecewise definition of G, the vector field along the boundary is different than the vector field on the interior of the triangular region. For example, for $A = 175$, between the equilibria the vector field points in opposite directions. For points above the line, the vector field points toward the interior of the physical region (up and to the left) whereas on the line $\eta_S = \eta_N$, the vector field points away (down and to the right). This tells us that if at some point t the ice lines came together, the Snowball state would be stable and there would be no escape. However, if we made a perturbation in the ice cover in the correct place on the Earth (i.e. between the equilibria), then all of the ice on the planet would melt. We note that this phenomenon is different from previous work in this area [47, 2] and requires further study. That study is left for future work.

A schematic of the bifurcation diagram of A is given in Figure 4.5. The red curves indicate equilibria of the system (stability is not indicated here). The orange region indicates a stable Snowball Earth, meaning that the the vector field along the boundary

$\eta_S = \eta_N$ and the vector field just above the boundary both point in the same direction (down and to the right). The blue region indicates a perturbation sensitive Snowball Earth as described in the previous paragraph. The green region indicates a completely unstable Snowball Earth meaning that the the vector field along the boundary $\eta_S = \eta_N$ and the vector field just above the boundary both point up and to the left. Snowball Earth isn't fully unstable until about $A = 122$.

4.5 Stability of Symmetric Solutions

It is easiest to see the stability of the symmetric solutions if we change coordinates. Let $x = (\eta_N + \eta_S)/2$ and $y = (\eta_N - \eta_S)/2$ (see Figure 4.6 for a visual reference). Then x measures the distance away from the symmetric state and y measures the distance away from the state where the ice lines are together. Then $\eta_N = x + y$ and $\eta_S = x - y$. The domain is $P = \{(x, y) \in [-, 1, 1] \times [0, 1] : \ |x| + |y| \leq 1\}$.

Redefine the functions F and G in these new coordinates as

$$\tilde{F}(x, y) = F(x - y, x + y), \quad \tilde{G}_S(x, y) = G(x - y), \quad \text{and} \quad \tilde{G}_N(x, y) = G(x + y). \tag{4.29}$$

Then the equivalent system in these coordinates is

$$\begin{aligned} \dot{v}_0 &= -(v_0 - \tilde{F}(x, y)) \\ \dot{x} &= -\frac{\lambda}{2}(\tilde{G}_N(x, y) - \tilde{G}_S(x, y)) \\ \dot{y} &= \frac{\lambda}{2}(2v_0 - \tilde{G}_N(x, y) - \tilde{G}_S(x, y)) \end{aligned} \tag{4.30}$$

For the following arguments we take a small λ so that the temperature variable v_0 quickly decays to its equilibrium $\tilde{F}(x, y)$ and we consider the ice line system in the plane

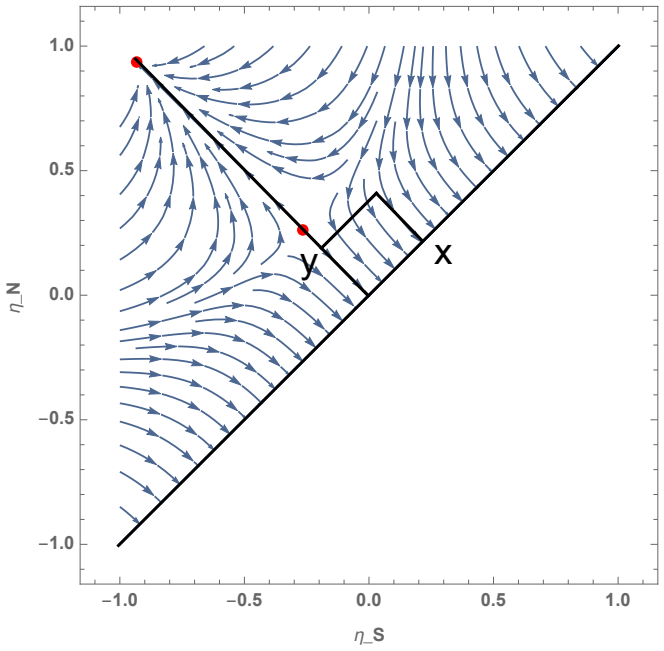

Figure 4.6: The $x - y$ coordinates in terms of the original ice line coordinates η_S and η_N. The domain is $P = \{(x, y) \in [-, 1, 1] \times [0, 1] : \ |x| + |y| \leq 1\}$.

$$\begin{aligned}\dot{x} &= -\frac{\lambda}{2}(\tilde{G}_N(x,y) - \tilde{G}_S(x,y)) \\ \dot{y} &= \frac{\lambda}{2}(2\tilde{F}(x,y) - \tilde{G}_N(x,y) - \tilde{G}_S(x,y)).\end{aligned} \tag{4.31}$$

It remains to be shown if the symmetry results hold for the full three dimensional system.

Lemma 4.5.1. *Suppose $x, y \in P$ and $\zeta = \zeta_{Earth}$. Then the zeros of $\tilde{G}_N(x,y) - \tilde{G}_S(x,y)$ are identically the set $S = \{(x,y) \in P : \ x = 0 \text{ or } y = 0\}$. Furthermore $\tilde{G}_N(x,y) - \tilde{G}_S(x,y) > 0$ for $x > 0$ and $\tilde{G}_N(x,y) - \tilde{G}_S(x,y) < 0$ for $x < 0$.*

Proof. We have

$$\tilde{G}_N(x,y) - \tilde{G}_S(x,y) = \begin{cases} -\frac{(\alpha_1+\alpha_2-2)\sum_{i=1}^{3} s_{2i}p_{2i}(\zeta)(p_{2i}(x+y)-p_{2i}(x-y))}{2(1+\delta)} & y \neq 0 \\ -\frac{(\alpha_2-1)\sum_{i=1}^{3} s_{2i}p_{2i}(\zeta)(p_{2i}(x+y)-p_{2i}(x-y))}{1+\delta} & y = 0 \end{cases}. \tag{4.32}$$

It is straightforward algebra to show that

$$p_2(x+y) - p_2(x-y) = 6xy \tag{4.33}$$

$$p_4(x+y) - p_4(x-y) = 5xy(-3 + 7(x^2+y^2)) \tag{4.34}$$

$$p_6(x+y) - p_6(x-y) = \frac{21}{4}xy(5 - 30(x^2+y^2) + 110x^2y^2 + 33(x^4+y^4)) \tag{4.35}$$

so that when $y \neq 0$ the subtraction $\tilde{G}_N(x,y) - \tilde{G}_S(x,y)$ is given by

$$-\frac{(\alpha_1+\alpha_2-2)}{2(1+\delta)}xy[(6s_2p_2(\zeta) + 5(-3+7(x^2+y^2))s_4p_4(\zeta) \tag{4.36}$$

$$+ \frac{21}{4}(5 - 30(x^2+y^2) + 110x^2y^2 + 33(x^4+y^4))s_6p_6(\zeta)] \tag{4.37}$$

and when $y = 0$ the subtraction is simply zero.

Then we clearly have $\tilde{G}_N(x,y) - \tilde{G}_S(x,y) = 0$ if $x = 0$ or $y = 0$, so we must show that the term in the numerator multiplied by $(\alpha_1 + \alpha_2 - 2)xy$ has no zeros in P, namely

$$\begin{aligned} &6s_2p_2(\zeta)+5(-3+7(x^2+y^2))s_4p_4(\zeta) \\ &\qquad + \frac{21}{4}(5-30(x^2+y^2)+110x^2y^2+33(x^4+y^4))s_6p_6(\zeta) \end{aligned} \tag{4.38}$$

has no zeros in P.

We can re-write the above term as

$$\begin{aligned} &y^4\left(\frac{693}{4}s_6p_6(\zeta)\right)+y^2\left(35s_4p_4(\zeta)+\frac{21}{4}(-30+110x^2)s_6p_6(\zeta)\right) \\ &\quad+\left(6s_2p_2(\zeta)-15s_2p_4(\zeta)+\frac{205}{4}s_6p_6(\zeta)\right. \\ &\qquad\left.+(35s_4p_4(\zeta)-\frac{630}{4}s_6p_6(\zeta))x^2+\frac{693}{4}s_6p_6(\zeta)x^4\right). \end{aligned} \tag{4.39}$$

Let

$$a_0(x,\zeta) = 6s_2p_2(\zeta)-15s_4p_4(\zeta)+\frac{105}{4}s_6p_6(\zeta)+\left(35s_4p_4(\zeta)-\frac{630}{4}s_6p_6(\zeta)\right)x^2 \tag{4.40}$$

$$+\frac{693}{4}s_6p_6(\zeta)x^4 \tag{4.41}$$

$$a_2(x,\zeta) = 35s_4p_4(\zeta)+\frac{21}{4}(-30+110x^2)s_6p_6(\zeta), \text{ and} \tag{4.42}$$

$$a_4(\zeta) = \frac{693}{4}s_6p_6(\zeta) \tag{4.43}$$

If we had

$$0 = y^4a_4(\zeta)+y^2a_2(x,\zeta)+a_0(x,\zeta) \tag{4.44}$$

then the binomial theorem tells us that

$$y^2 = \frac{a_2(x,\zeta)\pm\sqrt{(a_2(x,\zeta))^2-4a_4(\zeta)a_0(x,\zeta)}}{2a_4(\zeta)}. \tag{4.45}$$

For $\zeta = \zeta_{Earth}$ we have two real and two imaginary solutions. The real solutions yield y^2 values strictly greater than 1 for all $x \in [-1,1]$, so there are no zeros in P

except when $x = 0$ or $y = 0$.

We must also show that $\tilde{G}_N(x,y) - \tilde{G}_S(x,y) > 0$ for $x > 0$ and $\tilde{G}_N(x,y) - \tilde{G}_S(x,y) < 0$ for $x < 0$. Notice that $\tilde{G}_N(-x,y) - \tilde{G}_S(-x,y) = -(\tilde{G}_N(x,y) - \tilde{G}_S(x,y))$, so $\tilde{G}_N(x,y) - \tilde{G}_S(x,y)$ is antisymmetric about $x = 0$ and we need only show that $\tilde{G}_N(x,y) - \tilde{G}_S(x,y) > 0$ for $x > 0$.

Let $P^+ = P \cap \{x > 0\}$. We have that

$$\tilde{G}_N(x,y) - \tilde{G}_S(x,y) = -\frac{\alpha_1 + \alpha_2 - 2}{2(1+\delta)} xy(y^4 a_4(\zeta) + y^2 a_2(x,\zeta) + a_0(x,\zeta)) \tag{4.46}$$

as well as

$$-\frac{\alpha_1 + \alpha_2 - 2}{2(1+\delta)} xy > 0, \quad \text{and} \quad y^4 a_4(\zeta_{Earth}) + y^2 a_2(x,\zeta_{Earth}) + a_0(x,\zeta_{Earth}) > 0 \tag{4.47}$$

when $(x,y) \in P^+$, as desired. □

Corollary 4.5.1. *Let $\zeta = \zeta_{Earth}$. Then the only equilibria of the system lie in S.*

Before we get to the main result, we must define what it means to be a symmetric solution. We define the set of symmetric ice line configurations to be the set

$$\{(x,y) \in P : \ x = 0 \text{ or } y = 0\}. \tag{4.48}$$

We see that the set S from the previous lemma is the set of symmetric ice line configurations. Notice that when $x = 0$, then $\eta_N = -\eta_S$ which is what we intuitively understand to be symmetric. We include the case where $y = 0$ because this is the case where the ice lines have come together so the planet is completely covered in ice. Let $S_x = \{(x,y) \in S : x = 0\}$ and let $S_y = \{(x,y) \in S : y = 0\}$.

The the main result of this section uses a result from La Salle (Theorem 1 in [27]), namely

Theorem 4.5.1 (La Salle)**.** *Let $R \subseteq \mathbb{R}^n$ be a compact positively invariant set. Assume there exists a differentiable function $V : R \to \mathbb{R}$ such that*

$$\dot{V}(\mathbf{x}) \leq 0$$

for all $\mathbf{x} \in R$. Let M be the largest invariant set contained in $\{x \in R : \dot{V}(\mathbf{x}) = 0\}$. Then all trajectories starting in R approach M as $t \to \infty$.

Finally, let $D_y \subset S_y$ be the set where the y component of the vector field is nonpositive, i.e.

$$D_y = \{(x, y) \in S_y : \dot{y} \leq 0\}. \tag{4.49}$$

Notice that D_y is heavily dependent on the choice of Budyko parameters and can be the empty set, the whole line $[-1, 1]$ or a subset thereof.

Theorem 4.5.2. *Let $\zeta = \zeta_{Earth}$, then $D_y \cup S_x$ is globally attracting.*

Proof. The domain P is positively invariant because we do not let trajectories leave the region. It is also compact.

Define $V : P \to \mathbb{R}$ as $V(x, y) = x^2$. Notice that for ice caps

$$\dot{V}(x, y) = 2x\dot{x} = -\lambda x(\tilde{G}_N(x, y) - \tilde{G}_S(x, y)) \leq 0 \tag{4.50}$$

for all $(x, y) \in KP$ since $\tilde{G}_N(x, y) - \tilde{G}_S(x, y)$ has the same sign as x. Note we have equality only when $x = 0$ or $y = 0$, i.e. on the set S.

If the vector field along $y = 0$ points towards the interior of P, then S_x is the largest invariant set contained in the set $\{(x, y) \in P : \dot{V}(x, y) = 0\}$. If there is a region $D_y \subseteq S_y$ along which the vector field points down, then D_y is also invariant and $D_y \cup S_x$ is the largest invariant set contained in the set $\{(x, y) \in P : \dot{V}(x, y) = 0\}$.

La Salle's theorem tells us that all trajectories starting in P approach $D_y \cup S_x$ (where

D_y may be the empty set) as $t \to \infty$.

Since P is the whole space, we have that $D_y \cup S_x \subseteq S$ is globally attracting. □

4.6 Discussion

In this chapter we've laid the framework for studying asymmetric behavior of ice caps or an ice belt. To do this, we've created an additional ice line equation following techniques outlined in earlier studies of Budyko energy balance models with dynamic ice lines, namely [2, 29, 30, 47].

In particular, we have considered the case of Earth and have shown that symmetric ice line configurations are globally attracting for Earth regardless of the choice of Budyko parameters. In fact, the global stability relies only on the obliquity parameter ζ.

It would be interesting to consider making the parameter A a dynamic variable as was done recently in the symmetric case [2]. This may help us better understand glacial cycles which may have had asynchronous evolution between the northern and southern hemispheres. Recent data from New Zealand show that glaciers in the southern hemisphere retreated more slowly that their counterparts in the northern hemisphere [37], suggesting that north-south symmetry was broken during Earth's past climate.

Chapter 5

Energy Balance Model of Pluto with Two Ice Lines

The Budyko energy balance model (EBM) has recently been adapted to study climates on other planets [8, 36]. In this chapter we use the asymmetric EBM developed in Chapter 4 to study asymmetric ice belts in an energy balance model of Pluto. The majority of this chapter has been submitted to *Icarus* and is under revision at that journal.

NASA's New Horizons mission provided us with a wealth of information on Pluto and other objects in the Kuiper belt. The mission gave us a snapshot of Pluto's unexpectedly interesting geological formations, albedo contrasts, and surface and atmospheric compositions (e.g. [39, 35, 49]) among other intriguing discoveries. Pluto's *Sputnik Planitia*, within the larger Tombaugh Regio, has been an object of particular interest due to its high reflectivity, N_2 abundance, and crater-free surface (e.g. in [35, 42, 49]). In contrast with Earth's ice caps, there is no apparent "twin" of *Sputnik Planitia* or the larger Tombaugh Regio in Pluto's southern hemisphere, motivating an investigation into asymmetric behavior in low-dimensional models of the planet.

Recent modeling studies have been conducted to study different features of *Sputnik*

Planitia. These studies investigate the interplay of albedo and temperature on Pluto's surface (e.g. [15, 16]), ask whether Pluto's intriguing surface has been a feature in the past and if so, how it formed (e.g. [23, 16, 26]), and examine flow properties of N_2 glaciers in relation to New Horizons observations (e.g. [42]).

Because of Pluto's high obliquity, we consider an ice belt scenario in our coupled EBM-dynamic ice line system, where the albedo of the surface between the ice lines is higher than the surface poleward of the ice lines. In particular, we allow for two ice lines between the south and north poles which admits the possibility of asymmetric configurations of an ice belt. We show that it is possible for these ice belts to be both asymptotically stable and have the north and south ice lines which are not symmetric about the equator. Furthermore, these asymmetric solutions are present for a range of parameter values which may be relevant to Pluto and are located in approximately the same latitudinal range as Pluto's *Sputnik Planitia*.

In the following section we describe the governing equations and the parameter values that were used in this study. In section 3, we find the ice line equilibrium solutions and find the regions in parameter space for which stable, asymmetric equilibria persist. Section 4 consists of a discussion of the results. We conclude in section 5.

5.1 Adaptations to the Model

We use the same energy balance model as in Chapter 4 with a few modifications. We describe these modifications below.

Pluto is a rapidly rotating planet with more than fourteen thousand days in a Pluto year. This means we can use the approximation $\sigma_6(y, \zeta)$ for our model. The obliquity of Pluto is about 120 degrees, so the insolation distribution has a characteristic 'W' shape, where the poles get more annual insolation than the equatorial regions. This motivates us to model Pluto with an ice belt instead of an ice cap.

For the surface albedo, we again take $\eta = (\eta_S, \eta_N)$, which gives the location of a

southern (η_S) and northern (η_N) ice line. We restrict the ice lines to the interval $[-1, 1]$ with the condition $-1 \leq \eta_S \leq \eta_N \leq 1$ (i.e. we do not let the ice lines cross each other). We consider a piecewise constant albedo function given by

$$\alpha(y, \eta) = \begin{cases} \alpha_2, & y < \eta_S \\ (\alpha_1 + \alpha_2)/2, & y = \eta_S \\ \alpha_1, & \eta_S < y < \eta_N \\ (\alpha_1 + \alpha_2)/2, & y = \eta_N \\ \alpha_2, & \eta_N < y \leq 1 \end{cases} . \tag{5.1}$$

where $\alpha_2 < \alpha_1$, indicating that the region between the ice lines is more reflective than the regions poleward of the ice lines.

In addition to equation (4.1) we consider two dynamic ice line equations in the fashion of Widiasih's single ice line equation [47]. In particular, the movement of an ice line is determined by the temperature at the ice line relative to a critical temperature T_c, the highest temperature at which ice is present year round. In the case of an ice belt, we have

$$\begin{aligned} \frac{d\eta_S}{dt} &= \rho(T(\eta_S, t) - T_c), \\ \frac{d\eta_N}{dt} &= \rho(T_c - T(\eta_N, t)). \end{aligned} \tag{5.2}$$

If the southern edge of the ice belt is melting, it moves in the direction of the north pole. If instead we have $T(\eta_S, t) < T_c$ then it is colder than the critical temperature at η_S which means more ice can form and that the ice line moves toward the south pole. The northern ice line moves in a similar manner. To realize this movement with our equations, the northern ice line governing equation is multiplied by -1 so that ice formation ($T(\eta_N, t) < T_c$) or degradation ($T(\eta_N, t) > T_c$) results in the ice line moving in the proper direction.

We also must change the parameter values. Below we discuss how we arrived at the

values used in this study. Even though we are using the nondimensionalized equations, we discuss the normal Budyko parameters below because they are easier to interpret from a physical perspective.

5.1.1 Calculation and Estimation of Parameter Values

In this section we briefly discuss the parameter values typically used when studying Earth with Budyko-Sellers type energy balance models and the Widiasih dynamic ice lines. We will also describe parameter ranges which we will be using for our study of Pluto. In section 3.3 we discuss the ranges of parameters where the model results of stable, asymmetric solutions persist. The values for the dimensionless constants used in this study for the system

$$\begin{aligned} \dot{v}_0 &= -(v_0 - F(\eta_S, \eta_N)) \\ \dot{\eta}_S &= \lambda(v0 - G(\eta_S)) \\ \dot{\eta}_N &= -\lambda(vo - G(\eta_N)) \end{aligned} \tag{5.3}$$

are given in Table 5.1. Some of these parameters are well constrained by data from New Horizons while others are more uncertain.

Cosine of Obliquity. The only parameter needed to compute the cosine of the obliquity is the obliquity of the planet itself. The obliquities of Earth and Pluto have been studied extensively. Earth's current obliquity is about 23.5° and oscillates between about 22° and 24.5° [28, 30]. The obliquity of Pluto in the current epoch is about 119.6° although it oscillates between 102° and 126° over a period of about 3 million years [10]. Recent studies have considered how Pluto's changing obliquity may affect albedo and surface temperature [15, 16], but we do not consider its effects in this study. For Earth we have $\zeta_E = \cos(23.5) = 0.9171$ and for Pluto we have $\zeta_P = -0.4939$.

Radiative Forcing and Efficiency of Heat Transport. To compute the radiative forcing an efficiency of heat transport we need the parameters Q, T_c A, B, and

C. The parameters Q and T_c are straightforward to compute from the literature. The parameters A, B and C are empirical parameters and are thus hardest to determine for planets other than Earth.

The value of Q, the annual average insolation, can be calculated from first principles (see [41] and [29] among others). This value is calculated by first determining the solar intensity at the planet's average radius from the sun then scaling by 1/4 to account for the fact that the planet intercepts the energy across a disc but the energy is distributed across whole the surface area of the planet. For Earth, $Q_E = 343$ Wm^{-2} [41] and for Pluto the annual average insolation is approximately $Q_P = 0.2202$ Wm^{-2}.

The critical temperature, T_c, in these types of models is determined by the highest annual average temperature at which ice may be present year round. In models of Earth this value is traditionally taken to be -10 °C [6, 32, 41] although some recent studies have explored changing this [48]. For this model of Pluto, we will assume that all of the ice is N_2 ice, although this is a simplification of the ices on Pluto. We can then rely on work by [18] and [19], where the condensation temperature of N_2 is given as a function of the partial pressure. Since Pluto's atmospheric pressure is about 1.2 Pa [24, 21] and Pluto's lower atmosphere is greater than 99% N_2 by volume [50, 21], the partial pressure equation in [18] for the condensation temperature tells us that N_2 is condensating on Pluto when the temperature is about 36.9 K or -236.25 °C. However, we must take a lower temperature for T_c (which represents an annual average) so that the temperature would be less than or equal to 36.9 K for the whole year. We take $T_c = 35$ K $= -238.15$ °C for the critical temperature on Pluto.

As discussed in section Chapter 4, the OLR constants for Earth are gotten from satellite data with $A_E = 202$ Wm^{-1} and $B_E = 1.9$ Wm^{-1} °C^{-1} (e.g. in [47]). It is not clear what values A_P and B_P should take. For models of Earth A is referred to as the greenhouse gas parameter where, counterintuitively, a large A corresponds to a smaller greenhouse gas effect. We take $A_P = 238.2795$ Wm^{-1} and $B_P = 1$ Wm^{-1} °C^{-1} . We return to these parameters in section 3.4 to discuss possible ranges for them.

For Earth, the heat transport parameter C is taken to be roughly 3 $\mathrm{Wm}^{-1}\,{}^{\circ}\mathrm{C}^{-1}$ in recent studies [47, 30, 8]. Here we will use $C_E = 3.04$. Whereas on Earth the oceans and atmosphere do much of the heavy lifting in transporting heat across latitudes, Pluto does not have the same possible mechanisms for transporting heat. For this reason we assume C_P should be small. The validity of this assumption is is confirmed by the study of general circulation models applied to Pluto in [4] and [18] among others and we take $C_P = 0.01$.

The parameter values above results in $\mu_E = 0.5335$, $\delta_E = 1.6$, $\mu_P = 0.588$ and $\delta_P = 0.01$. Because the parameters A, B and C are all empirical parameters in the Budyko-Sellers type model, the values of μ and δ used in this study serve only to indicate *possible* behaviors on Pluto as detailed by the model. Where possible, we determine how solutions change as μ and δ are varied (see section 3.3). Further scientific work is needed to determine if the values indicated by μ and δ yield plausible values for A, B, and C for Pluto.

Ice Line Response to Temperature Change. To calculate the parameter for ice line response to the temperature change, we need R and ρ in addition to Q and B. As with our calculation of μ and δ, the dependence of λ on B makes the parameter hard to calculate exactly. Below we discuss R and ρ as they appear in other similar studies and how we use them to estimate λ.

The parameter R, the heat capacity of the surface layer, has units of Watts per square meter per degree Celsius per year ($\mathrm{Wm}^{-2}\,{}^{\circ}\mathrm{C}^{-1}\mathrm{yr}^{-1}$). In similar studies where Budyko-Sellers type models are applied to Earth, R is not usually given explicitly because the equilibrium solutions do not depend on R. However, in studies where the dynamics are considered, values of $R_E = 12.6$ $\mathrm{Wm}^{-2}\,{}^{\circ}\mathrm{C}^{-1}\mathrm{yr}^{-1}$ [47] or $R_E = 126$ $\mathrm{Wm}^{-2}\,{}^{\circ}\mathrm{C}^{-1}\mathrm{yr}^{-1}$ [30] are sometimes used. Note that the factor of 10 difference here is due to the assumed depth of the surface layer which was 100 m in [47] and 1000 m in [30].

On Pluto we must consider the heat capacity of frozen nitrogen. Nitrogen's heat capacity ranges from approximately 0.89 $\mathrm{Jg}^{-1}\mathrm{K}^{-1}$ to approximately 3.28 $\mathrm{Jg}^{-1}\mathrm{K}^{-1}$ around

its freezing point [20]. Since the density of nitrogen ice is approximately 1030 kg m^{-3} at Pluto temperatures of 37 K [40], the heat capacity ranges from $9.2 \cdot 10^5$ $Jm^{-3}K^{-1}$ to $3.4 \cdot 10^6$ $Jm^{-3}K^{-1}$. Assuming that the entire surface of Pluto is nitrogen that must be heated to a depth of 200 meters (a similar depth was assumed in [26]), we find that R ranges from $1.8 \cdot 10^8$ $Jm^{-2}K^{-1}$ to $6.8 \cdot 10^8$ $Jm^{-}2K^{-1}$ which is approximately 5.8 Wm^{-2} $^{\circ}C^{-1}yr^{-1}$ to 21.4 Wm^{-2} $^{\circ}C^{-1}yr^{-1}$.

The parameter ρ was used in [47] (called ϵ in that study) and [30] to understand the response of the ice line to changes in temperature. [47] takes $\rho_E = 0.01$ and [30] consider a range of small ρ_E values. They note that for large ρ correspond to near instantaneous adjustment of the ice line to changes in temperature which may be appropriate for a water planet, but are not appropriate when modeling Earth. We assume that ρ_P should also be small to avoid instantaneous adjustment of the ice line.

Using $R_E = 12.6$ and $\rho_E = 0.01$ we get $\lambda_E = 4.69 \cdot 10^{-4}$. The order of magnitude of $\rho_P QR$ is less than or equal to 1 as long at the order of magnitude of ρ_P is less than 1. A value of ρ_E close to 1 is very large (see [30]), so that is a reasonable assumption to take. Taking $B_P = 1$, we have that the order of magnitude of λ_P is less than or equal to 1. We will see that the values for B that admit stable, asymmetric ice belts can be quite large, but this may be due to our assumptions about other parameters. In section 3, we are concerned with finding equilibrium solutions of the ice line equation, so we do not need to specify a particular value of λ_P. For our analysis, we need only assume that λ_P is small which will be true as long as ρ_P is small enough.

Surface Albedos. The typical values taken in Budyko-Sellers EBMs for the albedos of Earth are $\alpha_1 = 0.32$ (ice free albedo between the ice lines) and $\alpha_2 = 0.62$ (ice albedo polward of the ice lines) [41, 47, 8]. Pluto has a striking range of albedos, in particular, normal reflectances on Pluto range from 0.08 to 1.0 [7]. Dark terrain on Pluto is characterized by the lowest albedo range in Cthulhu Regio of 0.08 to 0.2 and the slightly brighter but still relatively dark mid-latitudes with normal reflectances of 0.2 to 0.3 [7]. The bright heart shaped Tombaugh Regio has “extraordinarily high” albedo

Table 5.1: Parameter values used in the nondimensionalized Budyko-Widiasih model for Pluto.

Parameter	Name	Value for Pluto	Relation to Dimensional Constants
ζ	Cosine of obliquity	-0.4939	$\zeta = \cos\beta$
μ	Radiative forcing	0.588	$\mu = (A + BT_c)/Q$
δ	Efficiency of heat transport	0.01	$\delta = C/B$
λ	Measure of ice line response to changes in temperature	varies, small	$\lambda = \rho QR/B^2$
α_1	Albedo between the ice lines	0.6	N/A
α_2	Albedo poleward of the ice lines	0.2	N/A

values of 0.9 to 1.0 [7]. Besides these extremes, there is also terrain of intermediate albedo around 0.5 [7]. In previous modeling studies albedo values of 0.1, 0.3 and 0.6 have been used to model Pluto's albedo contrasts [15, 16]. In this study we take $\alpha_1 = 0.6$ (albedo between the ice lines) and $\alpha_2 = 0.2$ (albedo poleward of the ice lines) for Pluto although we also present our results as functions of α_1 and α_2 where possible.

5.2 Ice Line Equilibrium Solutions

In this section we assume that λ, the parameter controlling the ice line response to changes in φ, is small (i.e. significantly less than 1). Physically, this means that the ice line changes slowly relative to changes in the temperature and is well approximated by assuming φ comes to an equilibrium before the ice lines do. This assumption allows us to first find the equilibrium temperature φ^* and then determine how the location of the ice lines adjust to this change. A similar assumption is employed in [47], [30], and [2].

The restriction to small λ does not change the ice line equilibria of the system

because λ scales both equations in the ice line system, meaning that any zero of the system is unaffected by the magnitude of λ (as long as $\lambda \neq 0$). A small λ allows for a more straightforward calculation of equilibria solutions than large λ because we can first find φ^*. This is the main motivation for making this restriction below.

5.2.1 Calculation of Equilibrium Solutions

Recall from Section 4.2 that the ice line equilibria occur when $d\eta_S/d\tau = 0$ and $d\eta_N/d\tau = 0$ simultaneously. This occurs when both $\varphi^*(\eta_S) = 0$ and $\varphi^*(\eta_N) = 0$ for $\eta_S, \eta_N \in (-1, 1)$, i.e. when

$$\begin{aligned} 0 &= \varphi^*(\eta_S) \\ &= \sigma_6(\eta_S, \zeta)(1 - \alpha(\eta_S, \eta)) - \mu + \delta\left(1 - \mu - \alpha_2 + \frac{\alpha_2 - \alpha_1}{2}\int_{\eta_S}^{\eta_N} \sigma_6(y, \zeta)dy\right) \\ &= \sigma_6(\eta_S, \zeta)\left(1 - \frac{\alpha_1 + \alpha_2}{2}\right) - \mu + \delta\left(1 - \mu - \alpha_2 + \frac{\alpha_2 - \alpha_1}{2}\int_{\eta_S}^{\eta_N} \sigma_6(y, \zeta)dy\right), \end{aligned} \tag{5.4}$$

and

$$\begin{aligned} 0 &= \varphi^*(\eta_N) \\ &= -\left(\sigma_6(\eta_N, \zeta)\left(1 - \frac{\alpha_1 + \alpha_2}{2}\right) - \mu + \delta\left(1 - \mu - \alpha_2 + \frac{\alpha_2 - \alpha_1}{2}\int_{\eta_S}^{\eta_N} \sigma_6(y, \zeta)dy\right)\right). \end{aligned} \tag{5.5}$$

In previous studies [8, 36, 47, 30], equilibria of the system have been computed analytically to find the relationship between equilibrium solutions and different parameters of interest (in particular, A and Q). This was possible in part because the insolation distribution in those studies was approximated as a second degree polynomial or lower. However, there is no general formula to describe the solutions to fifth degree polynomials and higher in terms of their coefficients and, in general, polynomial equations of degree higher than four do not have algebraic solutions in terms of their coefficients. While some higher degree polynomial equations can certainly be solved in terms of their coefficients the solution is generally too complex to be used in practice.

In section 3.2, we first give numerical solutions for the parameter values given in Table 5.1 as it is not possible to find general analytic equilibrium solutions for our ice line equations. In section 3.3, we then generalize these numerical results, where possible, to indicate the range of values for which these solutions persist.

5.2.2 Equilibria and Phase Portraits

The vector fields depicted in Figure 5.1 describe the flows of the northern and southern ice edges on Pluto as governed by

$$\begin{aligned} \dot{\eta}_S &= \lambda(F(\eta_S, \eta_N) - G(\eta_S)) \\ \dot{\eta}_N &= -\lambda(F(\eta_S, \eta_N) - G(\eta_N)) \end{aligned} . \tag{5.6}$$

The part of the vector field below the line $\eta_S = \eta_N$ represents flows where $\eta_S > \eta_N$ (i.e. the southern ice line is northward the northern ice line) which is non-physical and has, thus, been omitted. The red dots designate equilibrium solutions of Equation (5.6). It is important to note that equilibria on the line $\eta_S = -\eta_N$ indicate an ice block that is symmetric across the equator and any equilibria not on this line are asymmetric.

In Figure 5.1, flows which reach the upper left corner at $(-1, 1)$ correspond to both ice lines at the poles, which indicates a completely glaciated planet. Flows that reach the line $\eta_S = \eta_N$ indicate that the ice lines have come together, i.e. an ice free state. In previous studies, the symmetry condition forced solutions to come together at the equator [2, 47]; however, in this study the ice lines can come together anywhere in the interval $[-1, 1]$.

For Pluto, the stable equilibria are located at

$$e_1 = (-0.578, 0.578), \quad e_2 = (-0.562, -0.094), \quad \text{and} \quad e_3 = (0.094, 0.562). \tag{5.7}$$

Notice that e_2 and e_3 are both stable, asymmetric equilibria of the system (5.6). Converting these values back to latitude (degrees) gives $\tilde{e}_1 = (-35.31, 35.31)$, $\tilde{e}_2 =$

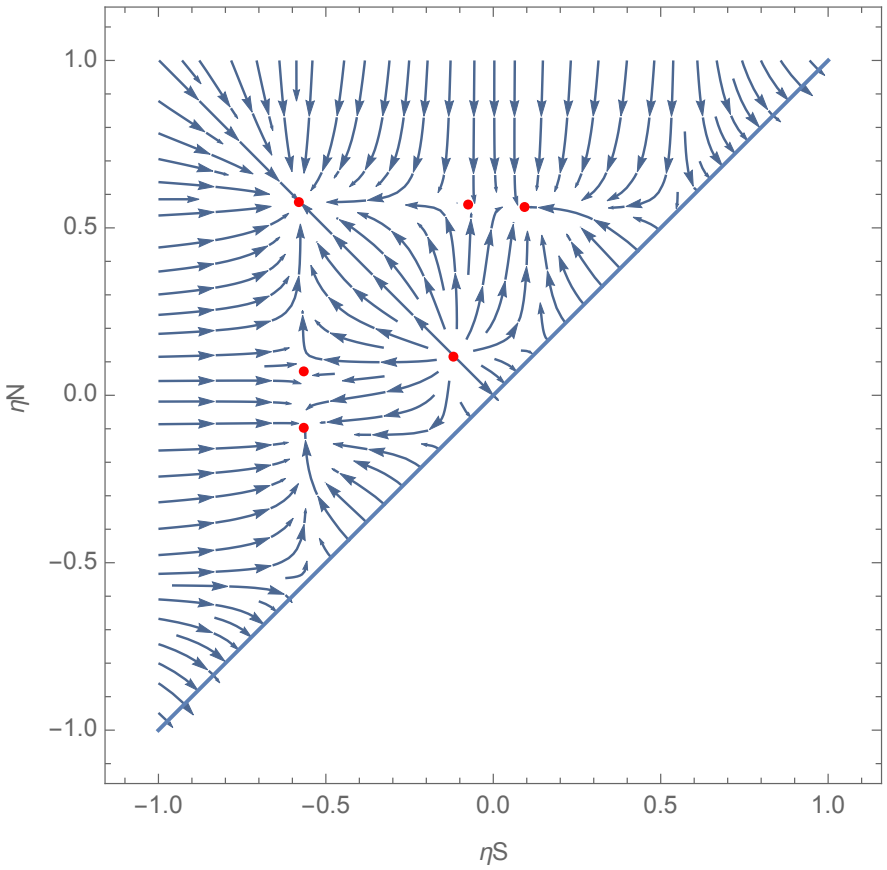

Figure 5.1: Ice line vector fields. The horizontal axis is the southern ice line (η_S) and the vertical axis is the northern ice line (η_N). Parameter values are indicated in Table 5.1 for Pluto. Red dots indicated equilibria of the ice line equations (5.6). The line $\eta_S = \eta_N$ depicts where the ice lines come together. Solutions with $\eta_S > \eta_N$ are not physical. Vector field for the movement of the ice lines for an ice belt on Pluto. There are three stable equilibria at approximately (-0.578, 0.578), (-0.562, -0.094), and (0.094, 0.562) as well as two saddle equilibria, and one unstable equilibrium. See text for a detailed discussion.

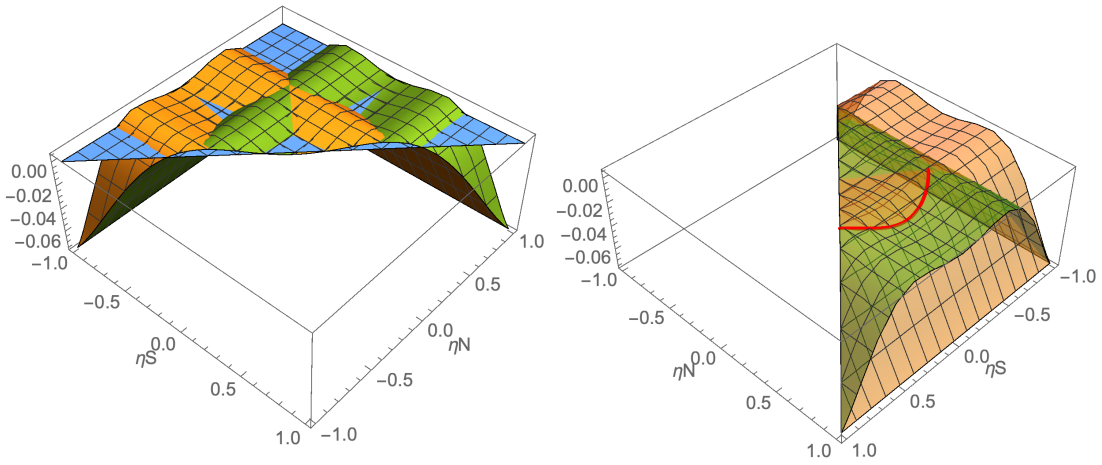

Figure 5.2: **Left:** The surfaces $P(\eta_S, \eta_N)$ (green), $S(\eta_S)$ (orange), and $S(\eta_N)$ (blue) for the parameter values from Table 5.1. Points where all three surfaces intersect are equilibria of the ice line system (5.6). **Right:** The red curve indicates where $S(\eta_N)$ intersects $S(\eta_S)$. This curve is independent of α_1, α_2, μ, and δ, and, as such, an asymmetric equilibria exists if and only if it is on this curve. Note that the perspective for this plot is shifted from the left hand plot to better so that the intersection curve is featured. Labels for the vertical axes are omitted because P and S are nondimensional.

$(-34.2, -5.4)$, and $\tilde{e}_3 = (5.4, 34.2)$. The equilibrium e_3 places the northern ice line at 34.2 °N and the southern ice line at 5.4 °N. This places a stable asymmetric ice belt within the latitudinal range of the observed *Sputnik Planitia* [23, 15, 49].

However, the parameters μ and δ control the location of the equilibria in Figure 5.1 (detailed in the next subsection) and, in particular, the saddle equilibrium located at $e_4 = (-0.072, 0.566)$ (approximately 4.1 °S and 34.5 °N). Changing μ and δ moves this saddle equilibrium left or right and, for certain values, an ice belt in the latitudinal ranges of *Sputnik Planitia* could be in the basin of attraction for the symmetric equilibrium e_1 or the asymmetric equilibrium e_3.

5.2.3 Nondimensional Parameter Ranges Yielding Stable, Asymmetric Ice Belts

In the computations below, we hold the albedo parameters, α_1 and α_2, constant and determine the maximum and minimum values of δ and μ for which there are stable, asymmetric equilibria of system (5.6) for Pluto. We define the functions

$$P(a,b) = \frac{\delta(\alpha_2 - \alpha_1)}{2} \int_a^b \sigma_6(\tilde{y}, \zeta) d\tilde{y}, \text{ and} \tag{5.8}$$

$$S(c) = -\left(\sigma_6(c,\zeta)\left(1 - \frac{\alpha_1 + \alpha_2}{2}\right) - \mu + \delta(1 - \mu - \alpha_2)\right) \tag{5.9}$$

so that the ice line equilibrium equations (5.4) and (5.5) can be written

$$\begin{aligned} 0 &= P(\eta_S, \eta_N) - S(\eta_S), \text{ and} \\ 0 &= -P(\eta_S, \eta_N) + S(\eta_N). \end{aligned} \tag{5.10}$$

The functions P and S do not have easily described physical interpretations, however they are helpful in visualizing the location of equilibria. Crucially, the ice line equilibria occur where the surfaces $P(\eta_S, \eta_N)$, $S(\eta_S)$, and $S(\eta_N)$ have a common intersection which is illustrated in the left hand image of Figure 5.2.

The parameters μ and δ cause the surfaces to shift or scale. The parameter μ does not affect the surface $P(\eta_S, \eta_N)$ and serves only to shift the surfaces $S(\eta_S)$ and $S(\eta_N)$ up or down the z-axis. Increasing μ moves $S(\eta_S)$ and $S(\eta_N)$ up the z-axis and decreasing μ moves them down. The parameter δ scales $P(\eta_S, \eta_N)$. When $\delta = 0$, $P(\eta_S, \eta_N) = 0$ and the surface corresponds to the (η_S, η_N) plane. For small δ, $P(\eta_S, \eta_N)$ can be well approximated by a plane (we notice that it appears almost flat in Figure 5.2); however we do not make that approximation below. The surface P is generally increasing in the positive η_S and η_N directions, although for $\delta \gg 1$, this increase may not be monotonic. For the surfaces $S(\eta_S)$ and $S(\eta_N)$, δ acts as a vertical shift; increasing δ shifts the surfaces down.

The intersection of the surfaces $S(\eta_S)$ and $S(\eta_N)$ depends only on ζ (and not on μ, δ, α_1 or α_2). We see this by setting $S(\eta_S) = S(\eta_N)$. Simplifying this equation yields $\sigma_6(\eta_S, \zeta) = \sigma_6(\eta_N, \zeta)$, so $S(\eta_S)$ and $S(\eta_N)$ intersect exactly where $\sigma_6(\eta_S, \zeta)$ and $\sigma_6(\eta_N, \zeta)$ are equal. We can compute this intersection explicitly as a function of ζ in a computer algebra software (we use *Mathematica*) and the portion of this intersection above the lines $\eta_S = -\eta_N$ and $\eta_S = \eta_N$ is plotted in red in the right hand image of Figure 5.2. The surface P has been removed from the right hand image of Figure 5.2 to highlight the intersection curve. This curve can be parameterized by η_S to remove the η_N dependency. This parameterization is given by

$$\eta_N = \iota(\eta_S) = \sqrt{0.969268 - 0.5\eta_S^2 - \sqrt{0.412268 + 0.969268\eta_S^2 - 0.75\eta_S^4}}. \tag{5.11}$$

Notice that there is an identical curve of intersection reflected across the line $\eta_S = -\eta_N$. Since the surfaces P and S are symmetric about this line, we omit discussion of this lower portion of the intersection curve and simply reflect any equilibria we find through the line $\eta_S = \eta_N$.

Ice line equilibria correspond to intersections of the parametric curves $(\eta_S, \iota(\eta_S), S(\eta_S))$ (the red curve denoting the intersection of the surfaces $S(\eta_S)$ and $S(\eta_N)$) and

$$(\eta_S, \iota(\eta_S), P(\eta_S, \iota(\eta_S))) \tag{5.12}$$

(the red curve projected onto the surface $P(\eta_S, \eta_N)$). Four cases of these parametric curves for different parameter values are illustrated in the left hand side of Figure 5.3. In the left hand figures, the solid, red curve is $(\eta_S, \iota(\eta_S), S(\eta_S))$ and the dotted, blue curve is $(\eta_S, \iota(\eta_S), P(\eta_S, \iota(\eta_S)))$. The surfaces have been removed from these figures so that to better display the intersections of the curves. In the middle column of Figure 5.3, we plot the same curves with the η_N dimension flattened. We remove this dimension for ease of computations.

Finally, the right hand column of Figure 5.3 displays the corresponding vector fields for the ice line equations in system (5.6). The first row corresponds to the parameter values in Table 5.1, the second to δ replaced with δ_{max}, the third to μ replaced with μ_{min}, and the fourth to μ replaced with μ_{max}. In the second row, the asymmetric stable equilibria have collided with the saddle equilibria closest to the line $\eta_S = \eta_N$ and coalesced into saddle equilibria. In the third row, the asymmetric stable equilibria have collided with newly generated saddle equilibria closest to the line $\eta_S = -\eta_N$ and coalesced into saddle equilibria. In the fourth row, the asymmetric stable equilibria have collided with the saddle equilibria closest to the line $\eta_S = \eta_N$ and coalesced into degenerate equilibria (the asymmetric equilibria will disappear for $\mu > \mu_{max}$, stable or otherwise).

The maximum and minimum values of the parameters for which there are asymmetric stable solutions can be visualized as different tangencies of the parametric curves $(\eta_S, \iota(\eta_S), S(\eta_S))$ and $(\eta_S, \iota(\eta_S), P(\eta_S, \iota(\eta_S)))$ (see Figure 5.3). It can be shown that the parametric curves are tangent if and only if the functions $P(\eta_S, \iota(\eta_S))$ and $S(\eta_S)$ are tangent. It is easier to determine when $P(\eta_S, \iota(\eta_S))$ and $S(\eta_S)$ are tangent for different values of δ and μ and we do so below. The argument relies on the fact that there are stable, asymmetric equilibria if and only if the curves intersect twice for η_S between the local maxima of $S(\eta_S)$, i.e. $\eta_S \in [-0.393, 0.393]$.

To find the maximum value of δ for which there are stable, asymmetric equilibria, we note that the largest effect of changing δ is to scale $P(\eta_S, \eta_N)$. This scaling causes the difference between the endpoints, given by $P(0.393, \iota(0.393)) - P(-0.393, \iota(-0.393))$, to increase. If P becomes too steep it will only intersect S at one point, meaning the stable asymmetric equilibria are not present. The smallest value of δ for which there is only one intersection occurs when $P(\eta_S, \iota(\eta_S))$ is tangent to the inflection point of $S(\eta_S)$ in the positive half line (see Figure 5.3(b)). The inflection points of S depend only on the parameter ζ. For $\zeta = \cos(\pi 119.6/180) \approx -0.4939$, the point is located at

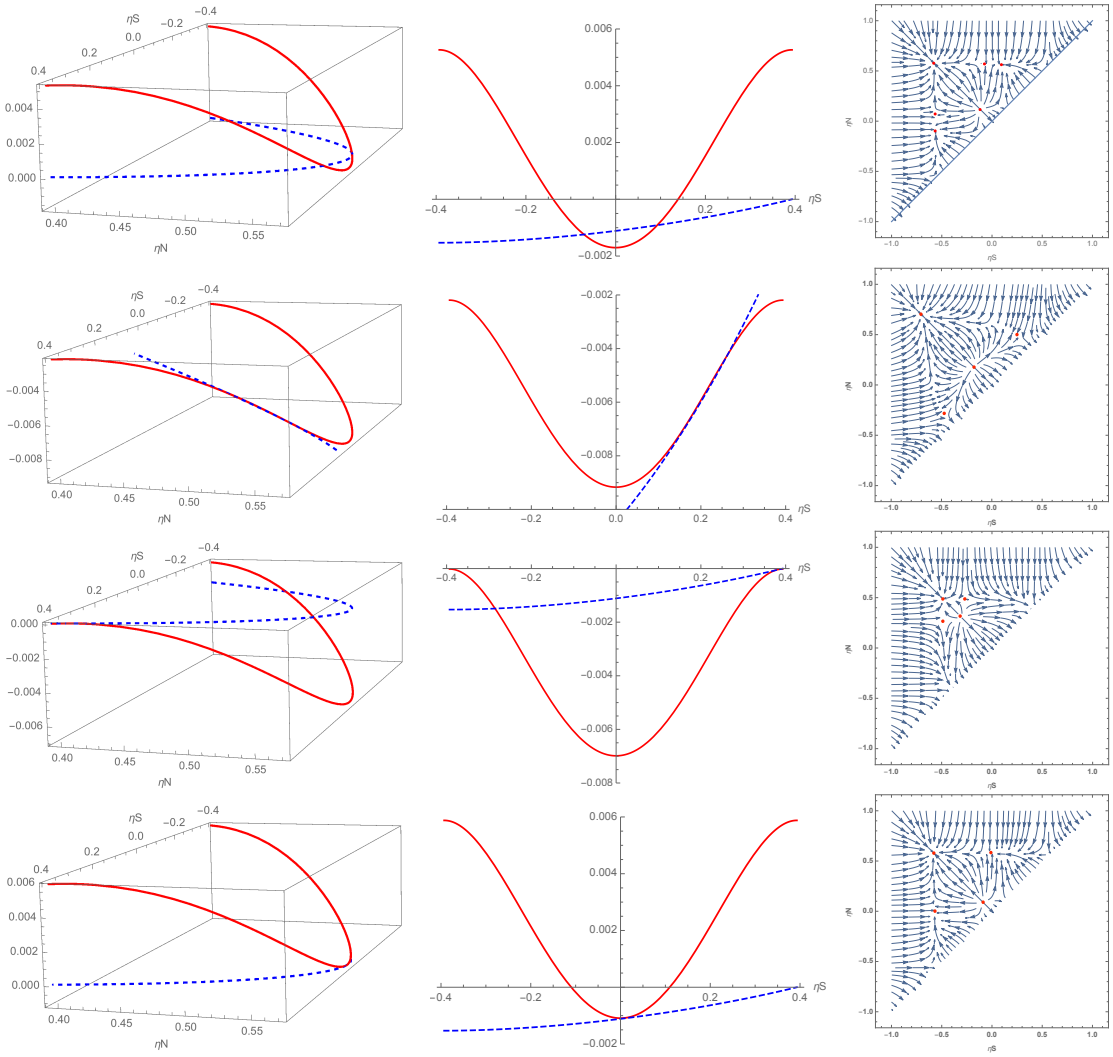

Figure 5.3: **Left column:** Intersections of the parametric curves $(\eta_S, \iota(\eta_S), S(\eta_S))$ (solid, red) and $(\eta_S, \iota(\eta_S), P(\eta_S, \iota(\eta_S)))$ (dashed, blue). The vertical scales are exaggerated for clarity. **Middle column:** Intersections of the parametric curves $(\eta_S, S(\eta_S))$ (solid, red) and $(\eta_S, P(\eta_S, \iota(\eta_S)))$ (dashed, blue). The vertical scales are exaggerated for clarity. **Right column:** Ice line vector fields. Red dots indicate equilibria of the ice line equations (5.6). **First row:** Parameter values given in Table 5.1; **Second row:** Parameter values given in Table 5.1 except $\delta = \delta_{max}$; **Third row:** Parameter values given in Table 5.1 where instead $\mu = \mu_{min}$; and **Fourth row:** Parameter values given in Table 5.1 where instead $\mu = \mu_{max}$. The axis labels for the vertical axes in the left and middle columns are omitted because the parametric curves are nondimensional.

$\eta_S = \eta_S^* \approx 0.219866$. The slopes of $P(\eta_S, \iota(\eta_S))$ and $S(\eta_S)$ at $\eta_S = \eta_S^*$ are equal when

$$\begin{aligned} 0 &= \frac{d}{d\eta_S}(P(\eta_S, \iota(\eta_S)) - S(\eta_S))\Big|_{\eta_S=\eta_S^*} \\ &= 0.726458(\alpha_1 - \alpha_2)\delta - 0.0456133(1 - 0.5(\alpha_1 + \alpha_2)). \end{aligned}$$

This tells us that if

$$\delta \geq \delta_{max} := \frac{0.0456133(1 - 0.5(\alpha_1 + \alpha_2))}{0.726458(\alpha_1 - \alpha_2)} = 0.0627886\frac{1 - 0.5(\alpha_1 + \alpha_2)}{\alpha_1 - \alpha_2},$$

there cannot be stable, asymmetric ice line equilibria. For our values of albedo this value is $\delta_{max} \approx 0.0941829$. Notice that if the albedos are close in value, then δ_{max} can be quite large. In fact, as α_2 approaches α_1, the maximum value for δ for which there can be stable, asymmetric ice line equilibria goes to infinity.

For $0 \leq \delta < \delta_{max}$, there is a minimum μ so that there is an asymmetric stable ice belt and a maximum μ. The minimum μ occurs when $P(\eta_S, \iota(\eta_S))$ is tangent to $S(\eta_S)$ between its inflection point and maximum in the positive half of the real line, i.e. $\eta_S \in [\eta_S^*, 0.393]$. The maximum μ occurs when $P(\eta_S, \iota(\eta_S))$ is tangent to $S(\eta_S)$ between zero and the inflection point of $S(\eta_S)$, i.e. $\eta_S \in [0, \eta_S^*]$. These scenarios are depicted in the bottom two rows of Figure 5.3.

It is not possible to solve for μ_{min} or μ_{max} in terms of α_1, α_2, and δ because the difference of the derivatives of P and S is not in the form of a solvable sixth degree polynomial. Instead we compute the numerical solutions for μ_{min} and μ_{max} with the values for α_1, α_2, and δ as given in Table 5.1. We then vary δ between 0 and δ_{max} and recompute μ_{min} and μ_{max}. These results are given in Figure 5.4.

To find μ_{min} we first solve

$$0 = \frac{d}{d\eta_S}(P(\eta_S, \iota(\eta_S)) - S(\eta_S)) \tag{5.13}$$

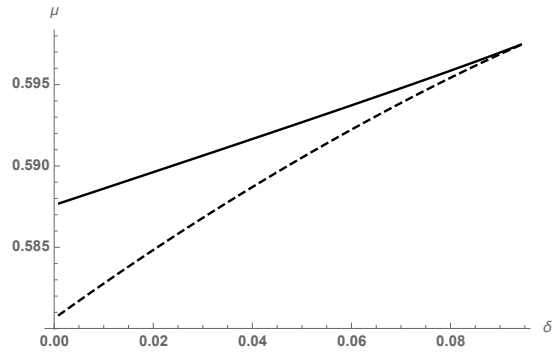

Figure 5.4: The minimum (dashed) and maximum (solid) values of μ that result in stable, asymmetric ice belts for different values of δ (holding $\alpha_1 = 0.6$, $\alpha_2 = 0.2$, and $\zeta = -0.4939$). The curves meet at $\delta = \delta_{max}$ where they are approximately equal to 0.5975. Any $(\delta - \mu)$-pair between these lines admits stable, asymmetric ice belts.

numerically on the interval $[\eta_S^*, 0.393]$. (Notice that the derivaitve of S does not depend on μ.) This generates a unique $\eta_S = \hat{\eta}_S$ for which the derivatives are equal on this interval. We then plug $\eta_S = \hat{\eta}_S$ into Equation (5.10) to get

$$0 = P(\hat{\eta}_S, \iota(\hat{\eta}_S), \mu) - S(\hat{\eta}_S), \mu).$$

Solving for the μ which satisfies this equation yields μ_{min}.

To find μ_{max}, we solve equation (5.13) on the interval $[0, \eta_S^*]$. This process again admits a unique $\eta_S = \check{\eta}_S$ for which the derivatives are equal on the interval. The μ which satisfies

$$0 = P(\check{\eta}_S, \iota(\check{\eta}_S), \mu) - S(\check{\eta}_S), \mu)$$

is μ_{max}. For the parameter values in Table 5.1, the minimum and maximum μ which admit stable, asymmetric equilibria are $\mu_{min} \approx 0.58277$ and $\mu_{max} \approx 0.588608$. Holding α_1 and α_2 constant but increasing δ causes both μ_{min} and μ_{max} to increase until they meet at the value of approximately 0.5975.

5.2.4 Dimensional Parameter Ranges Yielding Stable, Asymmetric Ice Belts

In order to place these results within a more physical framework, we convert the nondimensional parameters back to the physical parameters of A, B, and C. Using the equations for δ and μ from section 2.3, we get

$$A = Q\mu - (CT_c)/\delta \quad \text{and} \quad B = C/\delta \tag{5.14}$$

as long as $\delta \neq 0$. As discussed in section 2.4, we let $C = .01$ Wm^{-2} $^{\circ}C^{-1}$ due to Pluto's lack of substantial atmosphere or oceans to circulate heat. Given that $\delta \in [0.001, \delta_{max}]$ and $\mu \in [\mu_{min}, \mu_{max}]$ (i.e. that the ordered pair (δ, μ) is in the triangular region depicted in Figure 5.4) we see that A ranges from approximately 25.41 Wm^{-2} to 2381.63 Wm^{-2} and B ranges from approximately 0.106 Wm^{-2} $^{\circ}$C^{-1} to 10 Wm^{-2} $^{\circ}$C^{-1}. For $\delta \in (0, 0.001]$, the values of A and B increase rapidly to infinity.

5.3 Discussion

In this chapter, we study a Budyko-Sellers type energy balance model with two dynamic ice lines. We nondimensionalize the model and present the case of an ice belt on Pluto. We present a framework that can be used to study the possibility of asymmetric ice configurations on other rocky planets and moons in the solar system and beyond. The model provides a highly idealized framework for considering the phenonmena of ice-albedo feedback and the results should be interpreted broadly to tell us about the predominant or possible mechanisms affecting the location of ices on a planet.

The main result of this analysis shows that it is possible to have a stable ice belt which is not symmetric across the equator in a Budyko-Sellers type energy balance model with two dynamic ice lines. In particular, these stable, asymmetric equilibria are present even in the absence of external, asymmetric forcings. This is the first study

showing stable, asymmetric ice line equilibria; however, we hypothesize that there are other obliquities where asymmetric equilibria of the ice line equations exist and we encourage further study to determine the limits of parameter values which admit stable asymmetric equilibria.

For certain choices of parameter values, the stable, asymmetric ice belt falls within the observed ranges of *Sputnik Planitia*, see Figure 5.5. Observations show that there are high albedo regions which fall south of Pluto's equator; however it is not possible in our model to have a stable ice belt which falls over the equator unless it is symmetric about the equator. If the parameter values of μ and δ used in this study were accurate for Pluto, that would indicate that the ice belt given by largest possible latitude range of *Sputnik Planitia* (indicated by the red diamond in Figure 5.5) is in the basin of attraction for the large symmetric ice belt and that both the northern and southern edges of the region should be retreating southward. The basins of attraction for the symmetric and asymmetric ice belts are highly dependent on the values of μ and δ. Furthermore, whether or not our model *Sputnik Planitia* is growing into a large region which is symmetric across the equator or shrinking to an asymmetric region north of the equator is highly dependent on the norther or southern boundaries that are chosen.

The ice line vector field for Pluto (Figure 5.1, right hand side) demonstrates that for some initial conditions, an ice belt that is nearly symmetric across the equator will flow to an asymmetric configuration rather than a symmetric one. On the other hand, very thin ice belts near the equator can either shrink to nothing or grow to an asymmetric ice belt, but it is not possible for them to grow into ice belts which are symmetric across the equator, even if they are initially symmetric. This sensitive dependence on initial conditions for small ice belts near the equator is a potential indication that there may be large spatial heterogeneity at the equator, as has been observed on Pluto [**?**]. Because our model does not have longitudinal dependence, we cannot confirm this hypothesis. One could imagine extending a Budyko-Sellers type model to account for longitudinal variations; however the authors are unaware of such studies.

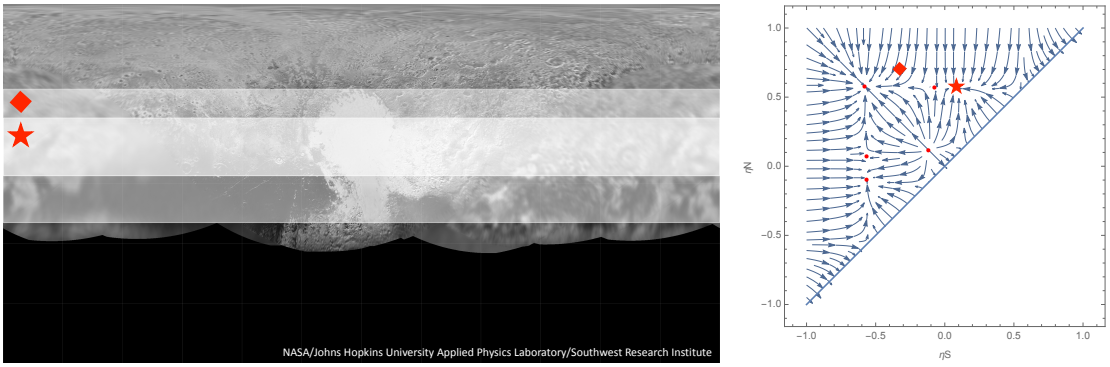

Figure 5.5: New Horizons surface map of Pluto with model location of ice belts overlaid on top. The ice belt identified with the red star is where the asymmetric stable ice belt is located in the model. The ice belt identified with the red diamond gives the northernmost and southernmost latitudes with high albedo (by eye). Note that the surface map has a faint $30^\circ \times 30^\circ$ grid overlaid on it as well. Both belts are additionally indicated in the vector field on the right. Surface map image source: NASA/Johns Hopkins University Applied Physics Laboratory/Southwest Research Institute

Calculation of the stable, asymmetric equilibria as they depend on the parameters in the model show that the stable, asymmetric ice line equilibria are present for a wide range of parameter values.

Although the values taken for the OLR parameters in the model are very uncertain, our analysis shows that the stable, asymmetric equilibria are present for a wide range of values for these parameters. This suggests that if we did know the actual values for A and B for Pluto, there is a high likelihood that they would generate a system with stable, asymmetric ice belts.

Furthermore, we note that regardless of the albedo contrast, δ_{max} is always greater than 0. This implies that it is always possible to find stable, asymmetric equilibria of the ice line equations when $\zeta = -0.4939$. We note that if the albedo contrast is very small, then stable, asymmetric equilibria can exist when heat transport is large relative to outgoing radiation (δ). Conversely, for the largest possible albedo contrast ($\alpha_1 = 1$ and $\alpha_2 = 0$), $\delta_{max} \approx 0.031$, so only planets with relatively weak heat transport can

support stable, asymmetric ice belts. This indicates that asymmetric ice formations are expected on high obliquity planets with heat transport that is weak relative to the outgoing radiation.

The apparent generality of the stable, asymmetric equilibria within the model seem to indicate that the primary mechanistic explanation for their existence is due to the effects of the insolation distribution and latitudinal heat transport. Further investigations into other forms of heat transport and its effects on location, type, and number of equilibria will help characterize the role of insolation on asymmetric ice belts.

[15] argue that insolation is not the driving factor of Pluto's equatorial albedo variance, but instead the fact that the equatorial regions are always in the diurnal zone and never experience Arctic day or night. They find that the constant diurnal insolation causes the equatorial regions to be a "preservation zone," i.e. whatever albedo is seeded there is preserved. [23] and [16] argue that the albedo contrasts in the equatorial regions on Pluto are due to a runaway albedo effect, again identifying the diurnal insolation as the driving mechanism. We find that the annual average insolation is enough to explain a stable ice belt within the latitude range of *Sputnik Planitia*. However, uncertainty in the parameters mean that it is not currently possible to determine from the model if an idealized *Sputnik Planitia* ice belt would be growing to a symmetric belt or shrinking to a smaller asymmetric belt. Furthermore, the simplicity of our latitude-dependent model does not admit the possibility of insolation variation along a latitude belt, meaning we cannot confirm nor refute these earlier studies.

However, because relatively little is known about heat transport and atmospheric effects on Pluto's surface temperature, it is not clear if the choice of parameters is appropriate for Pluto, and more work should be conducted to better understand the phenomena present in the model for Pluto and for other planetary scenarios.

Chapter 6

Discussion

In this work we have highlighted some generalizations for components of the incoming radiation term in an energy balance model of Earth. These generalizations admit the possibility of applying the model to planets other than Earth as well as studying Earth in greater detail.

The first part of this work focuses on incoming solar radiation and the dependence of the distribution to the planet's rotation rate and obliquity. Further work that investigates the convergence to rapid rotation for nonzero obliquities or eccentricities would be an important next step.

In the second part of this work we focus on planetary albedo on Earth and Pluto. In particular, we remove a long-standing symmetry constraint which forced the albedo to be symmetric across the equator. For the model of Pluto, the removal of this constraint allows us to find asymmetric configurations of the albedo which are stable.

References

[1] D. Abbot, A. Voigt, and D.Koll. "The Jormungand global climate state and implications for Neoproterozoic glaciations." *Journal of Geophysical Research: Atmospheres* 116.D18 (2011).

[2] A. Barry, E. Widiasih, and R. McGehee. "Nonsmooth frameworks for an extended Budyko model." :*Discrete and Continuous Dynamical Systems-Series B* 22.6 (2017): pp. 2447–2463

[3] H. Bateman. *Higher Transcendental Functions [Volume II].* A. Erdélyi, editor. McGraw–Hill (1953).

[4] T. Bertrand and F. Forget. "3D modeling of organic haze in Pluto's atmosphere." *Icarus.* 287 (2017): pp. 72–86. doi:10.1016/j.icarus.2017.01.016.

[5] R. Binzel, et al. "Climate Zones on Pluto and Charon." *Icarus.* 287 (2017): pp 30–36. doi: 10.1016/j.icarus.2016.07.023.

[6] M. Budyko. "The effect of solar radiation variations on the climate of the Earth," *Tellus*, 21.5 (1969): pp. 611–619. doi: 10.1111/j.2153-3490.1969.tb00466.x.

[7] B. Buratti, et al. "Global albedos of Pluto and Charon from LORRI *New Horizons* observations." *Icarus.* 287 (2017): pp 207–217.

[8] J. Checlair, K. Menou, and D. Abbot. "No snowball on habitable tidally locked planets." *The Astrophysical Journal* 845. 2 (2017): pp. 132.

[9] P. Chylek and J. Coakely. "Analytical analysis of a Budyko-type climate model. *Journal of the Atmospheric Sciences* 32 (1975): pp. 675–679.

[10] A. Dobrovolskis and A. Harris. "The obliquity of Pluto." *Icarus* 55.2 (1983): pp. 231–235.

[11] A. Dobrovolskis. "Spin states and climates of eccentric exoplanets." *Icarus* 192 (2007): pp. 1–23.

[12] A. Dobrovolskis. "Insolation patterns on synchronous exoplanets with obliquity." *Icarus* 204.1 (2009): pp. 1–10.

[13] A. Dobrovolskis. "Insolation on exoplanets with eccentricity and obliquity." *Icarus* 226.1 (2013): pp. 760–776.

[14] A. Dobrovolskis. "Insolation patterns on eccentric exoplanets." *Icarus* 250 (2015): pp. 395–399.

[15] A. Earle, et al. "Long-term surface temperature modeling of Pluto." *Icarus.* 287 (2017): pp 37–46.

[16] A. Earle, et al. "Albedo matters: Understanding runaway albedo variations on Pluto." *Icarus.* 303 (2018): pp 1–9.

[17] A. R. Edmonds. *Angular momentum in quantum mechanics.*Princeton University Press, (1974)

[18] F. Forget, T. Bertrand, M. Vangvichith, J. Leconts, E. Millour, and E. Lellouch. "A post-new horizons global climate model of Pluto including the N_2, CH_4 and CO cycles," *Icarus.* 287 (2017): pp. 54–71. doi:10.1016/j.icarus.2016.11.038.

[19] N. Fray and B. Schmitt. "Sublimation of ices of astrophysical interest: a bibliographic review." *Planet. Space Sci.* 57 (2009): pp.2053–2080.

[20] W. Giauque and J. Clayton. "The heat capacity and entropy of nitrogen. Heat of vaporization. Vapor pressures of solid and liquid. The Reaction 1/2 N_2+1/2 O_2 =NO from spectroscopic data." *J. Am. Chem. Soc.* 55.12 (1933): pp. 4875–4889. doi: 10.1021/ja01339a024.

[21] C. Glein and J. Waite. "Primordial N2 provides a cosmochemical explanation for the existence of Sputnik Planitia, Pluto." *Icarus.* 313 (2018): pp. 79–92. doi: 10.1016/j.icarus.2018.05.007

[22] C. Graves, W. Lee, and G. North "New Parameterizations and Sensitivities for Simple Climate Models." *Journal of Geophysical Research* 98. D3 (1993): pp 5025–5036. doi: 10.1029/92JD02666

[23] D. Hamilton, et al. "The rapid formation of Sputnik Planitia early in Pluto's history," *Nature*, 540 (2016): pp. 97–99.

[24] D. Hinson, et al. "Radio occultation measurements of Pluto's neutral atmosphere with New Horizons." *Icarus.* 209 (2017): pp. 96–111. doi: 10.1016/j.icarus.2017.02.031

[25] H. Kaper and H. Engler. *Mathematics and Climate.* Philadelphia, PA: SIAM Press, (2013).

[26] J. Keane, I. Matsuyama, S. Kamata, and J. Steckloff. "Reorientation and faulting of Pluto due to volatile loading within Sputnik Planitia." *Nature.* 540 (2016): doi:10.1038/nature20120

[27] J. LaSalle. "Some extensions of Liapunov's second method." *IRE Transactions on circuit theory* 7.4 (1960): 520-527.

[28] J. Laskar, et al. "Long term evolution and chaotic diffusion of the insolation quantities of mars." *Icarus* 170 (2004): 343–364.

[29] R. McGehee and C. Lehman. “A paleoclimate model of ice-albedo feedback forced by variations in Earth’s orbit.” *SIAM Journal on Applied Dynamical Systems* 11.2 (2012): 684-707.

[30] R. McGehee, E. Widiasih. “A quadratic approximation to Budyko’s ice-albedo feedback model with ice line dynamics.” *SIAM Journal on Applied Dynamical Systems* 13.1 (2014): 518-536.

[31] A. Nadeau and R. McGehee. “A simple formula for a planets mean annual insolation by latitude.” *Icarus* 291 (2017): 46-50.

[32] G. North. “Theory of Energy-Balance Climate Models.” *Journal of the Atmospheric Sciences* 32.11 (1975): 2033–2043.

[33] G. North. “Analytical solution to a simple climate model with diffusive heat transport.” *Journal of the Atmospheric Sciences* 32 (1975): 1301–1307.

[34] G. Ojakangas and D. Stevenson. “Thermal State of an Ice Shell onEuropa.” *Icarus* 81 (1989): 220–241.

[35] S. Protopapa et al. “Pluto’s global surface composition thought pixel-by-pixel Hapke modeling of New Horizons Ralph/LEISA data.” *Icarus.* 287 (2017): pp 218–228.

[36] B. Rose, T. Cronin, and C. Bitz. “Ice Caps and Ice Belts: The Effects of Obliquity on Ice–Albedo Feedback.” *The Astrophysical Journal* 846.1 (2017): pp. 28–45.

[37] H. Rother, et al. ”The early rise and late demise of New Zealands last glacial maximum.” Proceedings of the National Academy of Sciences 111.32 (2014): pp. 11630-11635.

[38] W. Sellers. “A global climatic model based on the energy balance of the earth-atmosphere system.” *Journal of Applied Meteorology* 8.3 (1969): pp. 392–400.

[39] S. Stern, et al. "The pluto system: initial results from its exploration by new horizons. *Science.* 350 (2015): aad1815.

[40] A. Trowbridge, et al. "Vigorous convection as the explanation for Pluto's polygonal terrain." *Nature* 534.7605 (2016): pp. 79.

[41] K. K. Tung. '*Mathematical Modeling.* Princeton, NJ: Princeton University Press, (2007).

[42] O. Umurhan, et al. "Modeling glacial flow on and onto Pluto's Sputnik Planitia" *Icarus.* 287 (2017): pp 301–319.

[43] J. Walsh and C. Rackauckas. "On the Budyko-Sellers energy balance climate model with ice line coupling." *Disc. Cont. Dyn. Syst. B* 20.7 (2015).

[44] H. Wang. "A new and sharper bound for Legendre expansion of differentiable functions." *Applied Mathematics Letters* 85 (2018). pp. 95–102. doi: 10.1016/j.aml.2018.05.022

[45] W. Ward. "Climatic variations on Mars: 1. Astronomical theory of insolation." *Journal of Geophysical Research* 79.24 (1974): 3375-3386.

[46] E. Whittaker and G. Watson. *A course of modern analysis.* Cambridge University Press. (1990).

[47] E. Widiasih. "Dynamics of the Budyko energy balance model." *SIAM Journal on Applied Dynamical Systems* 12.4 (2013): 2068-2092.

[48] E. Widiasih, M. Stuecker, and S. Baek "The Mid Pleistocene Transition from a Budyko-Sellers Type Energy Balance Model," arXiv: 1806.03900.

[49] O. White, et al. "Geological mapping of Sputnik Planitia on Pluto." *Icarus.* 287 (2017): pp 261–286.

[50] L. Young, et al. “Structure and composition of Pluto’s atmosphere from the New Horizons solar ultraviolet occultation.” *Icarus.* 300 (2018): pp. 174–199. doi: 10.1016/j.icarus.2017.09.006